

SYNTHESIS AND CHARACTERIZATION OF MICROPOROUS  
TITANO/VANADOSILICATE ZEOTYPE FILMS FOR HUMIDITY SENSING  
APPLICATIONS

A THESIS SUBMITTED TO  
THE GRADUATE SCHOOL OF NATURAL AND APPLIED SCIENCES  
OF  
MIDDLE EAST TECHNICAL UNIVERSITY

BY

RAMONA DAVOUDNEZHAD

IN PARTIAL FULFILLMENT OF THE REQUIREMENTS  
FOR  
THE DEGREE OF DOCTOR OF PHILOSOPHY  
IN  
MICRO AND NANOTECHNOLOGY

DECEMBER 2022



Approval of the thesis:

**SYNTHESIS AND CHARACTERIZATION OF MICROPOROUS  
TITANO/VANADOSILICATE ZEOTYPE FILMS FOR HUMIDITY  
SENSING APPLICATIONS**

submitted by **RAMONA DAVOUDNEZHAD** in partial fulfillment of the requirements for the degree of **Doctor of Philosophy in Micro and Nanotechnology, Middle East Technical University** by,

Prof. Dr. Halil Kalıpçılar  
Dean, Graduate School of **Natural and Applied Sciences**

Prof. Dr. Deniz Üner  
Head of the Department, **Micro and Nanotechnology**

Prof. Dr. Burcu Akata Kurç  
Supervisor, **Micro and Nanotechnology, METU**

Prof. Dr. Necati Özkan  
Co-Supervisor, **Polymer Science and Technology, METU**

**Examining Committee Members:**

Prof. Dr. Caner Durucan  
Metallurgical and Materials Eng, METU

Prof. Dr. Burcu Akata Kurç  
Micro and Nanotechnology, METU

Assoc. Prof. Selis Önel Kayran  
Chemical Engineering, Hacettepe Uni.

Prof. Dr. Emren Nalbant  
Chemistry, METU

Prof. Dr. Murat Kaya  
Chemical Engineering, Atılım Uni.

Date: 22.12.2022

**I hereby declare that all information in this document has been obtained and presented in accordance with academic rules and ethical conduct. I also declare that, as required by these rules and conduct, I have fully cited and referenced all material and results that are not original to this work.**

Name Last name: Ramona Davoudnezhad

Signature :

## **ABSTRACT**

### **SYNTHESIS AND CHARACTERIZATION OF MICROPOROUS TITANO/VANADOSILICATE ZEOTYPE FILMS FOR HUMIDITY SENSING APPLICATIONS**

Davoudnezhad, Ramona  
Doctor of Philosophy, Micro and Nanotechnology  
Supervisor: Prof. Dr. Burcu Akata Kurç  
Co-Supervisor: Prof. Dr. Necati Özkan

December 2022, 120 pages

The growing demand for environmental control for various chemical molecules has led to considerable interest in the research devoted to developing new materials for sensor devices. Since humidity is a prevalent component in our environment, measurements and control of humidity are essential for human comfort and a broad spectrum of industries and technologies. The constructive design of a good humidity sensor is a rather complicated topic due to its requirements, such as linear response, high sensitivity, fast response time, chemical and physical stability, wide operating humidity range, and low cost. Moreover, the sensor performance is strictly related to parameters like the chemical structure and the surface morphology of the developed sensor, which involve the adsorption/desorption process of water.

In this thesis, titanosilicate ETS-10 and vanadosilicate AM-6 zeotype materials in powder and film forms were synthesized to observe the effect of -V-O-V- and -Ti-O-Ti- wires on the humidity sensing behavior. The choice of material preparation allowed one to investigate the effect of different parameters on humidity sensing. These can be summarized as the effect of film thickness, crystallographic orientation, type of seed crystals, different defect formations within the quantum wires, and

lastly, vanadium doping in the ETS-10 structure. All samples were characterized by FE-SEM, XRD, Raman, and XPS analyses. For humidity sensing, a relative humidity experiment setup was designed with eleven saturated salt solutions with different relative humidity values. The determination of such humidity sensor parameters as sensor sensitivity and response time in constant humidity environments using saturated salt solutions was carried out via the impedance analyzer. The humidity sensors' sensitivity to variations in relative humidity values was determined according to the impedance data measured at certain frequencies.

In the first part of this study, titanosilicate ETS-10 and vanadosilicate AM-6 zeotypes powders were synthesized, and thin films were prepared by the spin coating method. The humidity sensing behavior of these two isostructural zeotypes shows high sensitivity at medium and high relative humidity levels.

In the second part of this thesis, to better understand the effect of the quantum wires and their orientation on humidity sensing behavior, ETS-10 and AM-6 films were prepared by the secondary growth method. For this purpose, ETS-10 powder was used as the seed layer. The humidity sensing performance of these films revealed that AM-6 films prepared by vanadyl sulfate as a vanadium source performed better than all prepared films at the whole relative humidity range.

In the last part of this thesis, to better understand the sensing mechanism, especially at low relative humidity levels, a structure with both vanadium and titanium atoms of differing coordinations in the quantum wire was investigated. This was accomplished by modifying titanosilicate ETS-10 by substituting vanadium into the structure. Sensors were prepared by spin coating methodology. Vanadium-doped samples with a V/Ti+V ratio of 0.2 showed better sensitivity at low relative humidity levels than other doped samples.

Keywords: Zeotypes, Humidity Sensing, Films preparation methods, Titanosilicates, Vanadosilicates, quantum wires

## ÖZ

### **NEM SENSÖRÜ UYGULAMALARI İÇİN MİKRO GÖZENEKLİ TİTANO/VANADOSİLİKAT ZEOTİP FİMLERİN SENTEZİ VE KARAKTERİZASYONU**

Davoudnezhad, Ramona  
Doktora, Mikro ve Nanoteknoloji  
Tez Yöneticisi: Prof. Dr. Burcu Akata Kurç  
Ortak Tez Yöneticisi: Prof. Dr. Necati Özkan

Aralık 2022, 120 sayfa

Çeşitli kimyasal moleküller için çevresel kontrole yönelik artan talep, sensör cihazları için yeni malzemeler geliştirmeye yönelik araştırmalara büyük ilgi duyulmasına yol açmıştır. Nem çevremizde yaygın bir unsur olduğundan, nemin ölçülmesi ve kontrolü insan konforu ve geniş bir endüstri ve teknoloji yelpazesi için gereklidir. İyi bir nem sensörünün geliştirici tasarımı, doğrusal tepki, yüksek hassasiyet, hızlı tepki süresi, kimyasal ve fiziksel kararlılık, geniş çalışma nem aralığı ve düşük maliyet gibi gereksinimleri nedeniyle oldukça karmaşık bir konudur. Ayrıca sensör performansı, geliştirilen sensörün kimyasal yapısı ve yüzey morfolojisi gibi suyun adsorpsiyon/desorpsiyon sürecini içeren parametrelerle sıkı sıkıya ilişkilidir.

Bu tezde, -V-O-V- ve -Ti-O-Ti- tellerinin nem algılama davranışı üzerindeki etkisini gözlemlemek için toz ve film formlarında titanosilikat ETS-10 ve vanadosilikat AM-6 zeotip malzemeleri sentezlenmiştir. Malzeme hazırlama seçimi, farklı parametrelerin nem algılama üzerindeki etkisinin araştırılmasına olanak sağlamıştır. Bunlar film kalınlığı, kristalografik yönelim, tohum kristallerinin türü, kuantum telleri içindeki farklı kusur oluşumları ve son olarak ETS-10 yapısındaki vanadyum

katkısının etkisi olarak özetlenebilir. Tüm numuneler FE-SEM, XRD, Raman ve XPS analizleri ile karakterize edilmiştir. Nem algılama için, farklı bağıl nem değerlerine sahip on bir doymuş tuz çözeltisi ile bir bağıl nem deney düzeneği tasarlanmıştır. Doymuş tuz çözeltileri kullanılarak sabit nem ortamlarında sensör hassasiyeti ve tepki süresi gibi nem sensörü parametrelerinin belirlenmesi empedans analizörü aracılığıyla gerçekleştirilmiştir. Nem sensörlerinin bağıl nem değerlerindeki değişimlere karşı hassasiyeti, belirli frekanslarda ölçülen empedans verilerine göre belirlenmiştir.

Bu çalışmanın ilk bölümünde titanosilikat ETS-10 ve vanadosilikat AM-6 zeotip tozları sentezlenmiş ve döndürmeli kaplama yöntemiyle ince filmler hazırlanmıştır. Bu iki izoyapılı zeotipin nem algılama davranışı orta ve yüksek bağıl nem seviyelerinde yüksek hassasiyet göstermiştir.

Bu tezin ikinci bölümünde, kuantum tellerinin ve yönelimlerinin nem algılama davranışı üzerindeki etkisini daha iyi anlamak için, ETS-10 ve AM-6 filmleri ikincil büyüme yöntemiyle hazırlanmıştır. Bu amaçla, tohum katmanı olarak ETS-10 tozu kullanılmıştır. Bu filmlerin nem algılama performansı, vanadyum kaynağı olarak vanadil sülfat ile hazırlanan AM-6 filmlerinin tüm bağıl nem aralığında hazırlanan tüm filmlerden daha iyi performans gösterdiğini ortaya koydu.

Bu tezin son bölümünde, kuantum telinde hem vanadyum hem de titanyum atomlarının farklı koordinasyonlara sahip olduğu bir yapı araştırılmıştır. Bu, titanosilikat ETS-10 yapısına vanadyum eklenerek modifiye edilmesiyle gerçekleştirilmiştir. Sensörler döndürmeli kaplama metodolojisi ile hazırlanmıştır.  $V/Ti+V=0.2$  miktarına sahip vanadyum katkılı örnekler, düşük bağıl nem seviyelerinde diğer katkılı örneklere göre daha iyi hassasiyet göstermiştir.

Anahtar Kelimeler: Zeotipler, Nem Algılama, Film hazırlama yöntemleri, Titanosilikatlar, Vanadosilikatlar, kuantum teli



*To my dear Family*

## ACKNOWLEDGMENTS

I would like to express my sincere gratitude to my supervisor, Prof. Dr. Burcu Akata Kurç, for her unwavering support, inspiration, and excellent guidance throughout my Ph.D. study. I am particularly thankful for the long evenings we spent discussing my research and her invaluable feedback on my writing.

I also want to thank the members of my thesis monitoring committee, Prof. Dr. Caner Durucan, and Assoc. Prof. Dr. Selis Önel, for their valuable comments and insights. Their guidance was instrumental in shaping the final version of my thesis.

I am grateful to my friends and labmates Nardin Avishan, Duygu Kuzyaka, Pelin Paşabeyoğlu, Kaan Kirdeciler, Melda İşler Binay, and Ahmad Saeed Khan for their friendship, support, and encouragement during my study. In particular I want to thank my labmate Cansu Gölboylu, who was there for me with a listening ear and supportive words. I will always remember the late nights we spent working in the lab and the long walks we took to clear our minds.

I am also thankful to Dr. Ibrahim Cam for his endless guidance on the humidity sensing measurement procedure.

Finally, I am grateful to the Scientific and Technical Research Council of Turkey (TÜBİTAK) for providing the financial support that made this study possible through project code 118M631. And, of course, I want to thank my parents, Mahin Hajizadeh and Fereidoun Davoudnezhad, and my sister Anahita Davoudnezhad for their never-ending love, patience, and support. I also want to thank again to my friend and sister Nardin Avishan for always being there. Without them, this thesis would not have been possible.

## TABLE OF CONTENTS

ABSTRACT.....	v
ÖZ.....	vii
ACKNOWLEDGMENTS.....	x
TABLE OF CONTENTS.....	xi
LIST OF TABLES.....	xv
LIST OF FIGURES.....	xvi
LIST OF ABBREVIATIONS.....	xx
CHAPTERS	
1 INTRODUCTION.....	1
1.1 Humidity.....	3
1.2 Humidity Sensing methods.....	4
1.2.1 Resistive type sensors.....	5
1.2.2 Capacitive type sensors.....	6
1.3 Sensing Materials.....	6
1.4 Impedance spectroscopy.....	7
1.5 Working principle and sensing mechanism of humidity sensors.....	8
1.6 Zeolites and Zeotype materials.....	12
1.6.1 Microporous Titanosilicate ETS-10.....	13
1.6.2 Microporous Vanadosilicate AM-6.....	15
2 LITERATURE REVIEW.....	17

2.1	Principle of humidity sensing for TiO <sub>2</sub> -based humidity sensor .....	17
2.2	Zeolite and zeotype-based materials in water sorption and humidity .....	20
2.3	Synthesis of titanosilicate ETS-10.....	24
2.4	Films Fabrication methods for Zeolites and Zeotypes .....	27
2.4.1	Thin Film Preparation of Zeolites and Zeo-type Materials: In situ and Secondary Growth Method.....	27
2.5	Goal and Objectives .....	34
3	EXPERIMENTAL PROCEDURE.....	37
3.1	The synthesis of ETS-10 and AM-6 crystals.....	37
3.1.1	The synthesis of nano-size ETS-10 crystals .....	38
3.1.2	The synthesis of nano-size AM-6 crystals .....	39
3.2	Thin Film Preparation.....	39
3.2.1	Production of ETS-10 and AM-6 thin films with various thicknesses over a glass substrate via the spin coating method .....	40
3.2.2	Production of ETS-10 films over various substrates via secondary growth method.....	41
3.2.3	Production of AM-6 films over various substrates through the second growth method, using different vanadium sources (VOSO <sub>4</sub> and V <sub>2</sub> O <sub>5</sub> ) .....	43
3.2.4	Synthesis of Vanadium-substituted ETS-10 Crystals.....	45
3.3	Humidity Sensor Experimental Setup .....	46
3.4	Analytical Techniques .....	50
3.4.1	Scanning electron microscope (SEM) .....	50
3.4.2	Raman spectroscopy .....	50
3.4.3	X-ray diffraction analysis (XRD) .....	50
3.4.4	Brunauer-Emmett-Teller (BET) .....	51

3.4.5	X-ray photoelectron spectroscopy (XPS).....	51
3.4.6	Impedance spectroscopy .....	52
4	INVESTIGATING THE HUMIDITY SENSING BEHAVIOR OF MICROPOROUS ETS-10 AND AM-6 THIN FILMS .....	53
4.1	Characterization of as-synthesized ETS-10 .....	53
4.2	Characterization of as synthesized AM-6 .....	55
4.3	ETS-10 ve AM-6 thin films prepared by spin-coating method .....	57
4.3.1	Humidity sensing behavior of ETS-10-2S and AM-6-2S films prepared by the spin coating method .....	59
5	HUMIDITY SENSING BEHAVIOR OF ETS-10 AND AM-6 FILMS PREPARED BY SECONDARY GROWTH METHOD .....	65
5.1	Preparation of ETS-10 films on various substrates by Secondary growth method.....	65
5.2	Preparation of ETS-10 films with different thicknesses by Secondary growth method.....	67
5.3	Effect of thickness of prepared films by secondary growth on humidity sensing performance .....	71
5.4	Preparation of AM-6 films with different gel formulations by Secondary growth method .....	74
5.5	Humidity sensing performance of AM-6 films prepared by different Secondary growth gel formulations .....	79
5.6	Complex impedance spectroscopy of films prepared by spin coating and Secondary growth methods.....	81
5.7	Effect of different film preparation methods on humidity sensing mechanism .....	83

6	TAILORING HUMIDITY SENSING BEHAVIOR OF TITANOSILICATES WITH Ti-O-Ti WIRES BY VANADIUM SUBSTITUTION .....	85
6.1	Characterization of as-synthesized ETS-10 and Vanadium substituted ETS-10 crystals.....	85
6.2	Humidity Sensing Performances of ETS-10 and its V-doped variations .....	94
6.3	Complex Impedance Spectra of Spin-coated ETS-10 sensors .....	97
6.4	Humidity Sensing Mechanism and effect of vanadium-doping .....	99
	SUMMARY and Conclusions .....	101
	REFERENCES .....	103
	CURRICULUM VITAE .....	119

## LIST OF TABLES

### TABLES

Table 3.1. List of the synthesized ETS-10 and AM-6 crystals and their synthesis conditions.....	38
Table 3.2. The experimental parameters of the films were obtained using the spin/dip coating method.....	40
Table 3.3. The experimental parameters of the films were prepared using ETS-10 as a seed layer with different thicknesses for the secondary growth method.....	41
Table 4.1 BET analysis of ETS-10 and AM-6 samples.....	57
Table 4.2. Thickness values of ETS-10-2S, AM-6-2S samples.....	59
Table 4.3. Response and recovery time of ETS-10-2S and AM-6-2S samples.....	62
Table 4.4. Thicknesses and Response and Recovery times of ETS-10-2S, ETS-10-4S, and ETS-10-8S samples.....	64
Table 5.1. Thicknesses and CPO values of 2S-TS, 1D-TS, and 2D-TS.....	69
Table 5.2. Thicknesses and response and recovery values of 2S-TS, 1D-TS, and 2D-TS.....	74
Table 5.3. Thicknesses and CPO values of 2S-VS <sub>1</sub> , 2S-VS <sub>2</sub> .....	76
Table 5.4. Response and recovery values of 2S-VS <sub>1</sub> and 2S-VS <sub>2</sub> . ....	81
Table 6.1 Bulk Atomic ratio of samples ETS-10, V <sub>0.1</sub> ETVS-10, V <sub>0.2</sub> ETVS-10, and V <sub>0.3</sub> ETVS-10.....	86

## LIST OF FIGURES

### FIGURES

Figure 1.1. Schematic of humidity sensor with interdigitated electrode [1]. .....	5
Figure 1.2. Nyquist diagram of the complex impedance of a humidity sensor, and equivalent electrical circuits when the sensor shows a) ionic conduction, b) mixed conduction, and c) electronic conduction [24], [25].....	8
Figure 1.3. “Donor effect” for n-type semiconductor with two possible mechanisms: (a) Electrons are attracted by the adsorbed water molecules to the semiconductor surface and the energy bands are bent; (b) Electrons are released by the competitive adsorption [2].....	10
Figure 1.4. Crystal structure of ETS-10, a) typical truncated-bipyramidal morphology of the crystals, which consist of a three-dimensional network of SiO <sub>2</sub> channels (blue) and TiO <sub>3</sub> <sup>2-</sup> molecular wires (red), b) view along the [1 $\bar{1}$ 0] axis, c) view along the [110] axis, d) a single TiO <sub>3</sub> <sup>2-</sup> molecular wire [9].....	14
Figure 1.5. Structural model of AM-6 [48]. .....	15
Figure 2.1. Schematic illustration of TiO <sub>2</sub> humidity sensing mechanism [56]. .....	19
Figure 2.2. Possible sites of water molecules adsorbed on HZSM-5 zeolite [57]...20	20
Figure 2.3. Proposed mechanisms of ETS-10 crystallization with P25 as the Ti source [39].....	25
Figure 2.4. schematic of films prepared by (a) Spin coating and (b) Secondary growth technique. ....	28
Figure 2.5. XRD patterns of ETS-10 in powder form and ETS-10 membrane [85]. .....	30
Figure 2.6. XRD patterns of bare ITO glass substrate (a), ETS-10 powder (b), seed layers deposited on the ITO glass substrate using 1 (c), 2 (d), and 3 (e) dip coating steps, and films after secondary growth of seed layers deposited via single (f), double (g), and triple (h) dip coating [78]. ....	31
Figure 3.1. The schematic illustration of ETS-10 film production process using the second growth method [92]. ....	43



Figure 3.2. A schematic illustration of the process of obtaining humidity sensors from ETS-10 or AM-6 thin films over substrates using the spin-coating method..	46
Figure 3.3. A schematic illustration for obtaining humidity sensors from ETS-10 or AM-6 films created using spin-coating and second-growth methods.....	47
Figure 3.4. The schematic illustration of the humidity sensing experimental design (a), the film-impedance system (b), and the calibration setup with Testo 176H1 humidity sensor (c). .....	47
Figure 3.5. Schematic of humidity sensing setup. ....	49
Figure 4.1. The FE-SEM image (a) and X-ray diffraction patterns (b) of ETS-10 crystals. ....	53
Figure 4.2. Raman spectra of ETS-10 crystals.....	54
Figure 4.3. The FE-SEM image (a), X-ray diffraction patterns (b) of AM-6 crystals. ....	55
Figure 4.4. Raman spectra of AM-6 crystals. ....	56
Figure 4.5. Top view and cross-sectional SEM images of ETS-10-2S (a),(b); AM-6-2S (c),(d), respectively.....	58
Figure 4.6. Relationship between impedance modulus and RH values at different frequencies for ETS-10-2S (a) and AM-6-2S (b) sensors.....	60
Figure 4.7. Variation of the impedance of ETS-10-2S and AM-6-2S sensor as a function of change in relative humidity at 100 Hz. The tables in each figure are derived from fitting the curves in the whole range (a,b,c); response and recovery times of both samples (d).....	61
Figure 4.8. Impedance vs RH% response (a) and response and recovery plot (b) of ETS-10-2S, ETS-10-4S and ETS-10-8S samples at 100 Hz frequency. ....	63
Figure 5.1. FE-SEM images ETS-10 secondary growth films on a window glass (a), microscope glass (b), borosilicate glass (c), and alkali-free glass (d) substrates. ....	66
Figure 5.2. Top view and cross-sectional SEM images of 2S-TS (a), (d), 1D-TS (b), (e), and 2D-TS (c), (f). ....	67

Figure 5.3. X-ray diffraction patterns of ETS-10 powder (a), 2S-TS (b), 1D-TS (c), and 2D-TS (d) films.....	69
Figure 5.4. Relationship between impedance modulus and RH at different frequencies for 2S-TS (a), 1D-TS (b), and 2D-TS (c) sensors, comparison of impedance vs. RH% response of 2S-TS, 1D-TS, and 2D-TS at 100 Hz.....	71
Figure 5.5. Response and recovery performance of 2S-TS (a), 1D-TS (b), and 2D-TS (c) sensors by changing relative humidity levels from 30% (dry environment) and 90% (high humidity environment), 2S-TS, 1D-TS, and 2D-TS sensors' response and recovery (d).....	73
Figure 5.6. Top view and cross-sectional SEM images of 2S-VS <sub>1</sub> (a), (b), 2S-VS <sub>2</sub> (c), (d). .....	75
Figure 5.7. XRD patterns of ETS-10 powder (a), 2S-VS <sub>1</sub> (b), and 2S-VS <sub>2</sub> (c) films. ....	76
Figure 5.8. Raman spectra of 2S-VS <sub>1</sub> (a), 2S-VS <sub>2</sub> (b) films. ....	77
Figure 5.9. Relationship between impedance modulus and RH at different frequencies for 2S-VS <sub>1</sub> (a), 2S-VS <sub>2</sub> (b).....	80
Figure 5.10. Response and recovery performance of 2S-VS <sub>1</sub> (a) and 2S-VS <sub>2</sub> (b) sensors by changing relative humidity levels from 30% (dry environment) and 90% (high humidity environment).....	81
Figure 5.11. CIS measurements of sensors prepared by spin coating and secondary growth film production method at 11.32% (a) 52.89% (b) 93.58% (c) RH levels..	83
Figure 5.12. Schematic of water filling in the films prepared by spin-coated and secondary growth at high (a-d), moderate (b-e), and low (c-f)relative humidities. 84	
Figure 6.1. XRD patterns of ETS-10 (a), V <sub>0.1</sub> ETS-10 (b), V <sub>0.2</sub> ETS-10 (c), V <sub>0.3</sub> ETS-10(d) (*quartz, #anatase) impurities.....	85
Figure 6.2. Raman spectra of ETS-10, V <sub>0.1</sub> ETS-10, V <sub>0.2</sub> ETS-10, and V <sub>0.3</sub> ETS-10.	88
Figure 6.3. SEM images of ETS-10 (a), V <sub>0.1</sub> -ETS-10 (b), V <sub>0.2</sub> -ETS-10 (c), and V <sub>0.3</sub> -ETS-10 (d). .....	89
Figure 6.4. XPS spectra of Ti(2p <sub>3/2</sub> ) binding energies of ETS-10 and vanadium-substituted ETS-10 samples. ....	90

Figure 6.5. XPS spectra of V(2p <sub>3/2</sub> ) binding energies of vanadium-substituted ETS-10 samples.....	91
Figure 6.6. XPS spectra of O 1s binding energies of vanadium-substituted ETS-10 samples.....	93
Figure 6.7. Relationship between impedance modulus and RH (a), and response recovery performance of ETS-10 and V-doped ETS-10 sensors at 100Hz frequency (b).....	94
Figure 6.8. Relationship between impedance modulus and RH for all sensors due to their slopes at 100 Hz frequency.....	96
Figure 6.9. Complex impedance spectra of V <sub>0.2</sub> ETS-10 at various relative humidity values. ....	97
Figure 6.10. Impedance–frequency characteristics of the sensor at different RH levels. R <sub>f</sub> : film resistance; C <sub>f</sub> : film capacitance; Z <sub>w</sub> : Warburg impedance. ....	98
Figure 6.11. The theoretical model for water adsorption on the surface of the sensor. ....	100

## LIST OF ABBREVIATIONS

### ABBREVIATIONS

FE-SEM	Field Emission Scanning Electron Microscopy
XRD	X-ray Diffraction
XPS	X-ray Photoelectron Spectroscopy
BET	Brunauer-Emmett-Teller
CPO	Crystallographic Preferred Orientation
ETS-10	Engelhard Titanosilicate-10
AM-6	Aveiro-Manchester-6
VOSO <sub>4</sub>	Vanadyl Sulfate
V <sub>2</sub> O <sub>5</sub>	Vanadium Pentoxide
P25	Degussa Titanium Dioxide

## CHAPTER 1

### INTRODUCTION

There has been a rapid increase in developing sensors for monitoring moisture, temperature, and chemical gases in various application fields. Humidity sensors hold an imperative role due to increased demand for the control of the indoor ambient environment, food and medicine storage, agriculture, health, industry, textile, and even space environments. The research in humidity sensors faces the profound challenge of sensing humidity variation in the whole humidity range of 0-100% relative humidity (RH), resulting in increased research devoted to developing new materials for humidity sensing applications. The constructive design of a high-performance humidity sensor is a rather complicated topic due to various design factors, such as linear response, high sensitivity, fast response and recovery times, chemical and physical stability, wide operating humidity range, and low cost.

Tailoring active materials' sensing properties that show sensitivity in a broader range of humidity is a profound challenge in improving the performance of humidity sensors. The most common sensing materials studied for humidity sensing are ceramics, metal oxides (semiconductors), polymers, and ceramic/polymers [1], [2]. Among them, metal oxide semiconductor materials such as ZnO, TiO<sub>2</sub>, VO<sub>2</sub>, CuO, and Al<sub>2</sub>O<sub>3</sub> are widely used for sensor development due to their facile synthesis method, high operational stability, and low cost [3].

Titanium dioxide (TiO<sub>2</sub>) was shown to be of particular interest due to its high response in electrical conductivity, hydrophilicity, wide resistivity range, and high chemical and thermal stability [2].

However, reported TiO<sub>2</sub>-based humidity sensors showed low sensitivity at a low relative humidity range. Therefore, many challenges have been performed to

improve the sensitivity of TiO<sub>2</sub> by using various production methods or modifying the structure by doping transition metals [4]–[8].

An opportunity to tune the humidity sensing performance can be achieved using Ti-based molecular sieves with a high surface area and tunable defect sites readily available in their structure. Engelhard titanosilicate (ETS-10) is a microporous zeotype material that contains periodically positioned -Ti-O-Ti- chains with a diameter ( $d$ ) of  $\sim 0.67$  nm running along two orthogonal directions, surrounded by tetrahedral silicate units [9]. Among other molecular sieves, ETS-10 has been the subject of extensive research due to these quantum wires that impart some fascinating properties [9], [10]. AM-6 is another microporous vanadosilicate that is isostructural to titanosilicate ETS-10, except its -V-O-V- chains were replaced with -Ti-O-Ti- chains in ETS-10 [11], [12]. Therefore, these zeotype materials could be suitable for humidity sensing applications.

This thesis investigates the humidity sensing behavior of Titano/Vanadosilicates zeotypes prepared by different film production techniques. In the first part of this study, Titanosilicate ETS-10 and Vanadosilicate AM-6 zeotypes powders were synthesized to observe the effect of -V-O-V- and -Ti-O-Ti- on the humidity sensing behavior of these two isostructural zeotypes. For this purpose, thin films were prepared by the spin coating method.

In the second part of this thesis, to better understand the effect of the quantum wires and their orientation on humidity sensing behavior, ETS-10 films were prepared by the secondary growth method. For this purpose, ETS-10 powder was used as the seed layer. Two different coating methods were used to understand the effect of the seed coating technique on crystallographic preferred orientation (CPO) and thickness of prepared films and its impact on the humidity sensing behavior of sensors.

Secondly, rather than ETS-10 with titanosilicate quantum wires, vanadosilicate AM-6 thin films possessing -V-O-V- wires using ETS-10 as a seed layer were also prepared. This approach allowed one to investigate the effect of -V-O-V- wires in

the structure and, thus, the effect of the vanadium source on the humidity-sensing behavior of prepared sensors.

The last part of this thesis investigates a structure with both vanadium and titanium atoms of differing coordinations in the quantum wire. This was accomplished by modifying Titanosilicate ETS-10 by substituting Vanadium into the structure during the synthesis. Vanadium doping allowed one to investigate the effect of “V-O-Ti” connections and to optimize the Ti/V amount with hopefully the proper coordination on the humidity sensing behavior of the prepared sensors using spin coating methodology.

## 1.1 Humidity

The amount of water vapor in any gaseous atmosphere is known as humidity. Some terms frequently appear in this context: Relative Humidity (RH), Parts Per Million (PPM) by weight or by volume, and Dew/Frost Point (D/F PT), two latter terms being subclasses of Absolute Humidity (AB) [2]. As a direct assessment of the value of the water vapor content is possible, Absolute Humidity units are applicable for the primary measurement results. On the contrary, since the measurement of the water vapor values is mediated in some manner, Relative Humidity is accurate for the secondary measurement results. Absolute Humidity, also known as vapor density, is defined as the ratio of the mass of water vapor in the atmosphere to the volume of the air, with the unit of grams per cubic meter or grains per cubic foot (1 grain = 1/7000 pound lb) [1], [2]. Absolute Humidity, in mathematical terms, is expressed as

$$AB = \frac{m_w}{v}$$

Where  $AB$  is the absolute humidity ( $\text{g/m}^3$  or  $\text{grains/ft}^3$ ),  $m_w$  is the mass of water vapor (gram or grain), and  $v$  is the volume of air ( $\text{m}^3$  or  $\text{ft}^3$ ). On the other hand, Relative Humidity (abbreviated as RH) is defined as the ratio of the amount of moisture in the atmosphere to the maximum (saturated) moisture level that the air can maintain

at an equivalent temperature and pressure. RH is a relative measurement since it is a temperature-dependent magnitude. It is stated as a percentage and determined according to the following formula:

$$RH\% = \frac{P_v}{P_s} \times 100$$

where  $P_v$  is the actual partial pressure of moisture content in the atmosphere, and  $P_s$  is the saturated pressure of moist air at an equivalent temperature (both measured in Bar or KPa). Finally, Saturation Humidity is defined as the ratio of the mass of the water vapor at the saturation level to the volume of the air.

These days, RH sensors are extensively commercialized, and research in the area of humidity sensors is confronted by the profound challenge of measuring humidity variation in the entire range of 0-100% Relative Humidity (RH). Which, in turn, requires a huge academic enterprise dedicated to developing new materials for humidity sensing applications.

## **1.2 Humidity Sensing methods**

Decades of implementation of humidity sensor design configurations have led to the consensus among the engineering community that the impedance-(resistive) and capacitive-based sensors are the most appropriate ones for advanced applications, for instance, in the area of experimental research [1], [2], [13]. There are various reasons for such popularity, such as their ability to fulfill the general requirements of the task at hand, including simpler structure, free choice of sensing elements among various available types, cost, adaptability to different types of circuits, and ease of fabrication and measurement setup.



### 1.2.1 Resistive type sensors

Standard resistive type humidity sensors contain noble, precious metal electrodes either deposited on a glass or ceramic substrate by thick film printing techniques or thin film deposition [14], [15]. Regarding resistive sensors, the design configuration is mostly based on interdigitated (interdigital) electrodes [16] in which the humidity-sensitive films are deposited at the gap between the fingers, as shown in Figure 1.1. Occasionally, the film-based sensors are constructed through the application of several different printing techniques, e.g., screen or inkjet printing, and coating techniques, like chemical vapor deposition (CVD) methods such as spin coating and dip coating. Another example can be physical vapor deposition (PVD) techniques such as thermal evaporation and cold sputtering [17]. The function of resistive sensors is to measure the variations of humidity and translate them into a variation in the electrical impedance of the hygroscopic medium. Characteristically, the resistance variation to humidity follows an inverse exponential relation, yielding an approximate range of  $1\text{K}\Omega$  to  $100\text{M}\Omega$ . Essentially, the water vapor, upon adsorption, is dissociated on a molecular level into ionic functional hydroxyl groups, increasing conductance[1]. Figure 1.1 illustrates a prototypical sketch of a planar thick/thin film humidity sensor based on the interdigitated structure with the porous membrane.

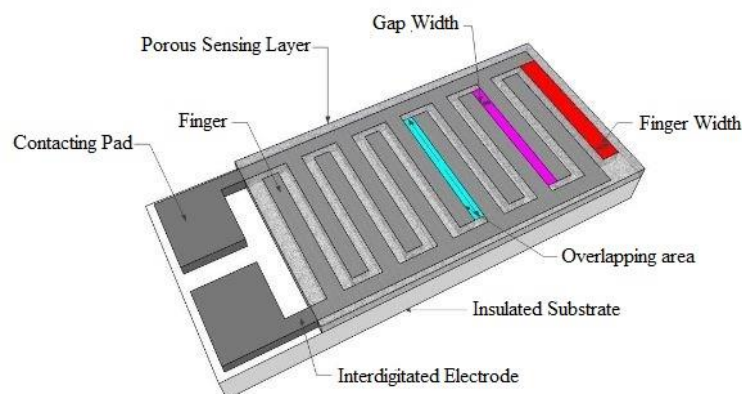


Figure 1.1. Schematic of humidity sensor with interdigitated electrode [1].

### **1.2.2 Capacitive type sensors**

In terms of design configuration, the capacitive humidity sensors may possess either a sandwiched structure with two electrode surfaces on each side or an interdigitated structure with comb electrodes, as in resistive RH sensors, in such a manner that the dielectric polymer film is deposited in between [1], [2]. Multiple capacitive RH sensors have been designed and manufactured on interdigitated gold, platinum, or silver electrodes. This platform incorporates organic polymer thin films or porous ceramics such as alumina, perovskites, and porous silicon based on printing deposition or coating techniques onto a ceramic substrate [18], [19]. Typically, the parallel plate structure consists of two metal electrodes deposited on the substrate and coated with a thin film layer of a dielectric polymer or a porous ceramic metal oxide. As an upper electrode, the top of the sensing surface is coated with a thin layer of evaporated gold to shield it from ambient contamination or dust and help guarantee a more appropriate condensation. In the sandwich design configuration, the upper porous electrode universally consists of a water vapor permeable film [20].

### **1.3 Sensing Materials**

Polymer electrolytes or polymer–salt complexes are used for resistive-type sensors, and hydrophobic polymers are preferred for capacitive-type sensors. Their working principle is regarding changes in their specific electrical conductance or dielectric permittivity following interaction with H<sub>2</sub>O at ambient temperature [21]. However, polymer-based sensors generally offer cost-effectiveness and acceptable sensitivity, and almost all work correctly only at room temperature. This limitation is due to the high sensitivity of polymers to heat. Other problems like limited operation in harsh and chemical environments and weak adhesion to polymeric substrates result in slow response times and short shelf lives. Among the various types of humidity sensors, semiconducting metal oxide and metal oxide/polymer-based sensors, mainly produced by thick film and thin film deposition techniques, are prevalent. These

materials are noteworthy due to their variety of sensitive element choices, post-processing, and greater response characteristics. Compared with polymer-based thin or thick film humidity sensors, the synthesis process of ceramics is more straightforward, and they frequently reveal fast response times. These sensors are operational over a wide range of humidity with instrumental response characteristics and possess the potential of being commercially available for medium to high-volume demands. Most recent nanostructured semiconductor metal oxides are based on zinc oxide (ZnO), titanium dioxide (TiO<sub>2</sub>), tungsten trioxide (WO<sub>3</sub>), copper oxide (CuO and Cu<sub>2</sub>O), tin oxide (SnO and SnO<sub>2</sub>), and vanadium oxide (VO<sub>2</sub> and V<sub>2</sub>O<sub>5</sub>), in the form of nanoparticles or as continuous films or layers [1], [3], [22].

Moreover, these sensors are divided into two groups according to their sensing mechanisms, i.e., impedance (resistive) or capacitive categories; the former uses the conductance properties, and the latter the capacitance properties of the sensing layer. Impedance-based sensors are subdivided into ionic conduction and electronic conduction. The primary issue with ceramic humidity sensors is the requirement for periodic heating to eliminate impurities such as dust and grease [21]. However, the majority of ionic-type ceramic sensors were designed without a heater and operated at ambient temperature.

#### **1.4 Impedance spectroscopy**

When a material's conductivity is ionic or mixed (i.e., electronic and ionic), impedance spectroscopy is the preferred method for measuring conductivity. Consequently, the system's response to a periodic small ac signal was measured at varied ac frequencies (typically 10 Hz–10 MHz). Studying the detected response can provide informational insight regarding the sample [23] Recording complex impedance data requires the utilization of equivalent circuits with R for resistance,  $1/j\omega C$  for capacitance, and  $j\omega L$  for inductance.

Figure 1.2 shows the typical complex impedance spectroscopy of a humidity sensor. In this figure, X ( $Z'$ ) axis is the real part, and the y ( $Z''$ ) axis is the imaginary part of the impedance ( $Z$ ). Every data point needs to be measured in a different frequency named Nyquist plot. As mentioned above, this plot can be shown as a combination of parallel resistors and capacitors in an equivalent circuit.

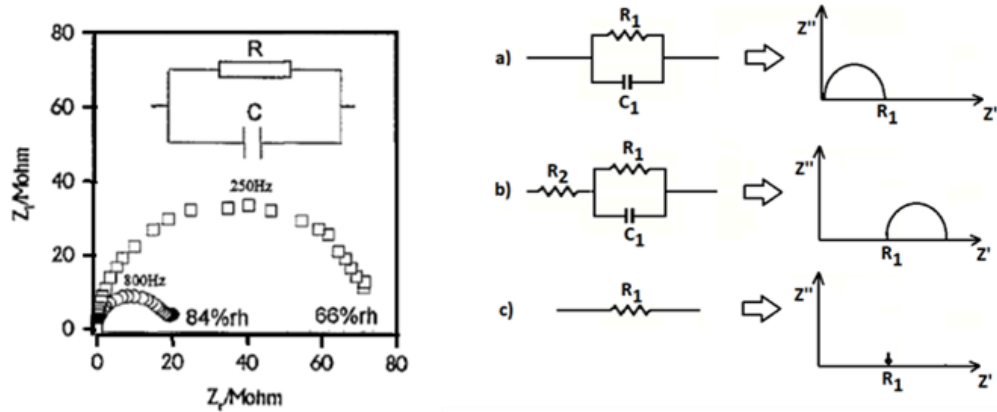


Figure 1.2. Nyquist diagram of the complex impedance of a humidity sensor, and equivalent electrical circuits when the sensor shows a) ionic conduction, b) mixed conduction, and c) electronic conduction [24], [25].

### 1.5 Working principle and sensing mechanism of humidity sensors

Most of the porous polymer and ceramic film sensing principles are quite similar. The working principle of a resistive type humidity sensor includes the change in the impedance due to exposing the sensor's surface to various relative humidity ranges. The difference in impedance was shown to happen by both ionic conduction and electronic conduction [2]. Accordingly, the porous structure of the sensor and their surface reactivity with the humidity have leading roles in the humidity sensing performance. When the sensor's surface is exposed to moisture, a few water vapor molecules are chemically adsorbed (chemisorption) on the surface active sites. At this stage, water molecules dissociate to form hydroxyl groups (two hydroxyl ions per water molecule). The film's first layer of physisorbed water molecules is formed

via hydrogen bonding on the two neighboring hydroxyl groups as water condenses on the surface. Increasing the relative humidity, an extra layer of water forms on top of the first physically adsorbed layer. Due to the high electrostatic fields in the chemisorbed layer, water molecules dissociate from physisorbed water, and  $\text{H}_3\text{O}^+$  (hydronium) groups are created. Charge transfer occurs when  $\text{H}_3\text{O}^+$  releases a proton to an adjacent  $\text{H}_2\text{O}$  molecule. Consequently, this water molecule is ionized, and another  $\text{H}_3\text{O}^+$  results in the proton hopping from one water molecule to the next. This process is known as the Grotthuss mechanism, and it is assumed that it also represents the conduction mechanism in liquid water [26].

The higher resistivity of the oxides at lower RH values is related to the number of water molecule adsorption sites, which may be increased by defect lattice sites and oxygen vacancies at the surface [27]. For ceramic humidity sensors at low RH levels, the proton hopping mechanism seems to be ineffective due to the immobilized nature of the chemisorbed and the first physisorbed layers. At this stage of low RH level, another phenomenon named the tunneling effect comes into play, where the electron can tunnel between donor water sites [28]. Due to this theory, the energy induced by the surface anions facilitates electrons to hop along the surface covered by the immobile layers, contributing to the conductivity.

For semiconductors, a high RH level results in an increase in the conductivity of n-type sensors, whereas a decrease in the conductivity of p-type sensors [3]. For semiconductors at low RH levels, the conduction mechanism occurs due to the transfer of electrons from chemically adsorbed water molecules to the surface [29]. Another theory claims water molecules replace the previously adsorbed oxygen ( $\text{O}^-$ ,  $\text{O}^{2-}$ , etc.) and release the electrons from the ionized oxygen [30]. A depletion layer is formed in both cases, called the “donor effect.” In this case, the electrons at the surface play a significant role in the humidity sensing mechanism rather than proton hopping occurring within the adsorbed water layer. As shown in Figure 1.3-a preferential alignment of the water dipoles increases surface electron accumulation which causes the enhancement of conductivity. In Figure 1.3-b, a depletion layer

forms due to adsorbed oxygen, which may be neutralized by releasing electrons for n-type semiconductors [2]. Because the conductivity is caused by the concentration of electrons at the surface, this sensing style is usually called the “electronic type.” However, as mentioned above, at increased RH levels, proton hopping is the main conduction mechanism due to the physisorption of water molecules. In summary, different mechanisms seem dominant at low and high RH levels. Therefore, different materials with tailored sensing mechanisms must be developed for successful humidity sensing in the whole RH region.

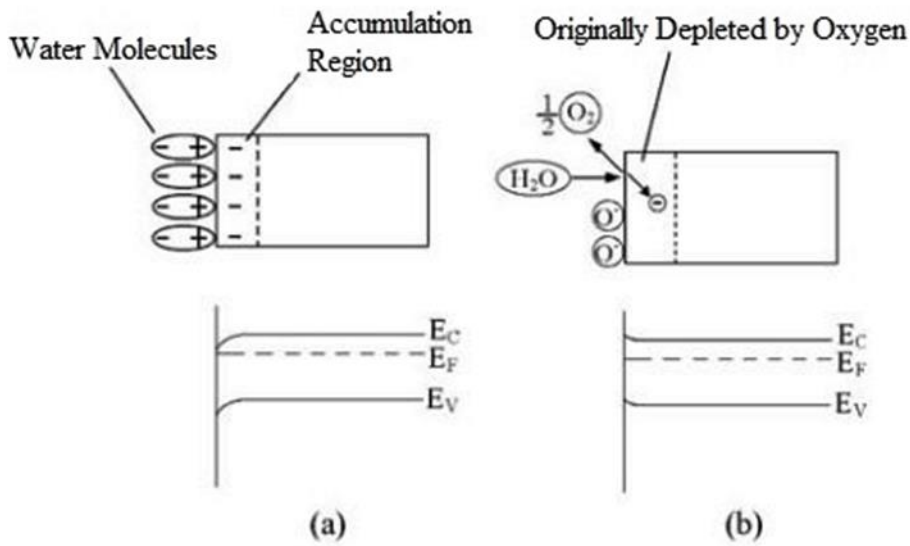


Figure 1.3. “Donor effect” for n-type semiconductor with two possible mechanisms: (a) Electrons are attracted by the adsorbed water molecules to the semiconductor surface and the energy bands are bent; (b) Electrons are released by the competitive adsorption [2].

TiO<sub>2</sub> is a material with a broad energy bandgap, often showing optical band gaps of 3.0 and 3.2 eV for rutile and anatase, respectively. TiO<sub>2</sub> is also known as titanium dioxide. There have been reports of a high dielectric constant for TiO<sub>2</sub> thin films ranging from 40–86, as well as a high resistivity extending to 10<sup>8</sup> Ω.cm [3]. TiO<sub>2</sub> has been widely used in various industries as a photoactive layer of gas sensors.

These sensors are usually chemiresistive, with an n-type semiconductor conductance change mechanism based on the adsorption/desorption process of oxidizing and reducing gases [31]. The well-ordered porous metal oxide structures of TiO<sub>2</sub> improve gas sensing by increasing the material's surface area, enhancing interaction with the gaseous species. For TiO<sub>2</sub>-based humidity sensor surface defects, such as Ti<sup>3+</sup> defect sites or oxygen vacancy sites, could improve the sensing by adsorbing water molecules [32]. While reports of TiO<sub>2</sub>-based humidity sensors abound, they often exhibit low sensitivity due to the single-phased TiO<sub>2</sub> material's poor charge transfer mechanism, high resistance, or low surface-to-volume ratio.

Compared to pure TiO<sub>2</sub> and SiO<sub>2</sub> compounds, the water sorption activity and capacity of Titanosilicates (TiSi) are much higher due to octahedrally coordinated Ti in the mixed oxide materials. Sosnov et al. revealed the higher water sorption of amorphous TiSi with high TiO<sub>2</sub> concentration is related to a high amount of surface hydrolytically unstable titanosiloxanes (Si-O-Ti) [33]. This fact is explained by the high tendency of Si-O-Ti bonds to undergo hydrolysis during water sorption, thus producing Si-OH and Ti-OH, which are responsible for the subsequent sorption of water molecules. Another study showed the improvement of the water sorption capacity of TS-1 by increasing the amount of the framework titanium. However, the high titanium leads to anatase formation and decreases the final material's pore volume [34]. This information makes titanosilicate a good candidate for humidity sensing applications.

On the other hand, a low dimensional nanostructure with a high surface-to-volume ratio demonstrating a drastic change of resistances on the adsorption of a water molecule could improve the sensing performance of humidity sensors.

ETS-10, one of the most popular TiSi zeotypes, could be a good candidate for humidity sensing with fascinating properties like -Ti-O-Ti- quantum wires make ETS-10 act as a semiconductor and facilitate the conduction along chains.

## 1.6 Zeolites and Zeotype materials

Zeolites are crystalline aluminosilicates composed of  $\text{SiO}_4$  and  $\text{AlO}_4$  tetrahedra arranged in a three-dimensional framework to generate pores of molecular diameters. The structure of zeolites is negatively charged due to the substitution of  $\text{Al}^{3+}$  with  $\text{Si}^{4+}$  at certain sites. The extra framework cations are in the cavities of the neutralized zeolite [35].

The unique properties of zeolites, such as ion exchange, catalytic activity, and sorption capacity, make them so fascinating to the industry. There are many parameters that are tailorable for modifying the properties of zeolite for different applications. For example the size of the pores affects the sorption property, the number of extra framework cations and pore openings affects the ion exchange capability, and Si/Al ratio affects the acidity and catalytic activity

Zeolites are categorized according to their framework types using codes like FAU, LTA, MFI, etc. [35]. These framework types can be followed from the published data in the *Atlas of Zeolite Framework Types* [36], [37] The information about the pores, the connection of the tetrahedral atoms, and the channel system can be obtained from the framework type [30].

Zeolites consist of  $\text{TO}_4$  tetrahedra (T representing any tetrahedrally coordinated cation) with 2- to 3-dimensional channels and cavities. The size of the pore openings in zeolite structure is defined by the number of T-atoms enclosing these pores; for instance, an 8-ring structure is a small pore opening [35]. The pores of zeolite are flexible, and pore and cavity dimensions are affected by the type of cation. In order to measure the dimensions of zeolites, it would be more accurate to mention the "effective" pore size, which could be 110 % of the crystallographic dimensions of zeolites [36], [37]. Moreover, it is possible to modify the catalytic and ion-exchange characteristics of zeolites by changing the framework composition or type and/or the number of extra framework cations [37]. Extra framework cations originated from



the synthesis mixture, or post-synthesis treatments present in the channels and cages of the zeolite framework are necessary to balance the electronegativity [35].

Materials with T atoms other than Al, like Ga, B, Ti, Cr, V, and P in their structures, are called zeotypes. These materials have microporous or mesoporous structures consisting of hexagonal, elliptical, spherical, or parallel channels.

### 1.6.1 Microporous Titanosilicate ETS-10

Engelhard titanosilicate (ETS-10) was first synthesized by Engelhard in 1989. ETS-10 is a synthetic microporous (pore dimensions; 4.9 Å and 7.6 Å) crystalline zeotype material. In the ETS-10 framework, the oxygen atoms bridge the corner-sharing TiO<sub>6</sub> octahedra and SiO<sub>4</sub> tetrahedra [38]. ETS has non-intersecting orthogonal monatomic linear chains (-O-Ti-O-Ti-O-), which take the shape of semiconducting 1D TiO<sub>3</sub><sup>2-</sup> quantum wires with 0.67 nm diameter (Figure 1.4) [9]. ETS-10 framework consists of a three-dimensional network of interconnected channels, cavities, and corner-sharing TiO<sub>6</sub> and SiO<sub>4</sub>. The 12-membered ring pore system of ETS-10 has dimensions of 7.6 Å × 4.9 Å [39]–[41]. ETS-10, with its unique properties like balancing the net negative charge of the framework due to the presence of non-framework cations, and pore uniformity, make it a promising candidate for catalytic, ion-exchange, adsorption, and separation applications. The monoatomic -Ti-O-Ti-O-Ti- chains of ETS-10 extend in both *a* and *b* directions, separated by a silica matrix [[9]

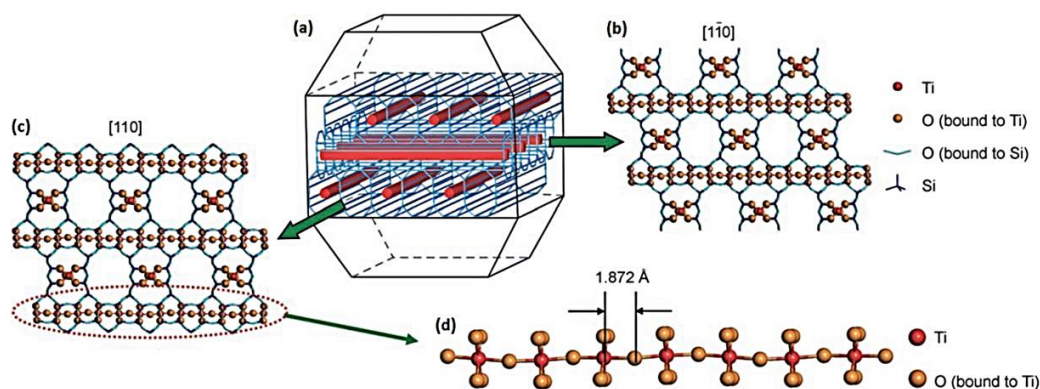


Figure 1.4. Crystal structure of ETS-10, a) typical truncated-bipyramidal morphology of the crystals, which consist of a three-dimensional network of  $\text{SiO}_2$  channels (blue) and  $\text{TiO}_3^{2-}$  molecular wires (red), b) view along the  $[\bar{1}10]$  axis, c) view along the  $[110]$  axis, d) a single  $\text{TiO}_3^{2-}$  molecular wire [9].

The novel one-dimensional (1D) semiconductor quantum-confined materials are promising for nanoscale electronic devices and applications. The thinnest 1D quantum-confined materials are quantum wires, and the -Ti-O-Ti- chains in ETS-10 are one example of quantum wires [9]. The extra-framework cations balance the two negative charges carried by each Ti atom in the chain. Moreover, the extra-framework cations in ETS-10 are exchangeable cations ( $\text{Na}^+$  and  $\text{K}^+$ ) which results in high cation-exchange capacity [39].

The ETS-10 crystals grow via two-dimensional surface nucleation [39], [42], [43]. According to this mechanism, “layer-by-layer” ETS-10 crystals grow from multiple surface nuclei, which results in layer-by-layer stacking and orthogonal coordination of Ti-O-Ti between the adjacent wires [39], [43]. These wires break at random points due to defects in ETS-10, probably because of the meeting of numerous spreading surface nuclei to build consecutive layers on top of each other (layer-by-layer ETS-10 crystal growth mechanism) [43]. These defects cause a considerable disorder due to different stacking sequences, which lead to the broadening of pores up to 2 nm in ETS-10 [44], [45].

### 1.6.2 Microporous Vanadosilicate AM-6

Microporous Vanadosilicate AM-6 (Aveiro/Manchester no. 6) is an isostructural of ETS-10. AM-6 consists of a monatomic semiconductor -V-O-V- chain instead of -Ti-O-Ti- chain separated by a silica matrix [46]. The unit cell composition of AM-6 is  $(\text{Na}, \text{K})_2\text{VSi}_5\text{O}_{13}\cdot 3\text{H}_2\text{O}$ , and it has micropores with opening dimensions of approximately  $4.9 \times 7.6 \text{ \AA}$  [46]. Corner-sharing  $\text{VO}_6$  octahedra and  $\text{SiO}_4$  tetrahedra make up the AM-6 structure. Due to its distinctive properties, such as microporosity, pore regularity, and the presence of vanadium, AM-6 could potentially be used in catalysis, gas separation, and sorption applications [12], [47]. The 3-dimensional pore structure in vanadosilicate AM-6 is composed of 12-, 7-, 5-, and 3-membered rings. Vanadium ions are placed octahedrally in the structure by four Si-O and two V-O bonds, as shown in Figure 1.5.

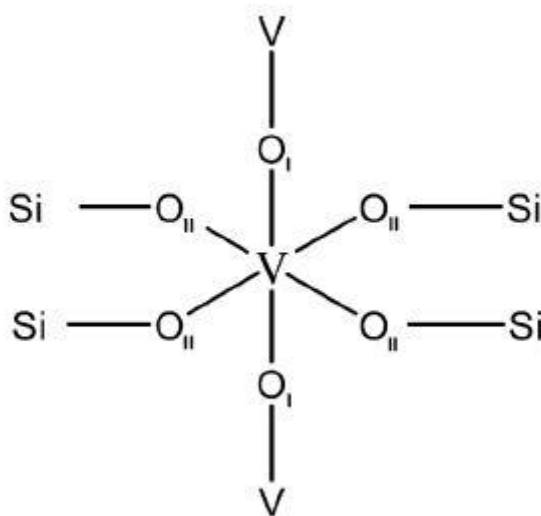


Figure 1.5. Structural model of AM-6 [48].

Due to the literature, there are various recipes for synthesizing AM-6. Rocha et al. used isostructure ETS-10 as a seed for the growth of AM-6 crystals. This method obtains an ETS-10/AM-6 core-shell structure with a small amount of quartz as an impurity and both  $\text{V}^{4+}$  and  $\text{V}^{5+}$  states [12]. Ismail et al. introduced a new recipe without ETS-10 as a seed, and the synthesis method resulted in AM-6 crystals with

both  $V^{4+}$  and  $V^{5+}$  states again [47]. In 2012, Jit Datta and his team successfully synthesized seedless, pure monodisperse, and high-quality AM-6 crystals from  $V_2O_5$  with only  $V^{IV}$  in the quantum wires [49]. After that, Mani et al. produced a new recipe with  $VSO_4$  and used the EVS-10 code name for AM-6 [50].

## CHAPTER 2

### LITERATURE REVIEW

#### 2.1 Principle of humidity sensing for TiO<sub>2</sub>-based humidity sensor

TiO<sub>2</sub> is the most studied material for many applications, such as photocatalysis, gas sensors, and humidity sensors, due to its high electrochemical stability, hydrophilicity, and surface roughness [3]. TiO<sub>2</sub> has three phases, anatase, brookite, and rutile, which identify it as an n-type transition metal oxide semiconductor. The anatase and rutile phases are more stable than the brookite phase. The structures of anatase and rutile are tetragonal, whereas brookite has an orthorhombic structure [3].

Reported TiO<sub>2</sub>-based sensors display limited sensitivity for humidity sensing applications. This is due to a low surface-to-volume ratio, high resistance, or poor charge transfer process of single-phased TiO<sub>2</sub> material [3], [51]. In order to overcome these limitations, defect sites like Ti<sup>3+</sup> and /or the oxygen vacancies on the surface of TiO<sub>2</sub> can be tailored [51]. At low RH levels, oxygen vacancies and surface Ti<sup>3+</sup> are active sites. Due to their polar nature, water molecules tend to reside on oxygen vacancy defects. Increasing the number of oxygen vacancies for TiO<sub>2</sub> material enhances the ionization of adsorbed water molecules, which speeds up the conduction process [32].

TiO<sub>2</sub> nanosheets with a high specific surface area and high concentration of surface oxygen vacancy defects show enhanced water dissociation, which is beneficial for proton hopping on the surface. Gong et al. reported the dominant conduction process at low RH levels could be proton hopping due to high levels of defect sites [32]. These nanostructured sensors revealed four order magnitude changes in the impedance variation from 11%–95% RH, with the short response (3 s) and recovery times (50 s) [32]. Lin et al. reported a humidity sensor based on graphene/TiO<sub>2</sub>,

which exhibited a sensing response (28 s) and humidity hysteresis value of <0.39% at 12%–90% RH [4].

The literature reports that if some of the positions initially occupied by the atoms of one of the metals are now occupied by atoms of another metal, the material's electrical response to humidity is altered. This can be related to the electronegativity of the occupying metal atoms, which can be used to regulate sensitivity [51].

Thus, doping a composite material with additional semiconducting metal oxides will induce changes in the sensor's electrical response to moisture [51]. Another effect of doping to modify the sensing properties can be stated as the ability to induce additional atomic defects. Depending on their ionic valency, they can also add charge carriers on the surface, producing a strong electric field. This favors more ionization of water molecules and hence high  $H^+$  density [51]. Accordingly, the enhanced sensitivity of doped  $TiO_2$  nanofibers towards the water molecules could be attributed to more favorable charge transfer between the adsorbed water molecules and the surface.

Musa et al. claimed that the improvement shown in sensitivity value in V-doped  $TiO_2$  nanorod arrays (TNA)-based humidity sensors is due to an increase in defect sites, particularly oxygen vacancies, usually associated with metal doping of  $TiO_2$  [52]. Zare et al. reported the doping of silver with an optimized level of 3 wt% improved humidity sensing of  $TiO_2$  significantly compared to pure  $TiO_2$  sensor [53]. Another study by Buvailo et al. showed that  $TiO_2$ -based nanomaterials doped with LiCl had revealed 0.75 and 1 s for sensor response and recovery time in the range of 5%–95% RH [54].

Angappane et al. reported nanorod  $TiO_2$  array sensor showed good sensitivity for relative humidity above 50%. This enhancement was related to the nanorod morphology of  $TiO_2$ . Also, annealing post-treatment increased the protonic conduction due to the enhancement of carrier concentration [55].

In summary, it can be concluded that  $TiO_2$  exhibits both ionic and electronic conduction mechanisms. Therefore, ionic and electronic conduction (with ions being

the dominant carriers) seems to be in charge at high RH levels, while the dominant charge carriers are electrons at low RH levels ( < 30%). Accordingly, sensing mechanisms at room temperature can be of an electronic-ionic nature, depending on where one lives. Humidity sensing behaviors are categorized into three different relative humidity regions:

- At low RH levels, electronic conduction based on electron donation from water molecules is the main sensing mechanism.
- At medium RH levels, due to the number of physisorbed layers after the creation of chemisorbed layer, both electronic and ionic conduction is responsible for humidity sensing.
- At high RH levels, with the increased number of physisorbed water layers, ionic conduction is dominant due to proton hopping between water molecules.

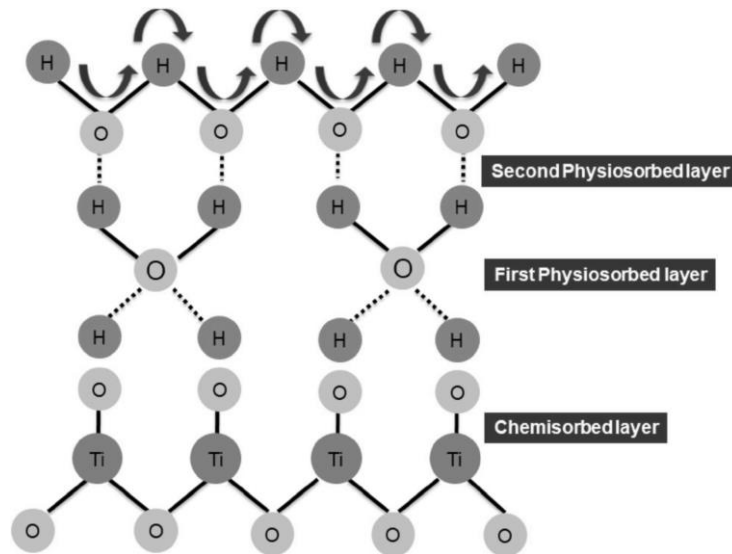


Figure 2.1. Schematic illustration of TiO<sub>2</sub> humidity sensing mechanism [56].

## 2.2 Zeolite and zeotype-based materials in water sorption and humidity

In the case of zeolites at low  $P/P_0$  levels of water, Lewis acid sites (presumably octahedrally coordinated aluminum) were proposed to be the active site for water sorption. However, at higher  $P/P_0$ , Brønsted acid sites (bridging hydroxyls) are said to have the primary role in the water sorption mechanism. Figure 2.2 shows possible orientations of the water molecules on Brønsted acid sites in ZSM-5 zeolites demonstrated by Mintova et al. [57]. Accordingly, the mechanisms proposed in Figure 2.1-a and b were claimed to be more probable.

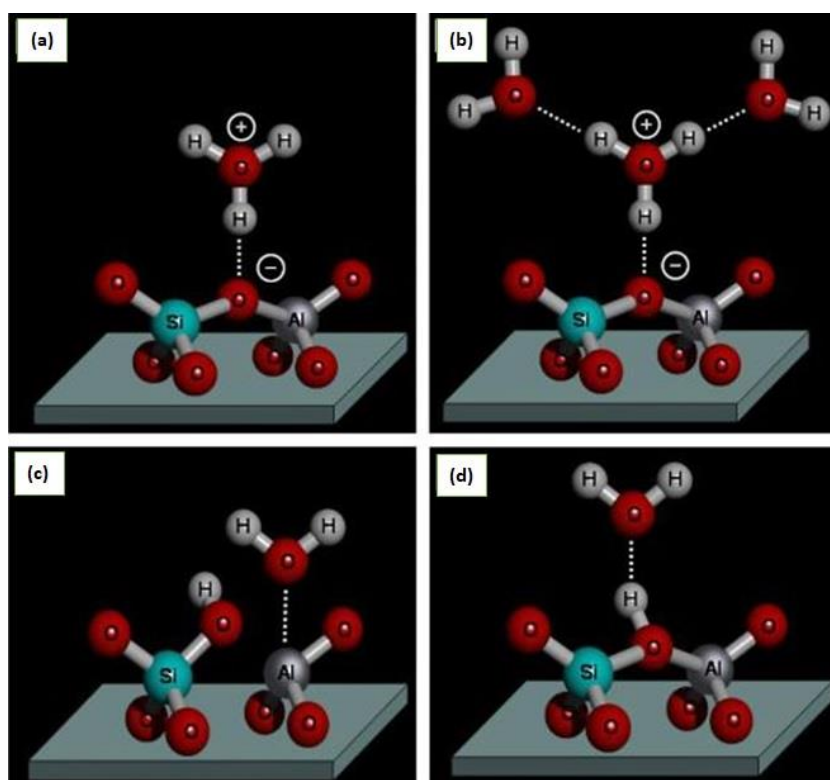


Figure 2.2. Possible sites of water molecules adsorbed on HZSM-5 zeolite [57].

A significant method to change and understand the water sorption affinity of zeolites is to investigate the effect of electronegativity of the incorporated metals (Al, Ti, Zr, etc.) into the framework positions and their concentration in the framework.



Zeolites like HZSM-5 with higher Al content have higher total water uptake due to more hydrophilic active sites, which results in enhanced water sorption at very low  $P/P_0$  values. It was shown that the water was sorbed at the acid sites of HZSM-5 through the formation of hydronium ( $H_3O^+$ ) ions rather than hydrogen bonding to the acidic proton [58],[59]. Thus, the number of Al atoms in the zeolite framework also affected the water sorption mechanisms.

It was shown that the amount and the type of defect sites in zeolites influenced the water adsorption capacity. The defect sites depend on the synthesis method, calcination, ion exchange, and the presence of doped elements. These defect sites, which are surface hydroxyl groups, interact with the water. Once the number of water molecules in the cavities is increased, water clusters are formed through hydrogen bonding.

Zeotype materials like aluminophosphate (AlPOs) and titanasilicate (TiSi) were shown to be promising materials for water sorption and humidity sensing applications. Despite the zeolites, AlPOs' framework is neutral, and no ions are present in the framework. It is anticipated that the AlPOs only have a low concentration of surface hydroxyl groups.

Generally, the hydrophilicity of zeolites originates from both extra-framework cations and framework anion sites. However, AlPOs, zeotypes, are often categorized as hydrophilic materials because they sorb water even under low  $P/P_0$  [57]. For zeolites, the water filling depends on the channel size. On the other hand, the water sorption capacity for AlPOs is related to the pore size and the angle of O-Al-O bonding in the framework, the existence of polyhedral Al sites, and the dimensions of the framework. The angle between O-Al-O could create different dipole moments and change the affinity to water sorption. The wider O-Al-O angles attract water molecules, while the narrower angles prohibit water molecules from being absorbed. Other properties come from oxygen atoms in the O-Al-O bonding, which controls the distance between water molecules sorbed on the Al sites. High hydrophilicity of AlPOs can also be related to (a) different concentrations of defect sites (Al-OH and

P-OH) in the structures, (b) the ability of tetrahedral Al framework to form polyhedral (Penta- or octahedral Al), and (c) difference in the electronegativity between Al (1.5) and P (2.1) atoms [57]. Although the AlPOs are composed of Al-O-P networks and the molar ratio Al/P is identical, this ratio is slightly varied, and as a result, the Al-OH and/or P-OH groups appear in order to retain the electrical neutrality of the structure. Unlike zeolites, the interaction of AlPOs with water is dominated by hydrogen bonding with a certain number of hydroxyls and non-polar surfaces. The abrupt water uptake is attributed to the water sorption at the moderate hydrophilic sites contributed by the structural defects, i.e., P-OH or Al-OH [57]. Kornatowski et al. reported the effect of doping on AlPOs water sorption properties [60]. By increasing metal content, a shift to lower relative pressures at the isotherm step and a transition of the water adsorption isotherm to type I was observed. The number of metal centers that control the adsorption mechanism and the structural defects and/or surface OH groups created from the metal incorporations increased the water sorption [60].

Compared to pure TiO<sub>2</sub> and SiO<sub>2</sub> compounds, the water sorption activity and capacity of Titanosilicates (TiSi) are much higher due to octahedrally coordinated Ti in the mixed oxide materials. Sosnov et al. revealed that the higher water sorption of amorphous TiSi with high TiO<sub>2</sub> concentration was related to a high amount of surface hydrolytically unstable titanosiloxanes (Si-O-Ti) [33]. This fact was explained by the high tendency of Si-O-Ti bonds to undergo hydrolysis during water sorption, thus producing Si-OH and Ti-OH, which were responsible for the subsequent sorption of water molecules. Another study showed the improvement of the water sorption capacity of TS-1 by increasing the amount of the framework titanium. However, the high titanium leads to anatase formation and decreases the final material's pore volume [34]. This information makes titanosilicate a good candidate for humidity sensing applications.

Zeolites, with their enhanced rate of water sorption, good regeneration ability, low toxicity, and long-term stability, are proposed to be very promising for humidity

sensing applications. However, studies evaluating zeolites as humidity sensors are not at a level that can be directly applied in industry. Zeolites, as humidity sensors in the literature, have been used as host materials for guests such as LiCl [61]. In thin film studies using the intrinsic properties of zeolites, humidity sensors based on the principle of change in mass have been designed. For this goal, Mintova et al. used the secondary growth method as a thin film production technique, and zeolites were grown on microbars [62], [63]. However, resistive-type humidity sensors using zeolites and zeotype materials are very few in the literature [64]–[67]. Thus, there is a lack of investigation regarding humidity sensing-related work. The biggest challenge in this field is to a) form zeolites, which can be chemically and structurally altered in many different approaches, into thin films, and b) subject these films to measurement techniques for their application area. Only then can it be possible to turn the beneficial structural properties of zeolites into an advantage in the field of humidity sensors. From this point of view, the controlled variation and determination of the structural and crystalline properties of zeotype thin films are very important.

In the present study, titanosilicate ETS-10 and vanadosilicate AM-6 have been selected to investigate their humidity sensing behavior. In contrast to  $\text{TiO}_2$ , titanosilicate ETS-10 has higher flexibility for chemical or structural modification due to its unique framework, charge distribution, and extraordinary adsorption properties [10]. The framework of ETS-10 consists of corner-sharing tetrahedrally coordinated silicon and octahedrally coordinated titanium connected by bridging oxygens [9], [10]. The pore system of ETS-10 consists of a three-dimensional 12-member ring channel, where titanium sites are located in small 7-membered ring channels [10]. Generally, compared to conventional zeolites, the interaction between water molecules inside the 12-membered ring channels of ETS-10 and the framework is relatively weak, which facilitates the regeneration of this zeotype material [68]. Owing to interesting water adsorption properties, ETS-10 was investigated for cyclic adsorption heating purposes [69].

The other fascinating property of the ETS-10 structure is its one-dimensional -Ti-O-Ti- chains surrounded by a highly insulating siliceous matrix. These chains are considered a quantum confined form of titania, i.e., titania quantum wires. The combination of these semiconductive titania quantum wires and the uniform micropore system (pore size of  $4.9 \text{ \AA} \times 7.6 \text{ \AA}$ ) [38]. This 1D quantum-confined wire acts as a semiconductor with promising potential in various applications like photocatalysis and other novel applications like humidity sensors.

### 2.3 Synthesis of titanosilicate ETS-10

Two-dimensional surface nucleation was the proposed mechanism for the growth of ETS-10 crystal [39], [42], [43]. In this growth model, ETS-10 crystals were shown to grow via a “layer-by-layer” crystal growth mechanism, where multiple surface nuclei form and propagate on the square crystal facets [43]. Adjacent layers of Ti wires in ETS-10 are orthogonal to each other and stacked layer by layer [39]. The  $\text{TiO}_3^{2-}$  wires are broken at random points in ETS-10 crystals due to defects, which are hypothesized to occur where multiple spreading surface nuclei meet to form a new layer on top of a previous layer (layer-by-layer ETS-10 crystal growth mechanism) [43]. The pore system contains 12-membered rings and displays a considerable degree of disorder due to different stacking sequences, which causes the broadening of the ETS-10 pores up to 2 nm [44], [45]. ETS-10 is very sensitive to synthesis conditions, such as the pH of the synthesis gel, water content,  $\text{Na}^+$  and  $\text{K}^+$  ions in the synthesis gel,  $\text{SiO}_2/\text{TiO}_2$  molar ratios, and temperature of crystallization [39]. The use of different titanium sources leads to the formation of ETS-10 crystals with different phase purity, particle morphology, and particle size. The crystals synthesized by  $3.4\text{Na}_2\text{O}:1.5\text{K}_2\text{O}:\text{TiO}_2:5.5\text{SiO}_2:180\text{H}_2\text{O}$  displayed bipyramidal and truncated bipyramidal morphologies upon using P25 and  $\text{TiCl}_3$  as Ti sources, respectively. Different morphologies of the crystals were explained by different nucleation rates and crystal growth as Ti sources were altered [39].

Silicate species were formed in solution and highly dispersed P25 fine particles interacted with them to create hydrous silica-titania gels under the mediation of OH<sup>-</sup> ions [8]. Ti atoms in P25 are six-coordinated and act as a structure-directing agent, leading to rapid nucleation. As a result, many small crystallites with an excellent bipyramidal morphology were obtained in the silica-titania gels via a direct structure reconstruction (Figure 2.3). In the case of TiCl<sub>3</sub>, the coordination number for Ti is different, resulting in a decreased nucleation rate and crystal growth rate, leading to smooth and larger crystals with a truncated bipyramid morphology [39].

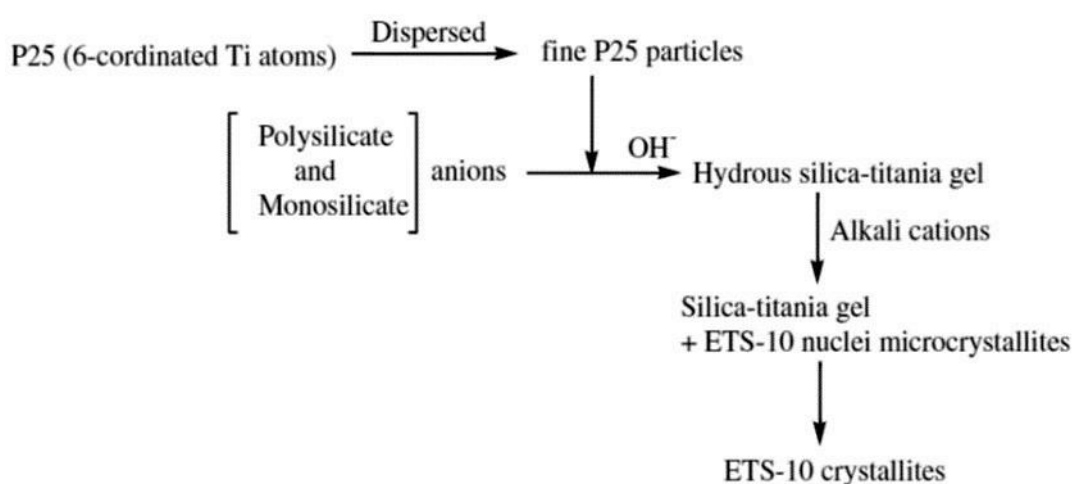


Figure 2.3. Proposed mechanisms of ETS-10 crystallization with P25 as the Ti source [39].

ETS-10 crystals with large a- and b-dimensions, which means square faces and relatively small trapezoidal faces (plate-like), would be better for the longer getting longer -Ti-O-Ti- chains. The largest ETS-10 crystals reported prepared with Ti(SO<sub>4</sub>) as Ti source by xNa<sub>2</sub>O:yK<sub>2</sub>O:TiO<sub>2</sub>:5.5SiO<sub>2</sub>:H<sub>2</sub>O (average dimensions 80\*80\*22μm) were obtained using a mixture with x/y= 0.6 and z= 300 [43].

In a defect-free ETS-10 structure, titanium ions are at the center of TiO<sub>6</sub> octahedra and are saturated by six oxygen atoms. Therefore, they cannot interact with molecules hosted in the channel system. The only titanium ions that were counted as active sites were the ones on the external surfaces or at defective sites (i.e., where -Ti-O-Ti- chains have a defect or a gap) and formed hydroxyl groups with saturated

dangling bonds of titanium ions forming Ti-OH groups [70]. Ti-OH groups could increase by different methods. The external surface area can be increased by synthesizing small crystals [41] or applying some post-synthesis, like acid treatment [71]. Another way to enhance the active sites could be the isomorphous substitution of transition metals like Cr, Fe, and V [72]–[74]. For ETS-10, Ti can be replaced entirely by V, and its isostructure AM-6 could be revealed [12]. There are studies on the properties of V-doped ETS-10 [74], [75]. Nash et al. reported the enhancement of the photocatalytic activity of V-doped ETS-10 compared to ETS-10 and AM-6 due to the presence of  $V^{4+}$  and  $V^{5+}$  states for an optimized concentration of vanadium incorporated into the ETS-10 structure. Increasing the amount of Vanadium caused a loss in structural stability and decreased photocatalytic activity. At higher V levels, the oxidation of the  $V^{4+}$  to  $V^{5+}$  in the chain drives the collapse of the ETS-10 structure, which is approved by energy calculations by Shough et al. Due to this theory, they predict that a chain of  $V^{5+}$ -O- $V^{5+}$  is energetically unfavorable [74], [75]. The appearance of both  $V^{4+}$  and  $V^{5+}$  states for V-substituted ETS-10 because long chains of  $V^{5+}$  were unstable. Their results claim that photocatalytic activity was better at a low vanadium concentration due to improved charge separation, where most of the  $V^{4+}$  and  $V^{5+}$  sites were isolated from each other. By enhancing the vanadium concentration, carrier recombination increased, which could be related to an increase in adjacent  $V^{4+}$  and  $V^{5+}$  sites. Moreover, by increasing the number of adjacent  $V^{5+}$  sites, the stability of the ETS-10 structure decreased, possibly resulting in the collapse of the structure at long  $V^{4+}$ -O- $V^{4+}$  chain lengths. However, there were no details about potential changes for Ti states by adding Vanadium to the structure [76]. The presence of vanadium also creates new surface sites at the termination of the chains or at defects along the chain that expose the vanadiol group. These peaks appeared as a result of distorted vanadium with a V=O bond as a defect site [77].

## **2.4 Films Fabrication methods for Zeolites and Zeotypes**

It is possible to use nano-sized zeolite and zeotype particles in various production methods. These methods could be classified into three classes: (i) seed methods, (ii) crystal attachment on functionalized surfaces, and (iii) direct synthesis of zeolite and zeotype crystals on support.

### **2.4.1 Thin Film Preparation of Zeolites and Zeo-type Materials: In situ and Secondary Growth Method**

The method determined to make films from zeolite and zeotype powder directly affects the performance of these films in their fields of use. In general, two different film production techniques are used in the concept of this study. These are spin coating and secondary growth methods.

The spin coating method is a method used to form homogeneously thin films on different surfaces. Usually, a small amount of coating material is applied by dripping to the center of the substrate; then, the substrate is rotated at high speed to spread the coating material by centrifugal force. By this method, the zeolite powder is homogeneously coated on the substrate.

In the secondary growth method, the crystals are grown into each other to form a stable structure, and the spaces between the crystals can be removed with this structure (Figure 2.1). In this method, seed crystals are coated on the substrate surface using a suspension of zeolite crystals. These seed-coated films were reacted with a second synthesis gel, and seed crystals act as nucleation sites for growth. Therefore secondary growth is provided from existing nuclei during secondary growth. Moreover, the direction of growth and the morphology of the resulting film can be controlled by seed orientation. On the other hand, the zeolite gel composition is very effective in directing growth. Therefore, by changing the secondary growth gel's chemical composition, the film's preferred crystallographic orientation can be varied. This method results in a continuous and stable film structure, and

intercrystalline spaces are eliminated. This way, unlike the spin coating method, uninterrupted internal channels can be created [78], [79].

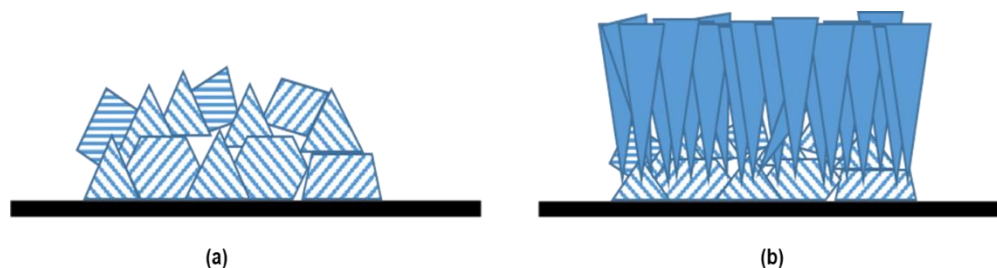


Figure 2.4. schematic of films prepared by (a) Spin coating and (b) Secondary growth technique.

#### 2.4.1.1 Controlling the Crystal Orientation in Zeolite and Zeotype Materials

To produce high quality zeolite films, microstructures of zeolite, such as crystallographic preferred orientation (CPO) or thickness, should be manipulated and optimized accurately. Device applications involving zeolite films are most likely affected by these microstructures. Among other types of microstructures, control of CPO is vital [80], [81]. Zeolite films are most likely randomly oriented, but preferred orientation is required for particular applications [82]. The out-of-plane crystallographic texture of the films highly affects their performance. Van der Drift proposed an evolutionary selection model to explain the formation of this texture in the 1960's. According to this model, grains have different crystal faces with different growth rates. Crystals with slighter growth rates disappear when they meet the boundaries of larger crystals. Crystals with growth rates in the perpendicular direction of the surface were preserved [81]. There is competition between the crystal growth rate and nucleation rate. Secondary growth mechanism should provide conditions such that the crystal growth rate overcomes the nucleation rate. Besides, crystals in the desired orientation should have the highest growth rate [83].

The secondary growth method is the most proper approach to obtain oriented zeolite film with respect to other methods due to the higher reproducibility and stability of



film. Lee et al. prepared uniformly b-oriented monolayers of silicalite crystals on glass substrates by using fingerprinting. To strengthen the bonds between the substrates and zeolite crystals a certain modification was applied to substrates or zeolite crystals. While silicalite-1 was modified Trimethylpropylammonium (TMP<sup>+</sup>) groups, glass substrates were modified with butyrate (Bu<sup>-</sup>) groups forming ionic bonding. Hydrogen bonding was formed between the surface hydroxyl groups of bare zeolite and bare glass. Another hydrogen bonding existed between the zeolite hydroxyl groups and poly(ethyleneimine) (PEI) and PEI and the hydroxyl groups of bare glass substrates. These ionic and hydrogen bonding were the most effective bonding types for monolayer formation [84].

Yilmaz et al. obtained b-oriented ETS-4 films on alfa-alumina and titania substrates by using the secondary growth method. The pore channel system and -Ti-O-Ti-chains in the structure of ETS-4 is b-oriented. Therefore, it is important to prepare b-out-of plane ETS-4 films for applications. It was demonstrated that the seed layer on alfa alumina is partially b-oriented, while the seed layer on titania substrate is partially a- and c-oriented. After hydrothermal treatment of seed layers, b-oriented ETS-4 films were obtained on both alfa-alumina and titania substrates. They claimed that secondary growth conditions are more effective than seed layer orientation for the formation of ETS-4 films [83].

Lin et al. studied the formation of ETS-10 membranes on different types of substrates for water/alcohol pervaporation experiments by using secondary growth approach. XRD patterns of pure ETS-10 powder, and ETS-10 membrane were demonstrated in Figure 2.5 [85].

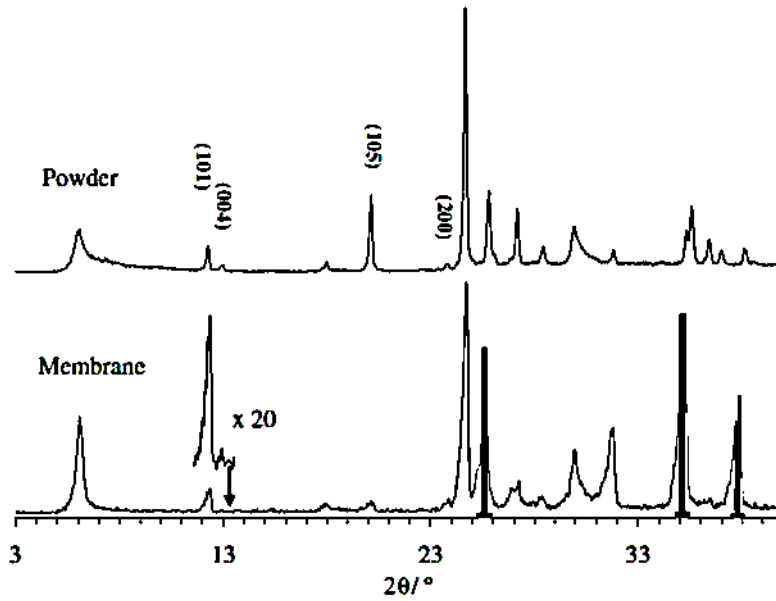


Figure 2.5. XRD patterns of ETS-10 in powder form and ETS-10 membrane [85].

Certain peaks with different intensities were obtained in the XRD pattern of ETS-10 membrane with respect to ETS-10 powder through the preferred growth direction. The (004) reflection was almost insignificant, which indicates c-orientation. CPO was calculated for quantitative analysis for orientation. Accordingly,  $CPO_{x/y} = \frac{(I_x/I_y)_m - (I_x/I_y)_p}{(I_x/I_y)_p}$  was defined where I indicate the integrated intensity corresponding to x and y peaks; m and p represent membrane and powder form, respectively. a and b orientation can be taken as equal due to the tetragonal structure of ETS-10.  $CPO_{200/105}$  was calculated as around 20 for ETS-10, indicating ETS-10 has a(b)-out-of-plane preferred orientation. The main channels of ETS-10 are parallel to a or b orientation, a(b)-out-of-plane preferred orientation can enhance membrane properties [85].

Galioglu et al. prepared oriented ETS-10 films on ITO-coated glass substrates by using secondary growth approach. They coated seed layers 1-time, 2-times, and 3-times by dip-coating method and applied hydrothermal growth to seed crystals for ETS-10 formation. It was observed that the intensities of XRD peaks of ETS-10 powder have differences with respect to ETS-10 film (Figure 2.6) [78].

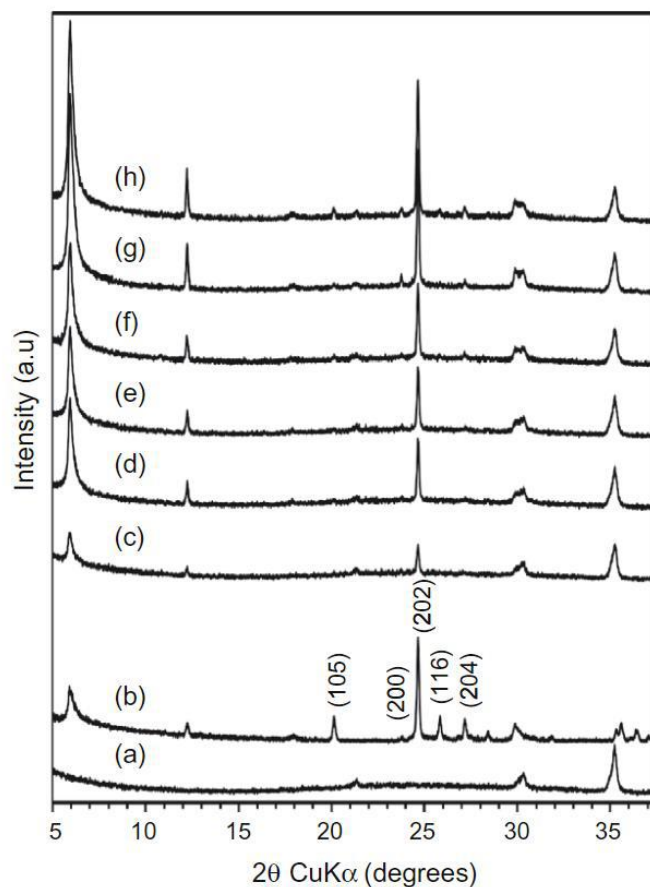


Figure 2.6. XRD patterns of bare ITO glass substrate (a), ETS-10 powder (b), seed layers deposited on the ITO glass substrate using 1 (c), 2 (d), and 3 (e) dip coating steps, and films after secondary growth of seed layers deposited via single (f), double (g), and triple (h) dip coating [78].

While the intensities of the (105), (116), and (204) peaks decreased, the intensity of the (200) peak increased, indicating a(b)-out-of-plane orientation. CPO was also calculated for quantitative analysis of the degree of the a(b)-out-of-plane orientation. Accordingly,  $CPO_{200/105} = \frac{(I_{200}/I_{105})_f - (I_{200}/I_{105})_p}{(I_{200}/I_{105})_p}$  was defined. It was observed that CPO values decreased with the increasing number of dip-coating steps, which is consistent with the literature [78].

CPO was calculated based on (200) and (105) reflections to determine the degree of a(b)-out-of-plane preferred orientation since ETS-10 has a tetragonal structure where

a and b are equivalent. The intensity of the (105) plane is used for the calculation of CPO instead of the (004) plane due to its very low intensity, as shown in Figure 2.6.

Accordingly, (105) plane was determined as the plane making the lowest angle with (004). Thus, CPO is calculated based on (200) and (105) reflections and defined as  $CPO_{200/105} = ((I_{200}/I_{105})_f - (I_{200}/I_{105})_p) / (I_{200}/I_{105})_p$ , where I depict the intensity of the particular planes and f, and p represents film and powder, respectively.

#### **2.4.1.2 Effect of the Seed Crystal Population on Film Formation**

The seed layer added to the synthesis mixture gives smaller zeolite crystals, facilitates zeolite growth, and increases crystallization. Thin zeolite films and membranes were prepared by coating the pre-seeded substrates with zeolite nanocrystals. Afterward, hydrothermal treatment was applied to the seeded substrates. In this way, perfect control of zeolite film orientation, morphology, and crystal growth was obtained. It is known that the seed crystals' type, size, shape, and orientation affect zeolite film growth [86]. Smaller seeds cause better-intergrown zeolite membranes to be obtained.

Crystal size and morphology affect the seed layer formation and, consequently, zeolite membrane. The seed layer becomes dense and homogenous with decreasing seed crystal size. Large or hexagonal-shaped seed crystals may cause a loose seed layer. It can be inferred that the quality of the seed layer is dependent on the size and morphology of seed crystals. Intergrowth of zeolite membranes grown from smaller seed crystals is better and smooth surfaces can be most likely obtained. Some defects and impurities emerge during membranes' formation using smaller seed crystals [87]. Li et al. investigated the seed layer concentration on the formation of silicalite-1 membranes. A loose structure of the zeolite membrane was obtained at a low concentration rate. With the increasing level of seed concentration, a denser seed layer and, consequently, a thicker and more uniform zeolite membrane was obtained. Further increase of the seed concentration caused seed layer crystals to overlap with

each other resulting in the formation of cracks on the zeolite membrane. They proposed that seed concentration affects the quality of the seed layer in parallel with the quality of the zeolite membrane [88].

The performance of a zeolite film is affected by the orientation of the crystal constituting the zeolite film due to the fact that the pore system alters with the orientation of the crystals. Therefore, it is necessary to control the orientation of the crystal constituting the zeolite. Hedlund et al. succeeded in growing silicalite-1 films using silicalite-1 seed crystals with three different dimensions. Seed crystals were coated on a silicon wafer to form half-monolayer, monolayer or bilayer. Subsequently, hydrothermal treatment was applied to the seeded substrates. Thicker films were obtained as a result of the utilization of large seeds. When seed crystals with the same dimensions were used, monolayer or half-monolayer coating of the seed layer could not change the thickness of the zeolite film. However, thicker films were obtained by using bilayer seed coating. The crystals constituting the zeolite films did not have characteristic silicalite-1 morphology because crystal size was almost the same as the film thickness, decreasing the possibility of lateral growth. The number of zeolite crystals per unit area decreased with increasing film thickness, which was most probably observed when the largest seed crystals were used. A continuous zeolite film could not be obtained when a half-monolayer seed layer was used. Besides, the growth of seed crystals was in every dimension, and the characteristic morphology of seed crystals was no longer observed. In this study, it was identified that the control of the amount and the orientation of seed crystals could provide control over the crystal constituting the zeolite film [89].

Wong et al. indicated that seed concentration and the chemistry of synthesis and crystallization conditions were significant for the morphology and orientation of the crystals constituting zeolite films. That way, they synthesized TPA-silicalite-1 crystals as seeds crystals and coated them on Si wafers such that each Si wafer had a different concentration of seed crystals. Then, hydrothermal treatment was applied to seeded substrates. Crystal grains generally grow towards synthesis solution. According to the competitive growth model, the competition between the neighboring grains determines the growth of each grain. The morphology and the orientation of the ultimate zeolite film is determined accordingly. More growth centers are formed with an increasing amount

of seed, causing greater competition for nutrient and space, affecting zeolite growth strongly. It was observed that crystal intergrowth was increased but crystal size was decreased due to competition. A change in the crystal morphology was also observed with an increasing amount of seed crystals [90].

Xomeritakis et al. produced polycrystalline MFI films on porous alfa-alumina and non-porous glass substrates using secondary growth and in-situ approach. Microcrystalline MFI crystals were coated on the alfa-alumina substrates, and hydrothermal treatment was applied to the seeded substrates in secondary growth method. A comparison between the films produced with or without seed layer was carried out for structural formation and permeability properties for butane isomers. The obtained films under secondary growth conditions revealed columnar grain structure and low surface roughness. The presence of the seed layer strongly affected the film structure under secondary growth conditions. Crystals grew in solution and on the substrate surface in the absence of the seed layer. Characteristic imperfections arising from the gaps in the seed layer were obtained in the films obtained by using secondary growth method. Intergrown polycrystalline MFI films could not be observed in the absence of a seed layer, as seen in the secondary growth method. The orientation of the MFI crystals constituting the film was different for secondary growth and in situ methods. In the presence of the seed layer, seed particles began to grow as soon as they were in contact with the secondary growth solution skipping the nucleation step. The nutrient and precursor contributed to crystal growth without forming new grains. The seed layer was shown to provide crystal growth without the need for nucleation, restricting the formation of new crystals. The quality of the films was dependent on the seed layer. The permeability performance of the film was highly affected by the orientation of the crystals constituting the film [91].

## **2.5 Goal and Objectives**

The main goal of this study is to investigate the humidity sensing performance and to identify the sensing mechanism of microporous titanosilicate ETS-10 and vanadosilicate AM-6 zeotype materials with Ti-O-Ti and V-O-V quantum wires,

respectively, and introduce them as brand-new humidity sensors for various applications. The objectives to achieve this goal can be summarized as follows:

- To synthesize pure microporous titanasilicate ETS-10 and vanadosilicate AM-6 crystals,
- To prepare films from ETS-10 and AM-6 powders by spin coating method on the quartz substrate with different thicknesses and investigate the humidity sensing performance of these two zeotype using impedance spectroscopy technique,
- To prepare ETS-10 films by secondary growth method from ETS-10 coated (as seed layer) substrate, which is prepared by spin coating and dip coating with different thicknesses to understand the effect of CPO and seed crystal population and coating technique on humidity sensing behavior and performance of ETS-10 films,
- To prepare AM-6 films with two different Vanadium precursors by secondary growth method from ETS-10 coated (as seed layer) substrate, which is prepared by spin coating method to investigate the quality of V-O-V quantum wires on humidity sensing behavior and performance of these films,
- To prepare V-substituted ETS-10 films by the spin coating method to reveal the effect of the appearance of new states and defects on humidity sensing behavior and performance of these films.





## CHAPTER 3

### EXPERIMENTAL PROCEDURE

In this thesis, the AM-6 and ETS-10 crystal powders required for all the humidity sensor setups were synthesized based on the previous work established in our laboratory [92], [93]. These crystals were used for two purposes: 1) to produce films through the spin coating procedure; and 2) as seed crystals for the secondary growth coating procedure, based on the information derived from spin coating and dip coating techniques. The quality of the crystal powders and thin films prepared in this manner were measured via various equipment. All the protocols necessary for ETS-10 and AM-6 films to be used in the humidity sensor application were designed for the purpose of the current study, and the details for this setup were provided in Section 3.3. Additionally, the variations of impedance values at different frequencies were measured for all the films under different relative humidity levels employing the impedance analysis method.

#### 3.1 The synthesis of ETS-10 and AM-6 crystals

In this section, ETS-10 and AM-6 crystals were synthesized, and the synthesis conditions of these crystals, such as chemical formulations, were successfully verified [39], [50]. The synthesized samples were characterized by SEM, XRD, BET surface analysis, and advanced analysis methods such as Raman and XPS.

Table 3.1 demonstrates the synthesis conditions of powder ETS-10 and AM-6 crystals synthesized during the thesis.

Table 3.1. List of the synthesized ETS-10 and AM-6 crystals and their synthesis conditions.

<b>Crystal type</b>	<b>Molar Composition</b> <i>Reaction temperature and time</i>	<b>Ref.</b>
ETS-10	3.4Na <sub>2</sub> O:1.5K <sub>2</sub> O:TiO <sub>2</sub> :5.5SiO <sub>2</sub> :180H <sub>2</sub> O <i>230°C and three days</i>	[39]
AM-6	1.44Na <sub>2</sub> O:0.19K <sub>2</sub> O:2.2SiO <sub>2</sub> :0.11V <sub>2</sub> O <sub>5</sub> :35H <sub>2</sub> O:0.34F <i>230°C and seven days</i>	[50]

### 3.1.1 The synthesis of nano-size ETS-10 crystals

The ETS-10 nano-size powder crystals (Table 3.1) were synthesized by the gel formulation route as specified in the literature [39]. The prepared powder sample was coated over various substrates via the spin coating method. For the synthesis of these crystals, firstly, NaCl and KCl salts were dissolved in distilled water in an HDPE bottle to obtain a homogeneous solution. Afterward, sodium silicate was added to this solution and was mixed for another 4 minutes in the vortex. In order to prepare the titanium precursor solution, P25 was used as a titanium source. It was dissolved in a solution of deionized water and sulphuric acid by vigorous handshaking for 5 minutes in a separate bottle. The titanium source solution was added to the previously obtained NaCl and KCl salt solution and mixed for another 8 minutes until a homogeneous mixture was achieved. The pH of the final solution was 10.4, which was then transferred to 10 mL Teflon-lined stainless steel autoclaves and was reacted at 503 K for three days. The products were cooled to room temperature. Then the obtained product was extracted by centrifugation and washed with deionized water. The final product was dried overnight at ~343 K in the laboratory oven.

### **3.1.2 The synthesis of nano-size AM-6 crystals**

AM-6 nano-size powder crystals were synthesized by the gel formula illustrated in Table 3.1 [50]. In order to obtain AM-6 crystals, a gel with almost 10.2 pH must be prepared. First, a combination of distilled water and sodium silicate ( $\text{Na}_2\text{SiO}_3$ , Sigma-Aldrich) in a bottle was mixed using a magnetic stirrer for 1 hour. Then, a mixture of sodium chloride (NaCl), sodium hydroxide (NaOH), potassium chloride (KCl), sodium fluoride (NaF), and distilled water was mixed in a separate bottle using a magnetic stirrer for 20 minutes. As a result, the silica source was obtained. At the final stage, this solution was added to the sodium silicate and water mixture, and a homogeneous compound was achieved by rotating it for 30 minutes inside a magnetic mixer. To prepare the vanadium source, vanadyl sulfate ( $\text{VO}\text{SO}_4$ , Acros) and distilled water were mixed in a tertiary bottle using a magnetic stirrer. The result was added to the previously obtained homogeneous mixture and left to age for two days. The final gel was transferred to 10 mL Teflon-lined stainless steel autoclaves. Lastly, the hydrothermal growth of nano-sized AM-6 crystals was facilitated by leaving the steel autoclaves in a closed oven at 503 K for seven days. The products were cooled to room temperature, centrifuged, washed with deionized water, and dried overnight at  $\sim 343$  K.

### **3.2 Thin Film Preparation**

In order to acquire and investigate the benefits of zeolite and zeotype materials in humidity sensing applications, thin film-based sensors were designed from these materials. Evaluating the advantages mentioned for zeolite and zeotype materials in a real application area and transforming alleged benefits into meaningful data can only be possible by obtaining quality thin films from these materials. Accordingly, within the scope of the present study, the thin film production techniques applicable to ETS-10 and AM-6 from the literature were explored for humidity sensor applications.

### 3.2.1 Production of ETS-10 and AM-6 thin films with various thicknesses over a glass substrate via the spin coating method

Tables 3.2 and 3.3 summarize all the films produced in this study. Zeotype ETS-10 crystals (ETS-10; Table 3.1) and AM-6 crystals (AM-6; Table 3.1) were coated over glass/porcelain substrates by the spin/dip coating method.

Table 3.2. The experimental parameters of the films were obtained using the spin/dip coating method.

Sample code	Crystal type	Molar composition	Production method
ETS-10-2S ETS-10-4S ETS-10-8S	ETS-10	$3.4\text{Na}_2\text{O}:1.5\text{K}_2\text{O}:\text{TiO}_2:5.5\text{SiO}_2:180\text{H}_2\text{O}$	Spin coated: 2-4-8 times
AM-6-2S	AM-6	$1.44\text{Na}_2\text{O}:0.19\text{K}_2\text{O}:2.2\text{SiO}_2:0.11\text{V}_2\text{O}_5:35\text{H}_2\text{O}:0.34\text{F}$	Spin coated: 2 times
ETS-10-1D* ETS-10-2D*	ETS-10	$3.4\text{Na}_2\text{O}:1.5\text{K}_2\text{O}:\text{TiO}_2:5.5\text{SiO}_2:180\text{H}_2\text{O}$	Dip coated: 1-2 times

\*These samples were used only for secondary growth experiments.

For spin-coating, an ETS-10 or AM-6 suspension, prepared in ethanol at a rate of 7 wt.%, was applied to the substrate surfaces, and the substrate was rotated at 5000 rpm for 30 seconds in each step. Before the coating, the substrates (10 mm × 20 mm) went through a cleaning procedure with acetone, ethanol, and 2-propanol through an ultrasonic device for 15 minutes each. Subsequently, they were left to dry for 20 minutes in an oven at 80°C. In order to evaluate the effect of film thickness, the substrate was spin-coated 2, 4, and 8 times using the suspension of 7% ETS-10 in ethanol suspension. For dip-coating, the substrate surfaces were immersed once or twice in a suspension of these seed crystals in ethanol, and the resulting seed-coated substrates were used in the secondary growth method to obtain ETS-10 films. ETS-

10 films obtained from the seed layer by 1 and 2 times dip coating were coded as 1D-TS and 2D-TS, respectively.

### 3.2.2 Production of ETS-10 films over various substrates via secondary growth method

In the second part of this study, the secondary growth method was employed for seed-coated films. Within the scope of humidity sensor design, various alkali-free glasses were explored as alternative substrates to ITO-coated glasses formerly used in the literature [78], [94]. Substrates with insulating properties were desirable since they neutralize the effect of ionic or electronic conduction on humidity sensors.

Table 3.3. The experimental parameters of the films were prepared using ETS-10 as a seed layer with different thicknesses for the secondary growth method.

Sample code	Seed type	Film type	The molar composition of the second growth solution	Ref.
2S-TS	ETS-10	ETS-10	4.55Na <sub>2</sub> O:TiO <sub>2</sub> :5.5SiO <sub>2</sub> :1.5KF:300H <sub>2</sub> O	[43]
1D-TS	ETS-10	ETS-10	4.55Na <sub>2</sub> O:TiO <sub>2</sub> :5.5SiO <sub>2</sub> :1.5KF:300H <sub>2</sub> O	[43]
2D-TS	ETS-10	ETS-10	4.55Na <sub>2</sub> O:TiO <sub>2</sub> :5.5SiO <sub>2</sub> :1.5KF:300H <sub>2</sub> O	[43]
2S-VS <sub>1</sub>	ETS-10	AM-6	6.07SiO <sub>2</sub> :V <sub>2</sub> O <sub>5</sub> :3.37H <sub>2</sub> SO <sub>4</sub> :3.03Na <sub>2</sub> O: 3.09K <sub>2</sub> O:7.22EtOH:415H <sub>2</sub> O	[95]
2S-VS <sub>2</sub>	ETS-10	AM-6	Na <sub>2</sub> O:0.23K <sub>2</sub> O:0.97SiO <sub>2</sub> :0.1V <sub>2</sub> O <sub>5</sub> :30H <sub>2</sub> O	[12]

The secondary growth is a two-step film production technique. This method is schematically illustrated in Figure 3.1. For the coating process, the samples listed in Table 3.2 were used as seed crystals. The seed crystals chosen in this part of the study were ETS-10-2S and ETS-10-1D/2D (Table 3.3). Seed crystals in powder form were coated over various substrates (window glass, microscope glass, borosilicate glass, alkali-free glass, and porcelain) using the spin coating technique. A suspension with 7 wt.% of ETS-10 crystals in ethanol was prepared for this coating process. This

suspension was dripped over the substrates and coated with a spin coater at 5000 revolutions for 30 seconds. It was observed that the ETS-10 crystals subjected to the spin coating process were homogeneously coated on the surface. The films coated with seed powder crystals (ETS-10-2S, ETS-10-1D, ETS-10-2D; Table 3.2) were heat-treated for 9 hours at 450°C. The molar composition formulation employed in the secondary growth method differs from the formulation for seed crystal production. In the secondary growth gel preparation, a gel was prepared with sodium silicate, sodium hydroxide, titanium sulfate, potassium fluoride, and sulfuric acid. The resulting gel was used in the hydrothermal growth of seed crystals. The gel was created by the formula  $4.55 \text{ Na}_2\text{O} : \text{TiO}_2 : 5.5 \text{ SiO}_2 : 1.5 \text{ KF} : 300 \text{ H}_2\text{O}$ , developed by Ji et al. [43]. The hydrothermal synthesis was accomplished by putting the seeded substrate surfaces in secondary growth solutions for 6 hours at 503 K to produce ETS-10 films. The films synthesized in this were washed 3 times with deionized water and dried. ETS-10 films prepared by this method are coded as 2S-TS, 1D-TS, and 2D-TS, as mentioned in Table 3.3.

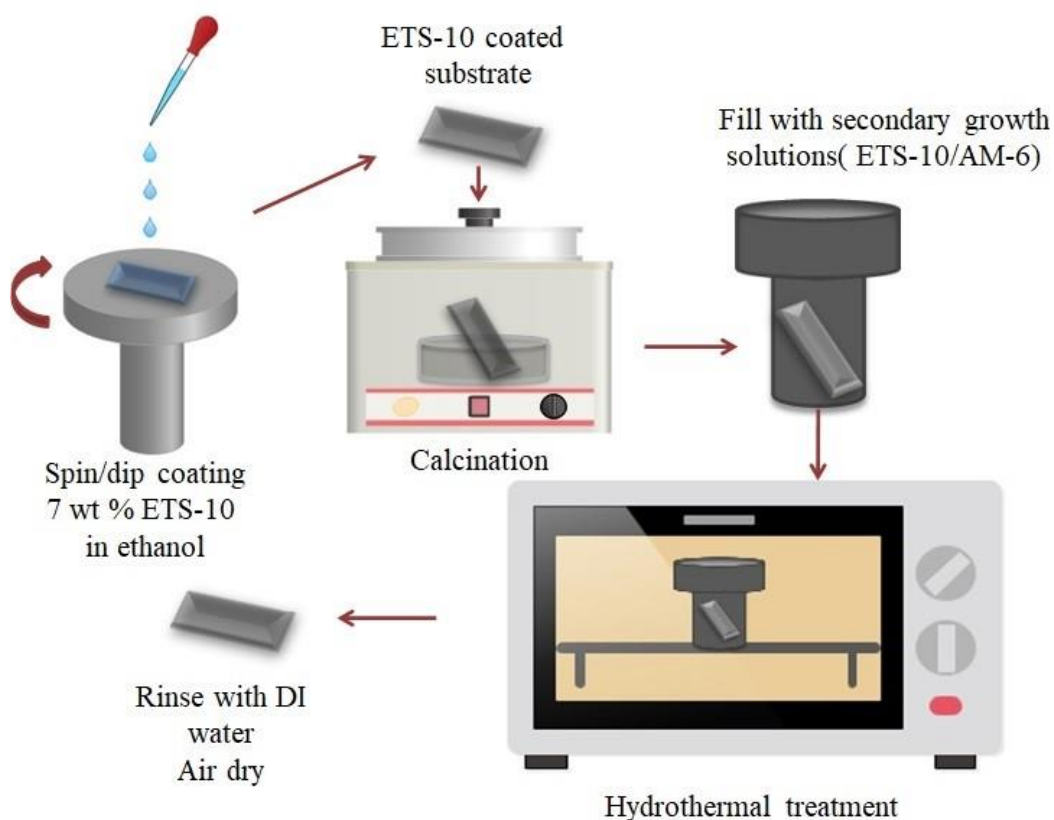


Figure 3.1. The schematic illustration of ETS-10 film production process using the second growth method [92].

### 3.2.3 Production of AM-6 films over various substrates through the second growth method, using different vanadium sources ( $\text{VO}_2$ and $\text{V}_2\text{O}_5$ )

For the preparation of AM-6 films, the secondary growth method was used to produce AM-6 films using ETS-10-coated substrates. In this respect, previously developed procedures were adapted on insulating substrates for the first time [78], [94]. In this study, porcelain surfaces were also investigated to obtain AM-6 thin films.

As explained earlier, ETS-10 seed powder crystals, using the spin-coating method, were coated on various porcelain substrates (2S-VS<sub>1</sub>, 2S-VS<sub>2</sub>; Table 3.3). For this

coating procedure, ETS-10 crystals, performing the role of seed crystals, were prepared in ethanol in the form of a 7 wt.% suspension. This suspension was coated over the substrates via dropping this solution, with a spin coating device rotating at 5000 cycles for 30 seconds. It was observed that the ETS-10 crystals were homogeneously coated on the surface using the spin coating technique. As a result of this procedure, substrate surfaces coated with seed powder crystals were produced. Afterward, these substrates underwent hydrothermal growth under certain conditions in order to synthesize AM-6 films.

Vanadium pentoxide ( $V_2O_5$ ) and Vanadyl sulfate ( $VOSO_4$ ) are the two different vanadium sources for preparing secondary growth solutions. Following the procedures defined in the literature, the secondary growth solutions were prepared from two different sources to obtain films of AM-6 structures comprising vanadium as an alternative to titanium-containing ETS-10 films [95], [12]. In all cases, seed crystal-coated substrates were placed in autoclaves filled with the pre-assigned secondary growth solutions (see Fig. 3.1). The reaction temperatures for secondary growth gels using  $VOSO_4$  and  $V_2O_5$  as vanadium sources were 230 and 255 °C respectively.

The preparation route of Vanadosilicate AM-6 using  $V_2O_5$  as the vanadium source (2S-VS<sub>1</sub>) include sodium silicate ( $Na_2SiO_3$ ), potassium hydroxide (KOH), vanadium pentoxide ( $V_2O_5$ ), ethanol (EtOH), and sulfuric acid ( $H_2SO_4$ ). The chemical formula used for Vanadosilicate AM-6 was 6.07  $SiO_2$ : $V_2O_5$ :3.37  $H_2SO_4$ :3.03  $Na_2O$ :3.09  $K_2O$ :7.22 EtOH:415  $H_2O$  [95].

The vanadium source solution was prepared by dissolving  $V_2O_5$  (Acros), ethanol, sulfuric acid, and distilled water inside the reflux system. The obtained mixture was stirred in an oil bath under argon gas at 100°C for 50 minutes. The silica source solution was prepared from stirring distilled water and  $Na_2O(SiO_2)_x \cdot xH_2O$  (Sigma-Aldrich). The obtained silica source was added to the vanadium source solution in the form of droplets when it cooled down to room temperature. After 18 hours of aging, the gel thus prepared was ready for use in the hydrothermal growth of seed crystals. AM-6 films were finally obtained after 5 hours of hydrothermal growth at



528 K by spreading the prepared gel over the seed-coated substrates in the autoclaves.

Vanadosilicate AM-6 was also synthesized using  $\text{VOSO}_4$  (Sigma-Aldrich) as the vanadium source. The chemical formula used for Vanadosilicate AM-6 was  $\text{Na}_2\text{O}:0.23 \text{ K}_2\text{O}:0.97 \text{ SiO}_2:0.1 \text{ V}_2\text{O}_5:30 \text{ H}_2\text{O}$  [12]. The preparation route of Vanadosilicate AM-6 using  $\text{VOSO}_4$  as the vanadium source (2S-VS<sub>2</sub>) solution, first of all, a combination of sodium chloride (NaCl), sodium hydroxide (NaOH), potassium chloride (KCl), sodium silicate ( $\text{Na}_2\text{SiO}_3$ , Sigma-Aldrich), and distilled water was mixed for 1 hour in a magnetic stirrer. Subsequently, vanadium sulfate ( $\text{VOSO}_4$ ) and distilled water were mixed using the magnetic stirrer to prepare the vanadium source in another bottle. In the final step, the vanadium solution was added to the sodium silicate, salt, and water mixture until a homogeneous compound was obtained for 30 minutes inside the magnetic stirrer. The mixture was transferred into seed-coated substrates placed in 10 ml Teflon containers in stainless-steel autoclaves. After that, the hydrothermal growth of AM-6 films was carried out by leaving the stainless steel autoclaves sealed for 3 days in an oven at 503 K. The films thus synthesized were then washed 3 times with deionized water and dried.

### 3.2.4 Synthesis of Vanadium-substituted ETS-10 Crystals

For vanadium-substituted ETS-10 samples, three different concentrations of vanadium-added titanium-containing solutions were prepared by adding 0.25, 0.75, and 1.25g of  $\text{VOSO}_4 \cdot x\text{H}_2\text{O}$  (Sigma-Aldrich) as vanadium source to the parent gel of ETS-10 with the formulation of  $3.4 \text{ Na}_2\text{O}:1.5 \text{ K}_2\text{O}:\text{TiO}_2:5.5 \text{ SiO}_2:180 \text{ H}_2\text{O}$  [39] mentioned at (Table 3.1). The vanadium-added titanium source was prepared by adding  $\text{VOSO}_4$  to the bottle containing P25 (76wt% anatase and 24wt% rutile, Degussa),  $\text{H}_2\text{SO}_4$ , and  $\text{H}_2\text{O}$ . The silica source was prepared by mixing sodium silicate (27 wt. %  $\text{SiO}_2$ , 8 wt. %  $\text{Na}_2\text{O}$ , and 65 wt. %  $\text{H}_2\text{O}$ , Aldrich), NaCl, KCl, and  $\text{H}_2\text{O}$ . After mixing the two solutions, the  $\text{V}_x\text{ETS-10}$  samples were hydrothermally synthesized in the autoclaves at 503 K for 3 days. Samples with  $\text{V}/(\text{V}+\text{Ti})$  molar

ratios of 0.1, 0.2, and 0.31 were denoted as  $V_{0.1}$ ETS-10,  $V_{0.2}$ ETS-10, and  $V_{0.3}$ ETS-10, respectively. The prepared ETS-10 and  $V_x$ ETS-10 (x indicates the atomic weight ratio of vanadium in the structure of ETS-10) powders were mixed with (%7 wt) ethanol, and these prepared suspensions spin-coated two times on a quartz glass substrate with gold interdigitated electrodes.

### 3.3 Humidity Sensor Experimental Setup

A homemade experimental setup was designed to investigate the humidity behavior measurements of the prepared films. For this purpose, firstly, silicone masks with inter-finger spacing of about 500  $\mu\text{m}$  were placed on the surface of glass/porcelain substrate with (10 mm  $\times$  25 mm) dimensions to obtain interdigitated electrodes on the films. Then, to get gold-interdigitated electrodes on the substrate or the film, masks were coated with gold under argon gas using the plasma spraying method. In the spin coating method, ETS-10 or AM-6 (ETS-10 (2S-4S-8S), AM-6-2S films) seed powder crystals were coated over the electrodes by this method. A schematic representation of the various stages of this process is given in Figure 3.2.

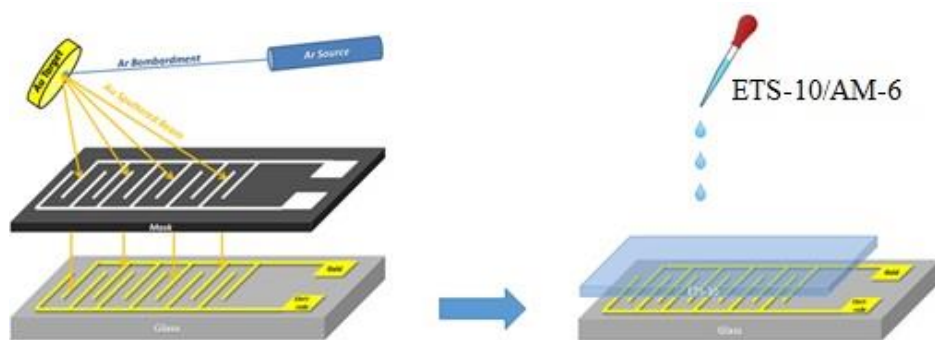


Figure 3.2. A schematic illustration of the process of obtaining humidity sensors from ETS-10 or AM-6 thin films over substrates using the spin-coating method.

In order to obtain a humidity sensor from ETS-10 or AM-6 films produced using the secondary growth method, the hydrothermal growth of ETS-10 seed crystals coded as 2S/1D/2D-TS, 2S-VS<sub>1</sub> and 2S-VS<sub>2</sub> was facilitated via different vanadium or

titanium containing gel formulations. Afterward, the electrodes were coated on secondary growth films using the method described in section 3.3. The difference between the two electrode coating procedures discussed here is schematically depicted in Figure 3.3.

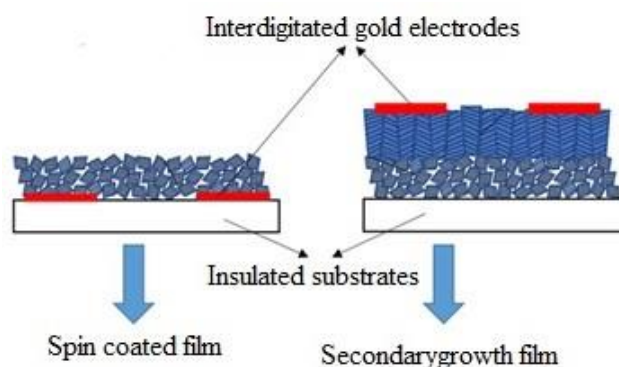


Figure 3.3. A schematic illustration for obtaining humidity sensors from ETS-10 or AM-6 films created using spin-coating and second-growth methods.

A relative humidity experimental design was fabricated for the electrode-coated films to investigate the humidity behavior of all successfully prepared sensors, as shown in Figure 3.4.

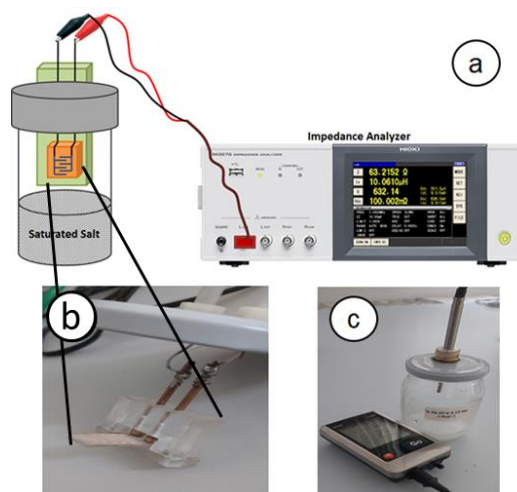


Figure 3.4. The schematic illustration of the humidity sensing experimental design (a), the film-impedance system (b), and the calibration setup with Testo 176H1 humidity sensor (c).

As indicated in Fig. 3.4-a, the lids of the glass jars had been modified. The lid configuration of the obtained device is represented in Figure 3.4-b. The desired conductivity level for the system was reached via the establishment of this mechanism. The measurement sample can be attached to two separately insulated copper wires located on top of the glass containers. This mechanism allows the conductivity values formed on the film surface to be read via an impedance analysis measuring device. The whole measurements were performed at carefully controlled humidity levels by isolating the system and measuring the humidity using Testo 176H1 humidity sensor.

The constant-humidity environment required for impedance measurements was built with the aid of saturated salt solutions placed in a closed glass container of approximately 250 cm<sup>3</sup> volume. The constant-humidity environments were controlled by the Testo 176H1 industrial humidity sensor, as illustrated in Figure 3.4-c. Humidity sensor measurements demonstrated that the relative humidity in the indoor environment reaches equilibrium in approximately half an hour. Following the completion of the measurement in the initial constant humidity environment, the films produced were transferred in one-hour intervals to other jars with constant humidity environments. The laboratory temperature for the measurements was maintained at 25°C at all times. The temperature variation in the room remained below ±1°C throughout the day. Eleven saturated salt solutions including NaOH, LiCl, CH<sub>3</sub>CO<sub>2</sub>K, MgCl<sub>2</sub>, K<sub>2</sub>CO<sub>3</sub>, Mg<sub>2</sub>NO<sub>3</sub>, KI, NaCl, KCl, K<sub>2</sub>NO<sub>3</sub>, K<sub>2</sub>SO<sub>4</sub> with 8.24%, 11.32%, 23.27%, 32.78%, 43.16%, 52.89%, 67.32%, 75.29%, 84.34%, 93.58%, 97.36% relative humidity levels were used for humidity response measurements. Figure 3.5 demonstrates an overview of the prepared setup.

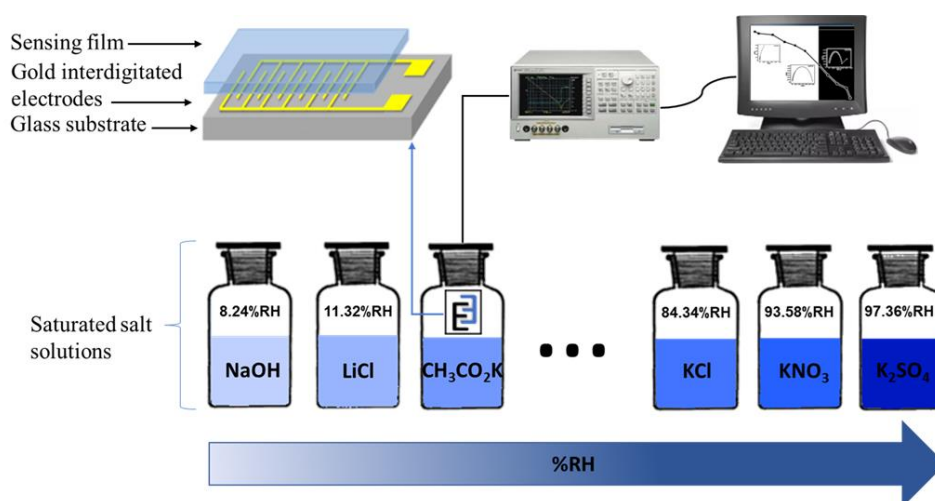


Figure 3.5. Schematic of humidity sensing setup.

The determination of such humidity sensor parameters as sensor sensitivity and response time in constant humidity environments using saturated salt solutions was carried out via the impedance analyzer (Agilent 4294A) located at the METU-Central Laboratory (ODTÜ-MERLAB). The humidity sensors' sensitivity to variations in relative humidity values was determined according to the impedance data measured at certain frequencies (100 Hz, 1 kHz, 10 kHz, and 100 kHz).

According to the impedance measurements performed on the bare sensor, it was assured that the system possessed a very high degree of resistance ( $\sim 10^9 \Omega$ ). The impedance value was measured at 100 Hz and 500 mV. The measured impedance value defined the open circuit resistance of the designed system. The rather large difference in impedance values between the measurements on the bare sensor and those after film production demonstrated that the measuring system was insulating and that the conductivity values registered by the device stemmed from the water ratio in the pores of the ETS-10 or AM-6 crystals constituting the zeotype films.

### **3.4 Analytical Techniques**

The ETS-10 and AM-6 films produced in this thesis were analyzed by advanced characterization techniques such as scanning electron microscopy (SEM), X-ray diffraction pattern (XRD), Raman analysis, Brunauer-Emmett-Teller (BET) analysis and impedance analysis. All these analyses were performed at the METU Central Laboratory.

#### **3.4.1 Scanning electron microscope (SEM)**

The SEM analyses performed in the course of this project employed Hitachi brand, S-4700 model FE-SEM (10 kV, 10  $\mu$ A), operating in the secondary electron imaging mode. The cross-sectional imaging of the broken films was accomplished by analyzing the broken surfaces.

#### **3.4.2 Raman spectroscopy**

The Raman spectroscopy of the films was carried out via a Renishaw brand Raman analyzer. A laser with a wavelength of 532 nm was used for this method of analysis and the power was supplied within the range of 0.5-1 mW.

#### **3.4.3 X-ray diffraction analysis (XRD)**

The X-ray diffraction pattern (XRD) analysis of the films was performed by means of the Rigaku-Ultima IV XRD device, which consists of a thin film add-on. The diffraction pattern was achieved through defining the scanning range as 5-40° and the scanning speed as 1°/min. A quantitative analysis of the orientations of the crystals was carried out by means of comparing the (105) and (200) peak intensities of the films and powder samples in their XRD patterns. 1°/8 min was adopted as the scanning rate for the XRD diffraction pattern of these peaks so as to pinpoint the

orientations. In this manner, the crystallographic preferred orientation (CPO) was calculated in accordance with the XRD patterns, and thereby the crystal orientations of the films were computed quantitatively. The CPO value calculated using the (200) and (105) peaks was determined according to the formula  $CPO_{200/105} = \frac{(I_{200}/I_{105})_f - (I_{200}/I_{105})_p}{(I_{200}/I_{105})_p}$ . The CPO value derived from this formula expresses the quantitative analysis of the growth of the crystals forming the films in the a(b) direction. The I value, as it appears in the formula, stands for the intensity of the corresponding peak, and the expressions f and p, respectively, refer to the samples in film and powder form. The assumption here was that the orientation of the powders was random, while the orientation of the films took place in a particular direction [82]. Furthermore, the crystallinity values and peak intensities employed in CPO calculations were determined with the aid of the Rigaku-Ultima IV XRD software.

#### **3.4.4 Brunauer-Emmett-Teller (BET)**

The BET analysis was performed using the surface characterization device at the METU Central laboratory. This device enabled us to carry out physical adsorption-desorption tests on the sample, and such features as total pore area, micropore area, pore volume, and pore size were thereby ascertained. Autosorb 6 series (Quantachrome Instruments) was used to perform nitrogen adsorption/desorption experiments. The Multipoint BET method was employed as a means of calculating the surface area of the samples, while the outer surface area was determined using the t-plot method. Samples were maintained in a vacuum for 24 hours prior to the analysis.

#### **3.4.5 X-ray photoelectron spectroscopy (XPS)**

A PHI 5000 VersaProbe spectrometer with an Al-K $\alpha$  radiation source was employed to perform the X-ray photoelectron spectroscopy (XPS) analysis. The binding

energies were referenced to the internal standard C 1s binding energy at 284.5 eV. XPS peaks are referenced to the C 1s peak. The shift of vanadium, titanium and oxygen peaks spectra was measured after C correction.

### **3.4.6 Impedance spectroscopy**

Parameters such as impedance values, sensor sensitivities, and response times relative to humidity and frequency were calculated using an impedance analyzer (Agilent 4294A) located at the METU-Central Laboratory (ODTÜ-MERLAB).



## CHAPTER 4

### INVESTIGATING THE HUMIDITY SENSING BEHAVIOR OF MICROPOROUS ETS-10 AND AM-6 THIN FILMS

#### 4.1 Characterization of as-synthesized ETS-10

The FE-SEM images and the X-ray diffraction pattern of as-synthesized ETS-10 crystals are shown in Figure 4.1. A typical bipyramidal morphology of ETS-10 with an average particle size of fewer than 0.5  $\mu\text{m}$  in Figure 4.1 (a) was observed. The six-coordinated Ti atoms in P25 act as structure-directing agents and promote fast nucleation of ETS-10 crystals. The XRD patterns of ETS-10 are similar to the ones in the literature[39], and no additional peaks were observed, as shown in Figure 4.1 (b).

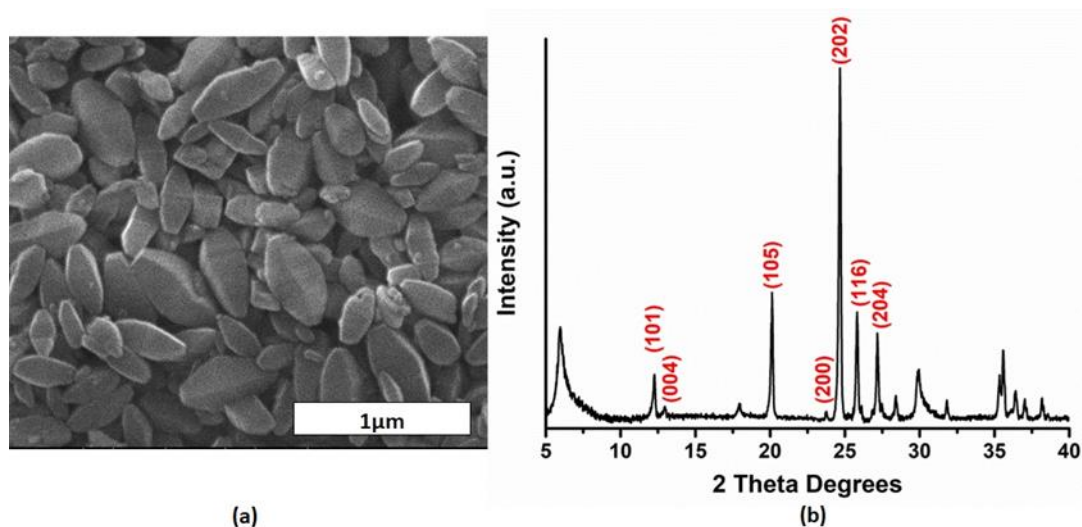


Figure 4.1. The FE-SEM image (a) and X-ray diffraction patterns (b) of ETS-10 crystals.

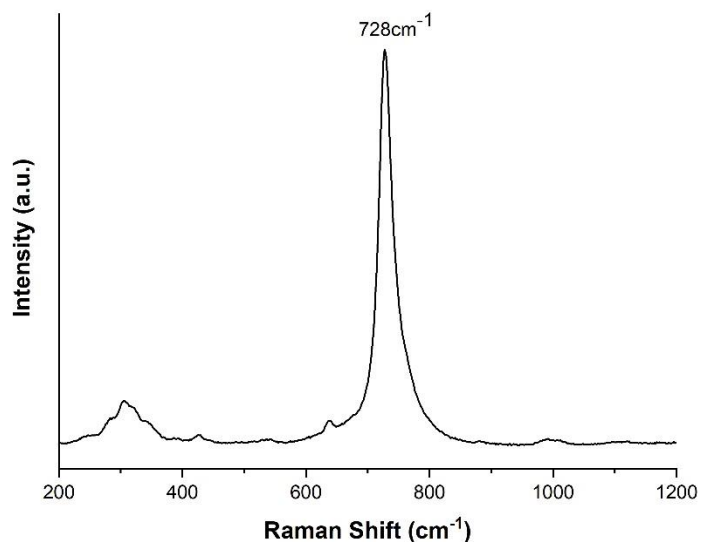


Figure 4.2. Raman spectra of ETS-10 crystals.

Raman spectra were taken to investigate the -Ti-O-Ti- quantum wires in the ETS-10 structure. Figure 4.2 shows the scattering band at  $728\text{ cm}^{-1}$  with a bandwidth of  $25\text{ cm}^{-1}$ , which belongs to the -Ti-O-Ti- stretching of the  $\text{TiO}_3^{2-}$  quantum wires [96], [97]. Depending on -Ti-O-Ti- chain length and concentration of defects, the position and the width of the peak can be different. Jeong et al. reported the Raman scattering band at  $724\text{ cm}^{-1}$  with a bandwidth of  $24\text{ cm}^{-1}$  to titanate quantum wires of  $> 50\text{ nm}$  length with very few defects, whereas a broader band had been observed at  $775\text{ cm}^{-1}$  for a highly defective ETS-10 sample [9]. Shifts towards higher frequencies for samples treated by acid or ion-exchanged samples have already been reported in a more defective ETS-10 [96], [98]. Pavel et al. said that peaks at  $600 - 400\text{ cm}^{-1}$  are assigned to Si-O-Si symmetric stretching vibration and peak below  $400\text{ cm}^{-1}$  is related to the bending motion of Si-O-Si and Si-O-Ti linkages [96]. Su et al. and F. Fan, C. Li et al. claimed that the peaks at  $396$ ,  $517$ , and  $638\text{ cm}^{-1}$  arise from the anatase  $\text{TiO}_2$ . The peak intensities have an inverse relationship with the crystallization of ETS-10 [11], [97]. Lv et al. assigned these minor peaks to various T-O-T, O-T-O (T = Ti or Si) bending and skeletal deformation modes and dramatically decrease by acid treatment [98]. In conclusion, the position and

intensity changes occurring with this peak can be used to identify defects created in the ETS-10 structure.

## 4.2 Characterization of as synthesized AM-6

The FE-SEM images and the X-ray diffraction pattern of as-synthesized AM-6 crystals are shown in Figure 4.3.

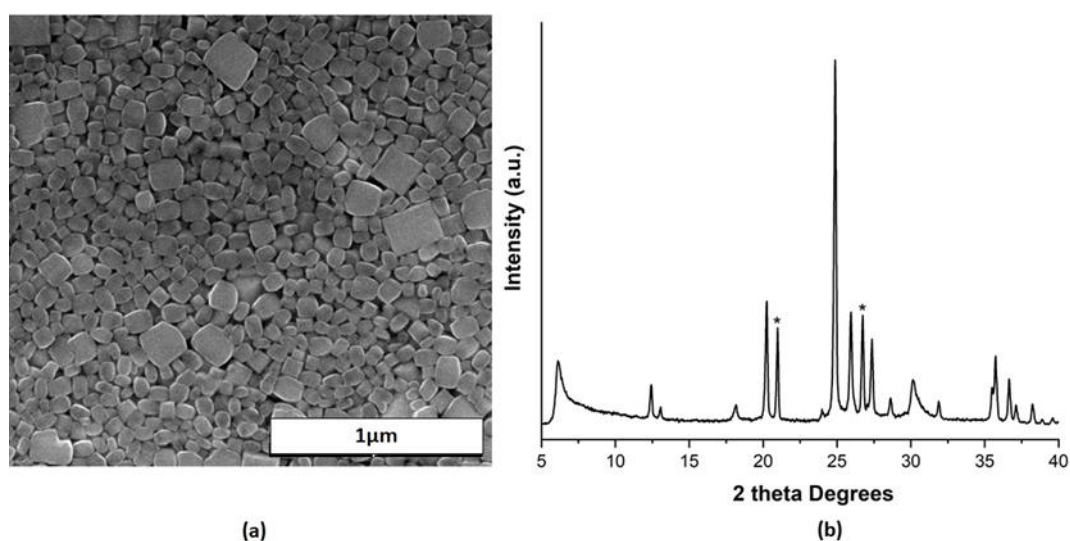


Figure 4.3. The FE-SEM image (a), X-ray diffraction patterns (b) of AM-6 crystals.

As mentioned previously in the literature Vanadosilicate AM-6 is an analog of Titanosilicate ETS-10 [49], [50]. Figure 4.3 (a) shows crystals of AM-6 with an average size of 200–500 nm, which is in correlation with the literature [50]. It is known that the vanadium source, which has different solubilities, can have an impact on the impurity level. In this particular case, Vanadyl sulfate was chosen as the vanadium source for seed crystals due to its relatively higher solubility. Figure 4.3 (b) shows XRD patterns of AM-6 which have the same peaks of ETS-10 with some quartz impurity (\*quartz peaks), which can be related to the solubility of Vanadyl sulfate.

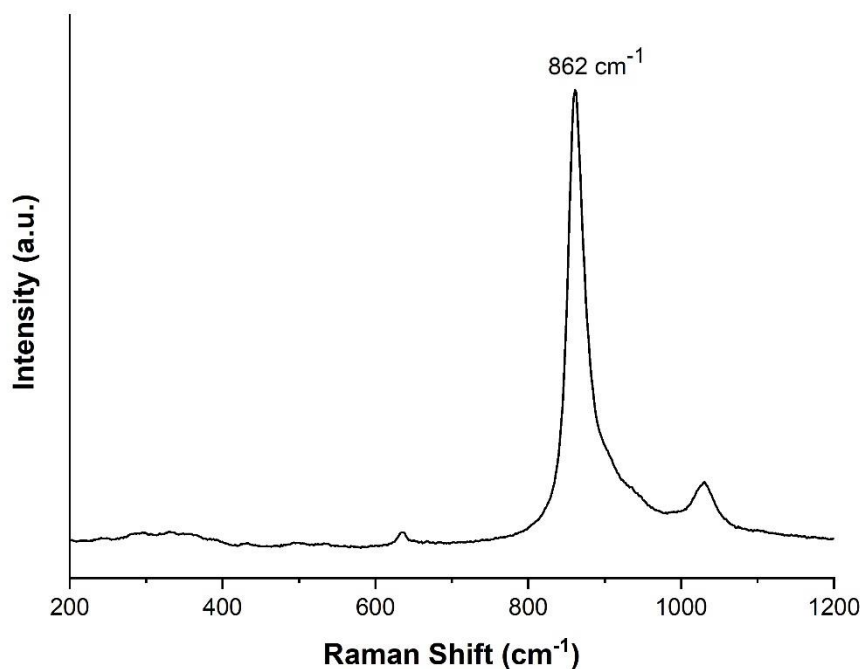


Figure 4.4. Raman spectra of AM-6 crystals.

Raman spectra of AM-6 in Figure 4.4 shows a Raman shift at  $862\text{ cm}^{-1}$  with a bandwidth of  $22\text{ cm}^{-1}$ , which belonged to the V-O-V stretching bonds of the  $\text{VO}_3^{2-}$  quantum wires. This peak is related to undistorted  $\text{VO}_6$  octahedra and depicts the  $\text{V}^{4+}$  in the V-O-V in the chain[11], [49], [99].

It was reported that the main AM-6 Raman shift could be seen in the range of  $860\text{--}870\text{ cm}^{-1}$ , whereas the Raman bands associated with V=O bonds usually appear at  $900\text{--}1000\text{ cm}^{-1}$ . Guo et al. reported V=O and Si-O in the Si-O-V moiety is  $1040$  and  $906\text{ cm}^{-1}$ , respectively, which further confirmed that the bands at  $906$  and  $1034\text{ cm}^{-1}$  are due to the distorted vanadium tetrahedron with a V=O bond[77]. In this study, the main V-O-V vibration was observed at  $862\text{ cm}^{-1}$  with an additional characteristic vanadium peak at  $1032\text{ cm}^{-1}$ . The main peak at  $862\text{ cm}^{-1}$  was used to observe the defects created along the V-O-V wires in the obtained films.

BET analyses of ETS-10 and AM-6 crystals were conducted to compare the surface area for these isostructural crystals. Table 5.1 shows that the total surface area values

obtained upon analysis and the obtained results are in correlation with the literature values [50]. Although not significant, the smaller pore size of AM-6 can be related to the smaller radius of Vanadium.

Table 4.1 BET analysis of ETS-10 and AM-6 samples

Sample Name	$S_{\text{total}}$ (m <sup>2</sup> /g) <sup>a</sup>	$S_{\text{Micro pore}}$ (m <sup>2</sup> /g) <sup>b</sup>	Pore Volume (cc/g) <sup>c</sup>	Pore size (Å) <sup>c</sup>
ETS-10	328.8	274.4	0.13	11.2
AM-6	298.1	254.1	0.12	11.0

a Determined by Multipoint BET

b Determined by t-Method

c Determined by SF Method

### 4.3 ETS-10 ve AM-6 thin films prepared by spin-coating method

FE- SEM images of the surface and the cross-section of the prepared films using seed crystals in Section 4.1 for ETS-10-2S and AM-6-2S crystals are shown in Figure 4.5a-b and Figure 4.5c-d, respectively.

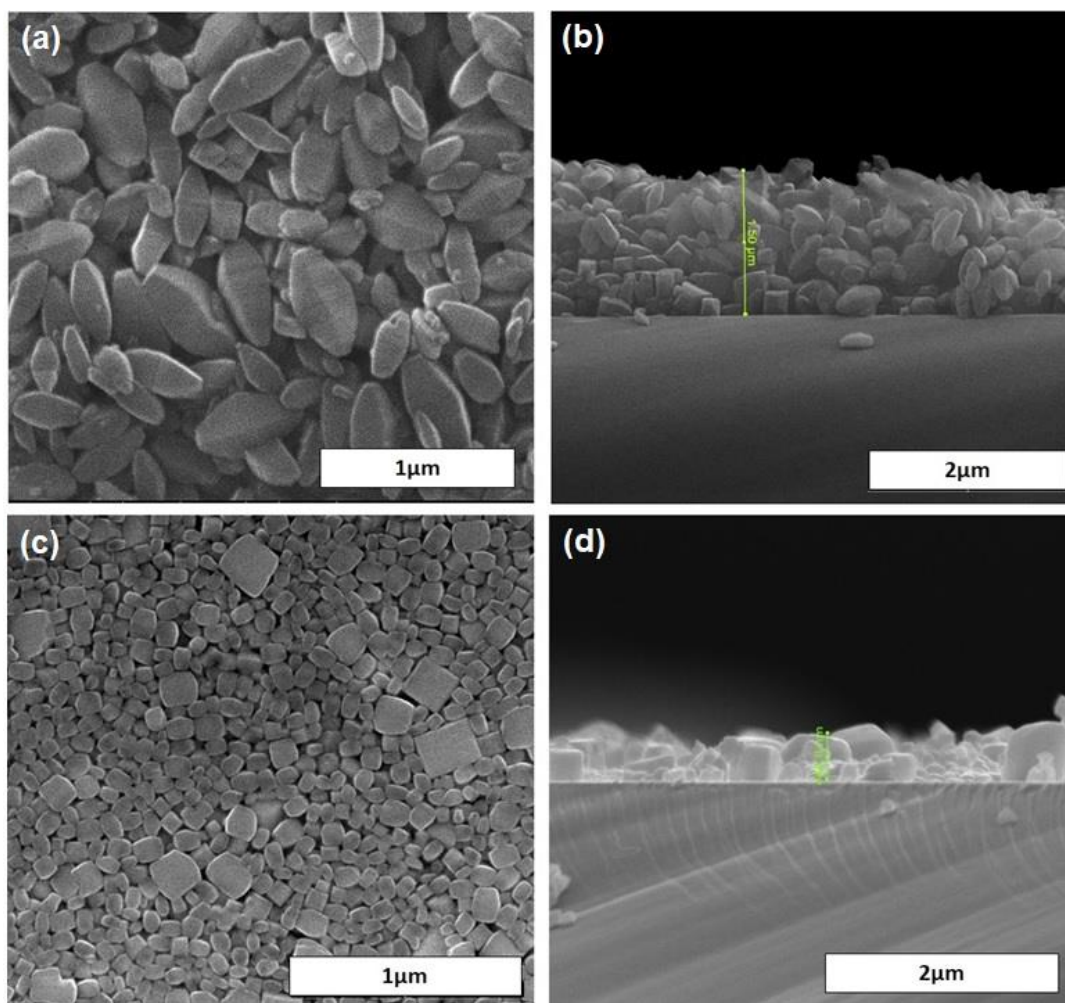


Figure 4.5. Top view and cross-sectional SEM images of ETS-10-2S (a),(b); AM-6-2S (c),(d), respectively.

Previous studies investigated different concentrations and coating steps to achieve full surface coverage by spin coating of ETS-10 crystal. Due to the results, the suspension prepared by 7 wt% of ETS-10 crystals gave better coverage than the suspension with 5 wt% of ETS-10 crystals [93]. In the case of coating step, less than 2 times spin coating is not enough to cover all the surface of the substrate by 7 wt% suspensions. Accordingly, ETS-10 and AM-6 crystals were uniformly coated on a quartz substrate, and thin films were prepared for humidity sensing investigations. The thicknesses of prepared films are summarized in Table 4.1.

Table 4.2. Thickness values of ETS-10-2S, AM-6-2S samples.

Sample code	Thickness ( $\mu\text{m}$ )
ETS-10-2S	1.32
AM-6-2S	0.45

The low thickness value reported for AM-6 sample compared to ETS-10 was due to the smaller crystal size of AM-6 powder crystals.

#### **4.3.1 Humidity sensing behavior of ETS-10-2S and AM-6-2S films prepared by the spin coating method**

This section summarizes the humidity sensing measurement results obtained from ETS-10-2S and AM-6-2S sensors explained in the above section using ETS-10 and AM-6 powders. The main aim was to specifically investigate the humidity sensing behavior with changing quantum wires since ETS-10 and AM-6 are two isostructural frameworks. The only difference is the T-O-T wires, V- for AM-6, and Ti- for ETS-10. The humidity sensing behavior of these thin films was investigated by measuring their impedance at different relative humidities (RH). All the measurements were performed at a frequency range of 100 Hz-1MHz with a constant applied voltage of 0.5 V. The relationships between the impedance modulus of prepared sensors and RH values measured at 100 Hz, 1KHz, 10KHz, 100KHz, and 1MHz are shown in Figure 4.6.

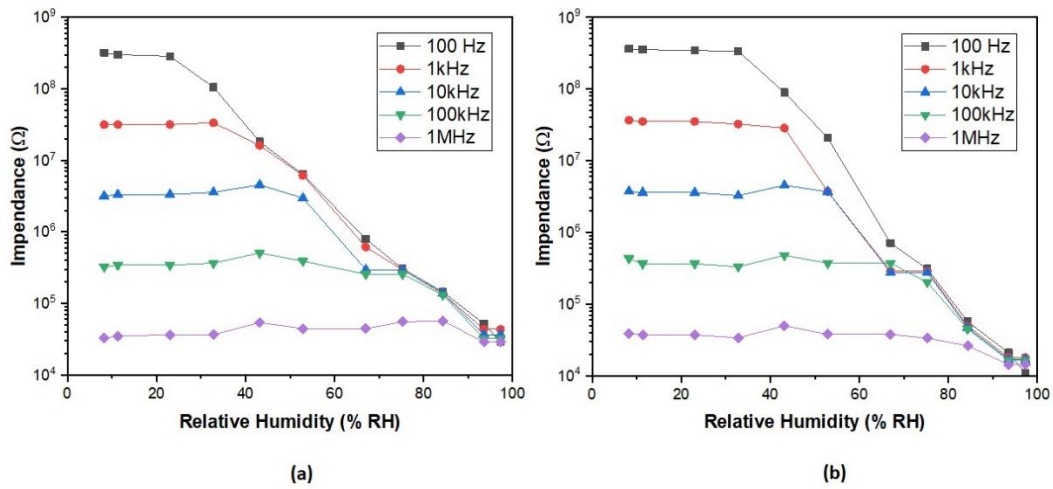


Figure 4.6. Relationship between impedance modulus and RH values at different frequencies for ETS-10-2S (a) and AM-6-2S (b) sensors.

Impedance measurements at different RH values obtained in the range of 8-97% RH showed that the relative humidity change at low frequencies (i.e., 100 Hz, 1 kHz) had a sharper slope. The impedance curve turned flat gradually at increased frequencies, i.e., 10 kHz, 100 kHz, and 1 MHz. Due to the literature, this fact was based on the polarization of water molecules at higher frequency values, where they cannot catch up with the speed of the electrical field. Thus, electronic displacement polarization and ion displacement polarization took place. Therefore, the effect of water molecules on impedance decreased [2]. From the measurements made at different frequencies, 100 Hz was chosen as an optimized frequency. Both ETS-10-2S and AM-6-2S sensors presented high humidity sensitivities and good linearities when RH was higher than 30%.

The impedance measurements for ETS-10-2S and AM-6-2S at 100 Hz are given in Figure 4.7 a-b. Accordingly, it can be concluded that both -Ti-O-Ti- and -V-O-V- based spin-coated films showed relatively good sensitivity and linearity, with a slightly improved linearity for ETS-10-2S (0.9818) than AM-6-2S (0.9391). It was seen that, the steady impedance values at low relative humidity levels (8%-32%) for AM-6-2S strongly affected the linearity and sensitivity values. Therefore, in Figure 4.7-c, the impedance vs. RH values in the range of 32%-97% was shown separately.



In the high RH range, AM-6-2S showed a higher sensitivity (0.071) than ETS-10-2S (0.053). Figure 4.7-d shows the response and recovery time of sensors measured by the simultaneous change of impedance from the relative humidity of 97% (response) to 32% (recovery) and vice versa.

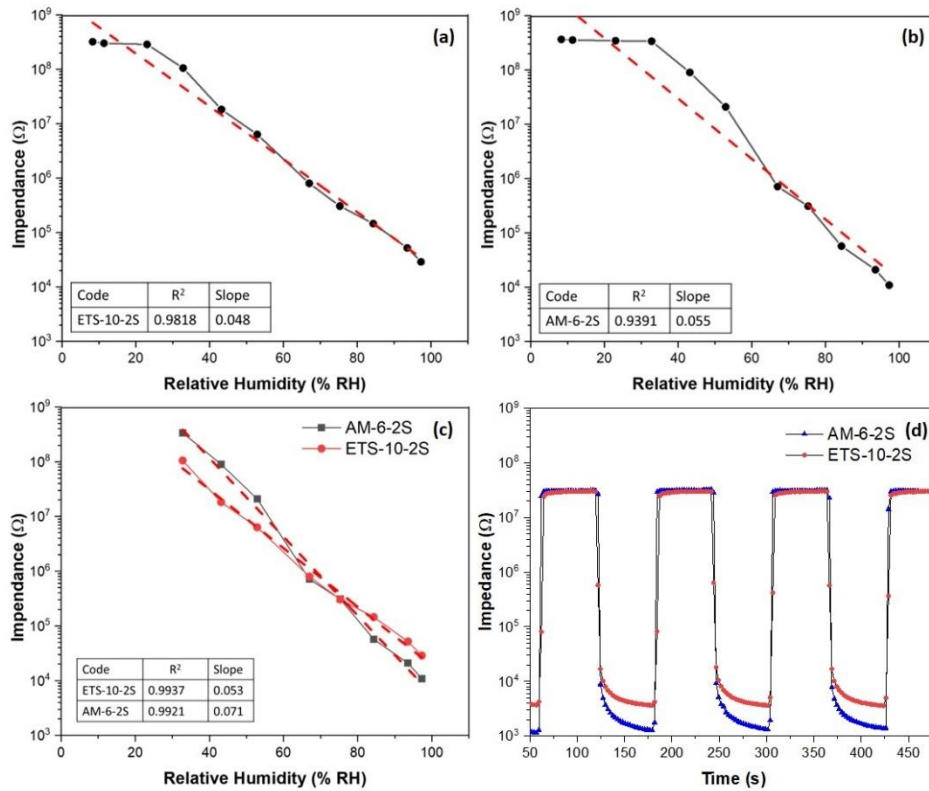


Figure 4.7. Variation of the impedance of ETS-10-2S and AM-6-2S sensor as a function of change in relative humidity at 100 Hz. The tables in each figure are derived from fitting the curves in the whole range (a,b,c); response and recovery times of both samples (d).

For both samples, impedance modulus change was seen to be more than three orders of magnitude in the range of 8-97% RH at 100 Hz. This phenomenon is related to increased layers of physisorbed water molecules on the surface upon increased RH, resulting in proton hopping mechanism and decreased impedance values [1]. Furthermore, the low sensitivity obtained at low relative humidity levels (LRH) can be related to the need for a sufficient number of active sites for water dissociation at

the surface. The sensitivity obtained on the surface at LRH is slightly different from the mechanism proposed at high relative humidity (HRH), which was speculated to happen through physisorption [26]. Accordingly, similar to semiconductor metal oxide humidity sensors at LRH, electronic conduction can be speculated to arise from the -Ti-O-Ti- and -V-O-V- chains in the current samples. The oxygen defects ( $O^-$ ,  $O^{2-}$ , etc.) on the surface with only a few adsorbed water molecules at very low RH values have been shown to result in electronic conduction [2]. It seems that a depletion layer might be surfacing around the -Ti-O-Ti- and -V-O-V- wires, in accordance with the  $TiO_2$  semiconductor humidity sensors in the literature [32], [100]. In the current study, the conduction was observed to be very low at a humidity range lower than 32%, as seen in Figures 4.7-a and b. Thus, creating some defect sites at LRH could potentially increase the water dissociation at those sites leading to increased humidity sensing. For that purpose, tailoring material properties by increasing active atomic defects like Ti-OH and unstable  $V^{+5}$  states, which can act as V-OH active sites at LRH ranges, can be a promising approach.

As shown in Figure 4.7-d and Table 4.3, the response time for ETS-10-2S and AM-6-2S was about 8 and 54 seconds, respectively. However, recovery time was less than 5 seconds for AM-6-2S and about 35 seconds for ETS-10-2S.

Table 4.3. Response and recovery time of ETS-10-2S and AM-6-2S samples.

<b>Sample code</b>	<b>Response time (s)</b>	<b>Recovery time(s)</b>
ETS-10-2S	8	35
AM-6-2S	54	5

These results suggest that the ETS-10 sample with -Ti-O-Ti- showed improved recovery, while AM-6 sample with -V-O-V- showed improved response time. According to these results, it can be hypothesized that water was bound more strongly, leading to harder desorption from the sites, resulting into longer recovery time for ETS-10 sample. Nevertheless, it seems that ETS-10 and AM-6 samples showed promising behaviors to be used as humidity sensors with significant features,

where each sample has distinct capabilities in different humidity behaviors. In order to investigate the insensitivity of the samples at LRH (8-32% RH), the effect of film thickness was studied by changing the number of applied coatings.

#### 4.3.1.1 Effect of film thickness on humidity sensing performance of ETS-10 films prepared by spin-coating method

In order to study the effect of film thickness on the humidity sensor's performance, ETS-10-2S films were prepared with 2, 4, and 8 times of coating steps (2S, 4S, and 8S). As shown in Figure 4.8, the impedance values decreased  $\sim 10$  times by increasing the number of coating steps, with a persistent insensitivity in LRH range. However, the linearity of ETS-10-4S and ETS-10-8S remained good. As shown in Figure 4.8-b and Table 4.4, the response time also increased from 8 to 47 and 68 seconds with increased thickness from 2S to 4S and 8S, respectively. Accordingly, thinner film formation seemed to show improved sensor performances for the currently investigated films.

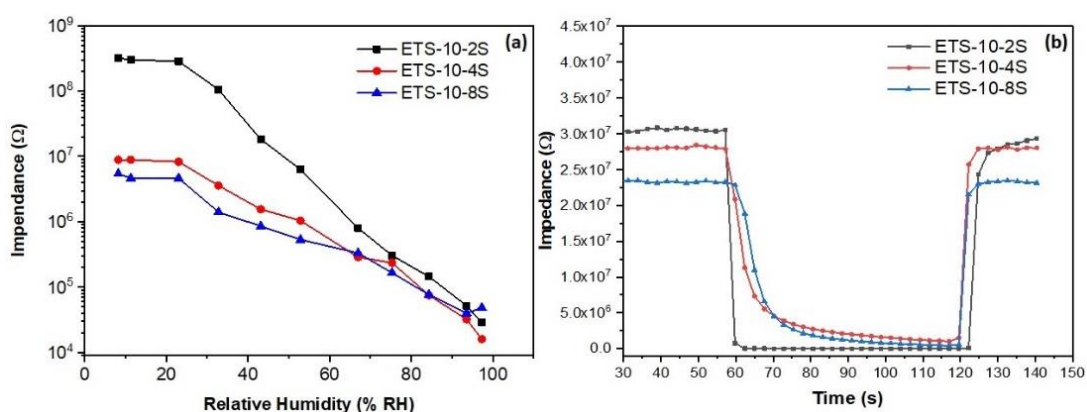


Figure 4.8. Impedance vs RH% response (a) and response and recovery plot (b) of ETS-10-2S, ETS-10-4S and ETS-10-8S samples at 100 Hz frequency.

Table 4.4. Thicknesses and Response and Recovery times of ETS-10-2S, ETS-10-4S, and ETS-10-8S samples.

Sample code	thickness ( $\mu\text{m}$ )	Response/Recovery time (s)
ETS-10-2S	1.32	8/35
ETS-10-4S	2.54	47/41
ETS-10-8S	4.67	68/73

As shown in Figure 4.8-b and Table 4.4, the response time also increased from 8 to 47 and 68 seconds with increased thickness from 2S to 4S and 8S, respectively. Accordingly, thinner film formation seemed to show improved sensor performances for the currently investigated films.

## CHAPTER 5

### HUMIDITY SENSING BEHAVIOR OF ETS-10 AND AM-6 FILMS PREPARED BY SECONDARY GROWTH METHOD

#### 5.1 Preparation of ETS-10 films on various substrates by Secondary growth method

In this part of the study, the secondary growth film production technique was investigated for humidity sensing applications. The secondary growth method is a two-step technique, as shown in Figure 3.1. In the first step, ETS-10 seed crystals were coated on different glass substrates using the spin coating technique described in section 3.2.1. In the preparation of the secondary growth gel, a different molecular composition was used than the molecular composition used for the production of ETS-10 seed crystals. This was done to investigate the effect of gel formula in the crystallographic preferred orientation (CPO), which was believed to affect the formation of quantum wires along the films [101]. For this purpose, substrates were spin-coated two times (2S) with ETS-10 crystals and were located inside Teflon-lined stainless autoclaves. The primary purpose of this study was to study the stability of the substrates withstanding harsh synthesis conditions, such as high pH (approximately 10.4) and reaction temperatures of 230°C.

In order to investigate the most suitable substrate with insulating properties, four different glass substrates, which are window glass, microscope glass, borosilicate glass, and alkali-free glass, were used, as shown in Figure 5.1.

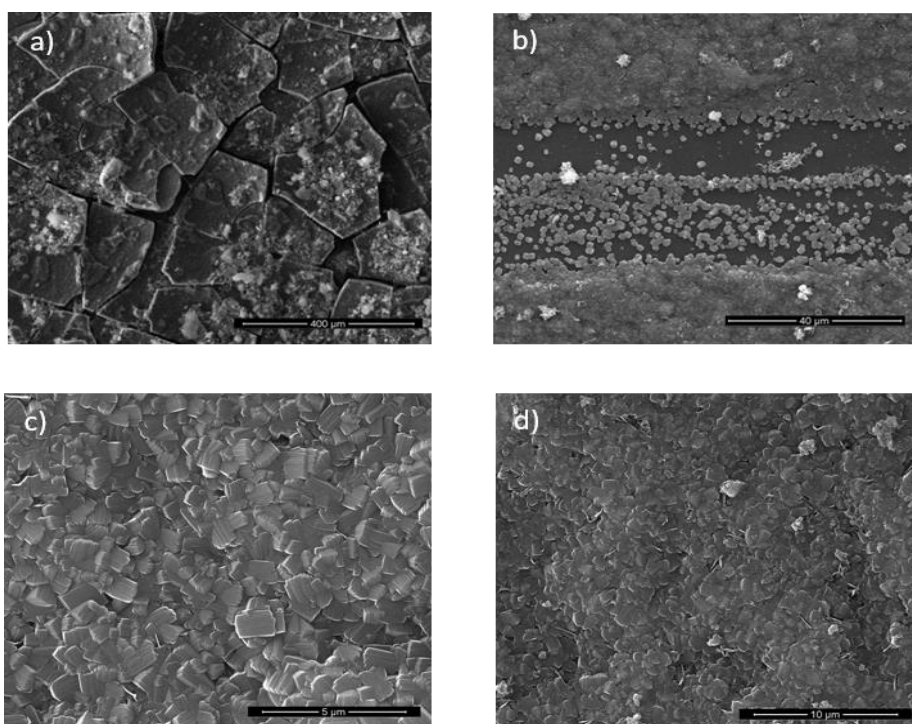


Figure 5.1. FE-SEM images ETS-10 secondary growth films on a window glass (a), microscope glass (b), borosilicate glass (c), and alkali-free glass (d) substrates.

As shown in Figure 5.1-a, the surfaces of the produced films corroded at high pH values when window glass was used, and the seed crystals were shed entirely from the substrate. Seed crystals remained with almost no film growth upon using microscope glass, which can be due to the high pH of the secondary growth gel (Figure 5.1-b). This may be due to the inability of the newly formed nuclei to adhere due to the smooth surface. Films prepared using borosilicate glass (Aluminoborosilicate, Schott Borofloat 33) and alkali-free glass (Schott AF 32 eco) are shown in Figures 5.1-c and d, respectively. Accordingly, the ETS-10 film was successfully intergrown as expected. Although films have been successfully obtained on Alkali-free and Aluminoborosilicate glass substrate surfaces, preparing zeotype films using these substrates requires a high cost. Hence, the search for alternative substrates continued, and zeotype thin films were made on porcelain substrates. In this context, hydrothermal growth of ETS-10 seed crystals was carried out by the secondary growth method on porcelain substrates.

## 5.2 Preparation of ETS-10 films with different thicknesses by Secondary growth method

This part of the study aimed to investigate the effect of changing the thickness and orientation of the seed layer on the properties of films using porcelain substrates prepared by the secondary growth method. This was investigated to see if any change would occur in the humidity sensor properties. For this purpose, in addition to the films in which the ETS-10 crystals are used as seed layers by the spin coating method (2S-TS), the dip coating method was also used to produce films with different thicknesses (1D/2D-TS) and crystallographic preferred orientations (CPO). The details on film preparation are listed in Table 3.3. Top and cross-sectional SEM images of the obtained secondary growth films from both spin-coated and dip-coated seed layers are shown in Figure 5.2.

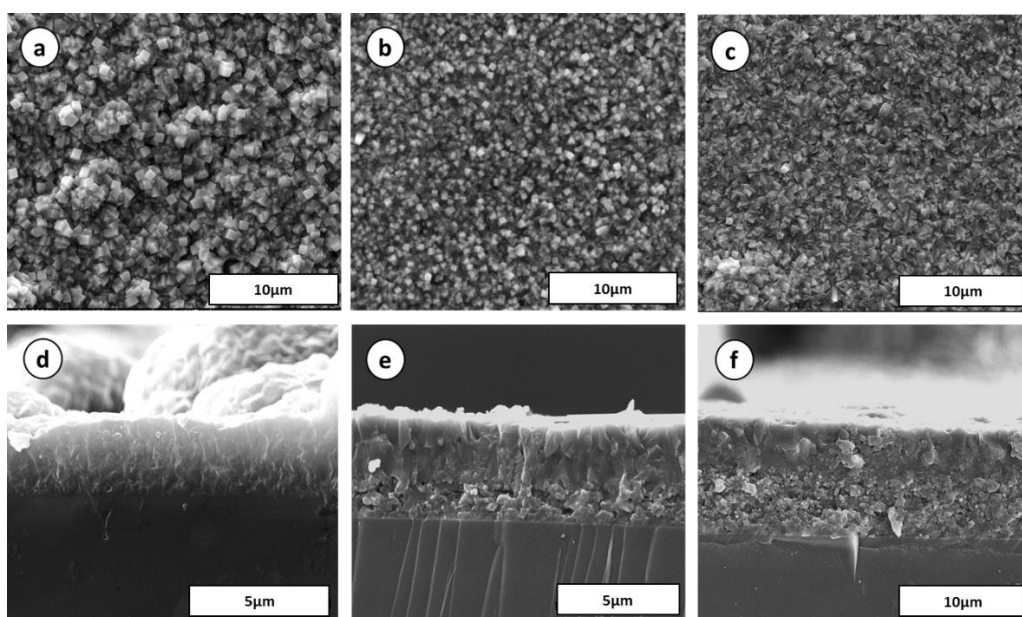


Figure 5.2. Top view and cross-sectional SEM images of 2S-TS (a), (d), 1D-TS (b), (e), and 2D-TS (c), (f).

As shown in Figure 5.2, changes in the seed layer coating technique also caused changes in film formation. The increased population of crystals forming the seed

layer with increased coating thickness affected the size and even the orientation of the films obtained on the coating layer, in correlation with the literature [102]. The thickness of the dip coating method increased from 4.38  $\mu\text{m}$  to 8.27  $\mu\text{m}$  with an increased population of seed crystals compared to the spin coating method with thickness of 2.67  $\mu\text{m}$ . When the dip coating method was applied two times, the highest population of seed crystals was reached. The increase in seed population is known to increase the number of nuclei sites exploited for film growth. Therefore, the nutrients in the secondary growth solution will not be sufficient for crystal growth. For this reason, smaller crystals were obtained in films obtained by dip coating with a high seed population. In addition, the increase in the seed population caused the seed crystals to collide with each other and change their orientation before they could grow sufficiently, which also affected the orientation of the crystals forming the films obtained [92].

XRD patterns of 2S-TS, 1D-TS, and 2D-TS were demonstrated in Figure 5.3. XRD patterns of the samples do not contain any impurities, and the XRD pattern is consistent with the XRD pattern described in the literature for ETS-10 [78]. These patterns were used to determine the crystal orientations (CPO). The thickness values and CPO calculation results are shown in Table 5.1. The positions of peaks for powder form and all the films were the same.



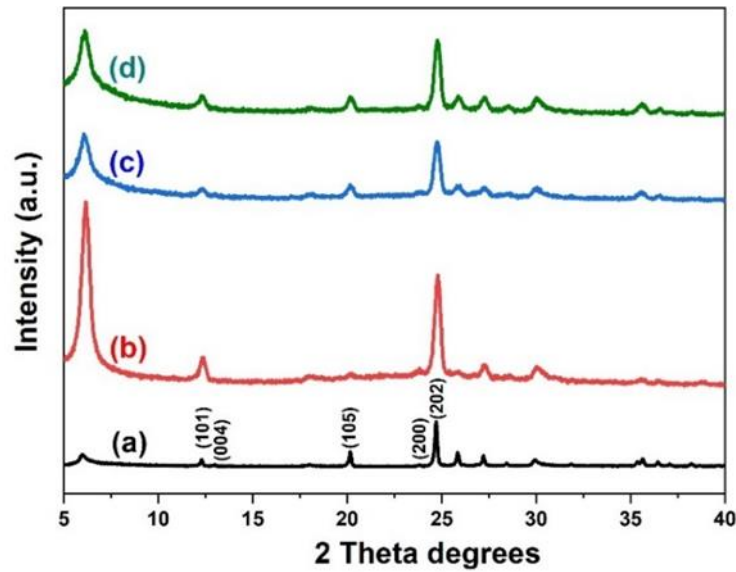


Figure 5.3. X-ray diffraction patterns of ETS-10 powder (a), 2S-TS (b), 1D-TS (c), and 2D-TS (d) films.

CPO values were calculated by considering the intensity of (200) and (105) planes to investigate the degree of  $a(b)$ -out-of-plane preferred orientation of films grown on the seeded substrates. As mentioned in Section 3.4.3,  $CPO_{200/105} = \frac{(I_{200}/I_{105})_f - (I_{200}/I_{105})_p}{(I_{200}/I_{105})_p}$  equation was used for calculations. In this equation,  $I$  depict the integrated intensity of the corresponding reflections, and the subscripts of  $p$  and  $f$  represent powder samples (randomly oriented) and films (preferentially oriented), respectively [78], [103].

Table 5.1. Thicknesses and CPO values of 2S-TS, 1D-TS, and 2D-TS.

<i>Sample code</i>	<i>Thickness (<math>\mu\text{m}</math>)</i>	<i>CPO</i>
2S-TS	2.67	10.45
1D-TS	4.38	4.70
2D-TS	8.27	1.54

As seen in Figure 5.3 and Table 5.1, there was a difference between the thickness of the films obtained by spin-coated and dip-coated seed crystals used as a seed layer. CPO calculation was performed for the quantitative analysis of the crystal orientations of 2S-TS, 1D-TS, and 2D-TS, and the results obtained are shown in Table 5.1. Rocha et al., calculated their CPO values to be around 20, which suggests longer chains along  $a(b)$ -direction with presumably fewer defects [85]. In the current study, the CPO value for 2S-TS was 10.45, while the CPO values for 1D-TS and 2D-TS were 4.70 and 1.54, respectively. The obtained values can be considered relatively small, suggesting short chains and preferred growth along  $c$ -direction. Nevertheless, the higher CPO value for 2S-TS film with the lowest thickness can be related to the faster growth rate of seed crystals along their  $a$ - or  $b$ - directions. This was aimed by choosing a specific gel solution that promotes a higher crystal growth rate in the  $a$ - and  $b$ -directions rather than the  $c$ -direction [78]. The main channels of ETS-10 parallel to  $a$ - or  $b$ - orientation were shown to enhance membrane properties [85].

The slight decrease in CPO values for dip-coated samples suggests a change in the growth direction of seed crystals due to an increase in the seed population, causing the seed crystals to change their direction upon meeting each other during hydrothermal growth. The  $2\theta$  degree of  $\approx 20^\circ$  (i.e., (105) plane) observed in the 1D/2D-TS films relatively increased by increasing the thickness by dip-coating of the seed layer for growth films due to the tendency of crystals to grow in  $c$ -direction. On the other hand, increasing the growth in the  $c$ -direction inhibits the further growth of -Ti-O-Ti- wires, which may cause defects like Ti-OH at the end of the chain [44]. In general, the change in the film production technique by converting from spin- to dip-coating seemed to affect the CPO values with a change in the thickness of the films.

### 5.3 Effect of thickness of prepared films by secondary growth on humidity sensing performance

This section shows humidity sensing measurements of 2S-TS, 1D-TS, and 2D-TS sensors, prepared by the secondary growth method. The humidity sensing behavior of these films was investigated by measuring their impedance at different relative humidity levels. All the measurements were done at the frequency range of 100 Hz-1MHz with a constant applied voltage of 0.5 V. The relationships between the impedance modulus of prepared sensors and RH with measuring frequencies at 100 Hz, 1kHz, 10kHz, 100kHz, and 1MHz are shown in Figure 5.4.

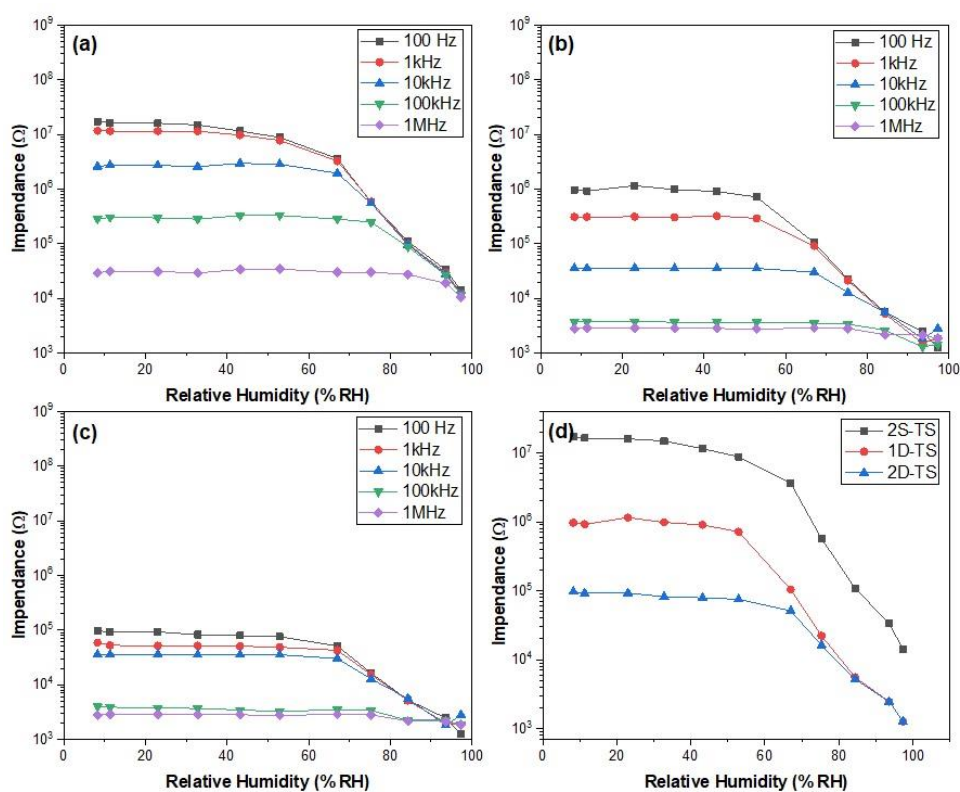


Figure 5.4. Relationship between impedance modulus and RH at different frequencies for 2S-TS (a), 1D-TS (b), and 2D-TS (c) sensors, comparison of impedance vs. RH% response of 2S-TS, 1D-TS, and 2D-TS at 100 Hz.

According to Figure 5.4, 2S-TS and 1D-TS sensors showed similar behavior at the RH range of 43-97%, while the 2D-TS sensor showed sensitivity in a narrower RH range of 67-97%. In addition, the 2S-TS and 1D-TS sensor showed a sensitivity of three orders of magnitude for HRH levels. However, the impedance values for 1D-TS film shifted to lower values in this range compared to 2S-TS, which could be related to the thickness of the film. The sensitivity for 2D-TS was in the order of two orders of magnitude, suggesting a decrease of 10 times in comparison with 2S- and 1D-TS films.

This difference in humidity sensor performance can be attributed to the difference in thickness and CPO values (Table 5.1). By increasing the thickness of the film and decreasing the CPO value in dip-coated samples, -Ti-O-Ti- chains became shorter, creating defective Ti-OH terminations. These Ti-OH sites can act as water sorption and dissociation sites [44]. It seems that a more sensitive sensor can be obtained using thinner films with optimized defect concentration. It could be concluded that electronic conduction was not improved at LRH levels upon an increased number of shorter chains and higher thicknesses, while proton hopping can be enhanced due to the high level of physisorption at HRH values, with a presumably higher number of dangling bonds. Nevertheless, it can be concluded that the applied modification technique only affected the HRH values.

The response and recovery time of 2S-TS, 1D-TS, and 2D-TS sensors are shown in Figure 5.5 and Table 5.2. As can be seen in Figure 5.4, the impedance values of 1D-TS and 2D-TS sensors changed insignificantly compared to 2S-TS sensors during the transition from a dry to a high humidity environment. The same is true for the recovery time, i.e., from low impedance to high impedance values.

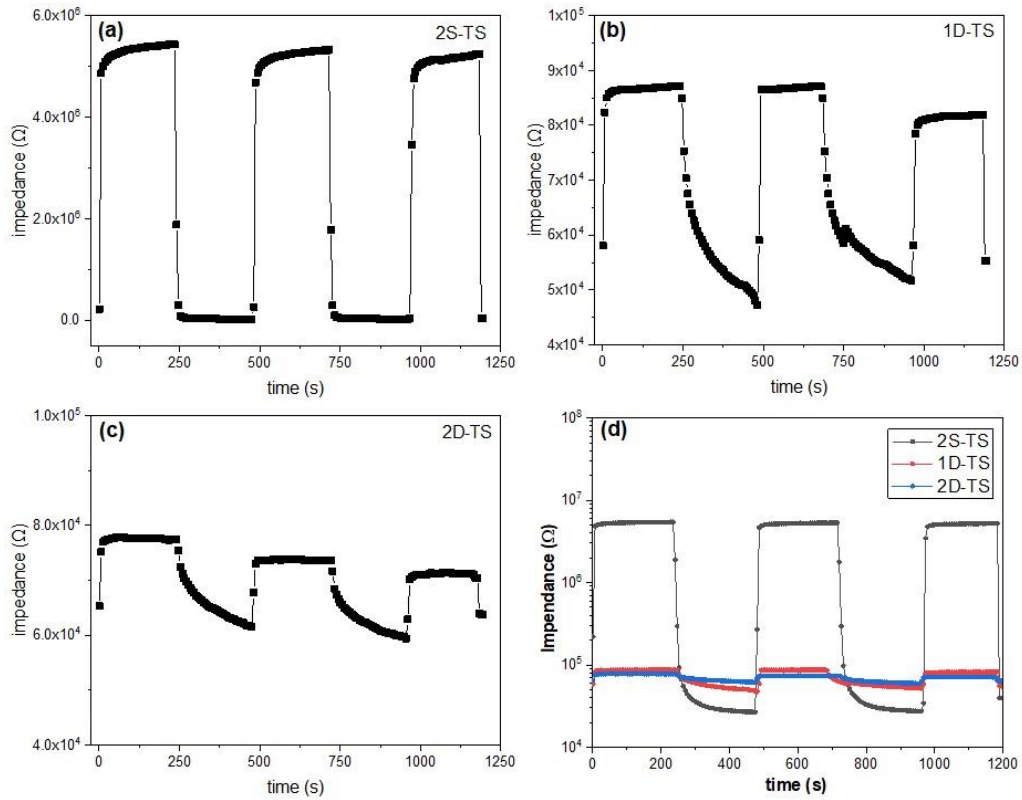


Figure 5.5. Response and recovery performance of 2S-TS (a), 1D-TS (b), and 2D-TS (c) sensors by changing relative humidity levels from 30% (dry environment) and 90% (high humidity environment), 2S-TS, 1D-TS, and 2D-TS sensors' response and recovery (d).

As shown in Table 5.2, a significant increase in response and recovery time was observed as the thickness increased. This may be due to the fact that with the increase in the thickness of seed crystals, there was a denser crystallization creating a different film morphology with a smaller particle size. These results were in correlation with the above mentioned results (Table 4.4), with the exception of a more significant decrease in CPO upon higher film thickness values.

Table 5.2. Thicknesses and response and recovery values of 2S-TS, 1D-TS, and 2D-TS.

<i>Sample code</i>	<i>Thickness (<math>\mu\text{m}</math>)</i>	<i>Response (s)</i>	<i>Recovery (s)</i>
2S-TS	2.67	30	100
1D-TS	4.38	150	210
2D-TS	8.27	250	310

#### **5.4 Preparation of AM-6 films with different gel formulations by Secondary growth method**

The AM-6 film growth process was similar to ETS-10, and not every substrate was suitable for AM-6 film formation. Porcelain surfaces were used as a substrate for producing AM-6 films due to their insulating properties. Therefore, experiments were continued with a porcelain substrate.

After successfully adapting the porcelain substrate to AM-6 film growth, two different secondary growth gels with varying precursors of vanadium were used to investigate the effect of different recipes on film properties like crystallographic preferred orientation (CPO) and the chemical structure of the final product. For ETS-10 films, this factor was achieved by changing the seed coating method, while for AM-6, the CPO difference was investigated by changing the solution chemistry. Accordingly, two different AM-6 films were obtained by using recipes with  $\text{V}_2\text{O}_5$  and  $\text{VSO}_4$  precursors in the secondary growth solution. The films were grown on the ETS-10 seed layer, which was two times spin-coated on the surface of the porcelain substrate. The prepared films by the secondary growth method were coded as 2S-VS<sub>1</sub> and 2S-VS<sub>2</sub>, respectively. Top and cross-sectional SEM images of samples coded 2S-VS<sub>1</sub> and 2S-VS<sub>2</sub> are shown in Figure 5.6.

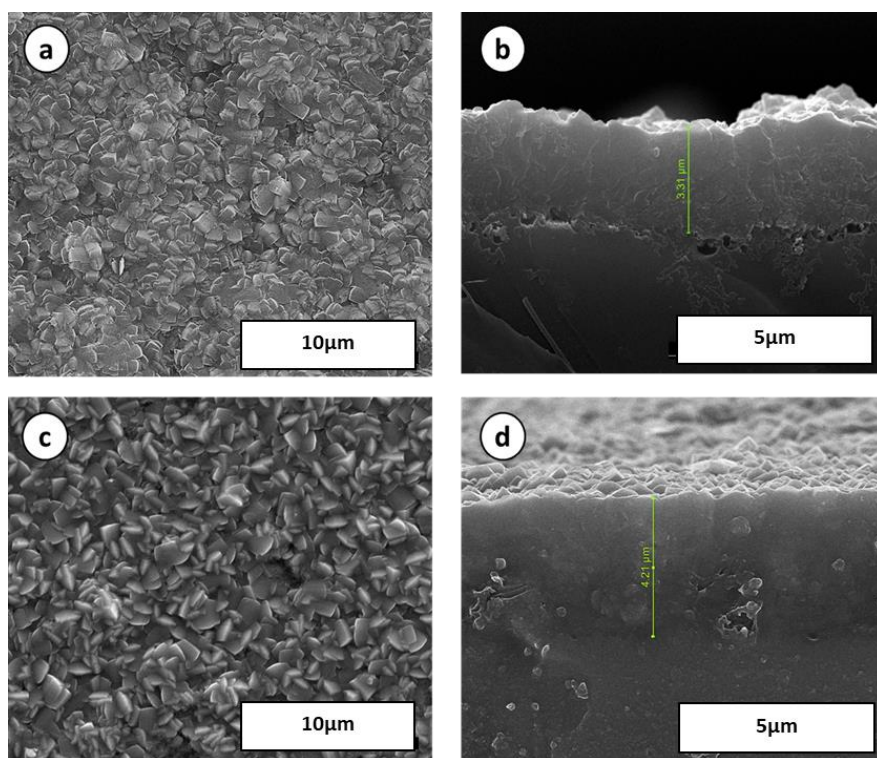


Figure 5.6. Top view and cross-sectional SEM images of 2S-VS<sub>1</sub> (a), (b), 2S-VS<sub>2</sub> (c), (d).

As shown in Figure 5.6, AM-6 films obtained using the secondary growth method with different chemical formulations also showed morphological differences. The difference observed in the film morphologies was also detected in literature studies where ITO glass was used as a substrate for the secondary growth of AM-6 films [92].

XRD analysis was performed to check whether the samples coded 2S-VS<sub>1</sub> and 2S-VS<sub>2</sub> contained any impurities and to determine the crystal orientations. The obtained results are shown in Figure 5.8.

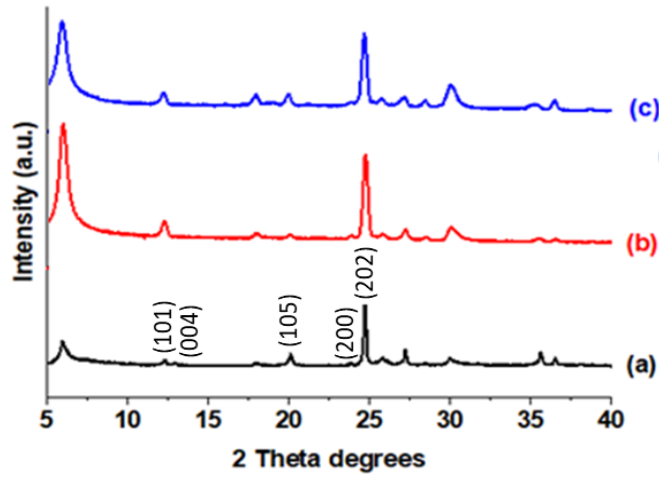


Figure 5.7. XRD patterns of ETS-10 powder (a), 2S-VS<sub>1</sub> (b), and 2S-VS<sub>2</sub> (c) films. As shown in Figure 5.7, the samples coded 2S-VS<sub>1</sub> and 2S-VS<sub>2</sub> did not contain any impurities, and their XRD pattern was compatible with the XRD pattern described for AM-6 films in the literature [49]. Since AM-6 and ETS-10 have the same structure, their XRD patterns were also the same. The positions of the XRD peaks of the samples matched well with that of the ETS-10 seed layer.

CPO calculation was performed for the quantitative analysis of the crystal orientations of the samples, and the results are shown in Table 5.3. Accordingly, while the sample coded 2S-VS<sub>1</sub> had a CPO value of 9.04, the CPO value of the sample coded 2S-VS<sub>2</sub> was calculated as 2.61. Although the obtained values were small, suggesting an *a(b)*-direction orientation for all samples according to the literature, it can still be inferred that the sample coded 2S-VS<sub>1</sub> had a higher tendency to grow in the *a(b)*-direction.

Table 5.3. Thicknesses and CPO values of 2S-VS<sub>1</sub>, 2S-VS<sub>2</sub>.

<i>Sample code</i>	<i>Thickness (μm)</i>	<i>CPO</i>
2S-VS <sub>1</sub>	3.31	9.04
2S-VS <sub>2</sub>	4.21	2.61



The characteristic vibrational bands of the -V-O-V- ( $\text{VO}_3^{2-}$ ) quantum wires in the AM-6 structure were characterized through Raman analysis to get more insight into the defects formed in the VS films made by using two different vanadium sources. The results obtained are shown in Figure 5.9.

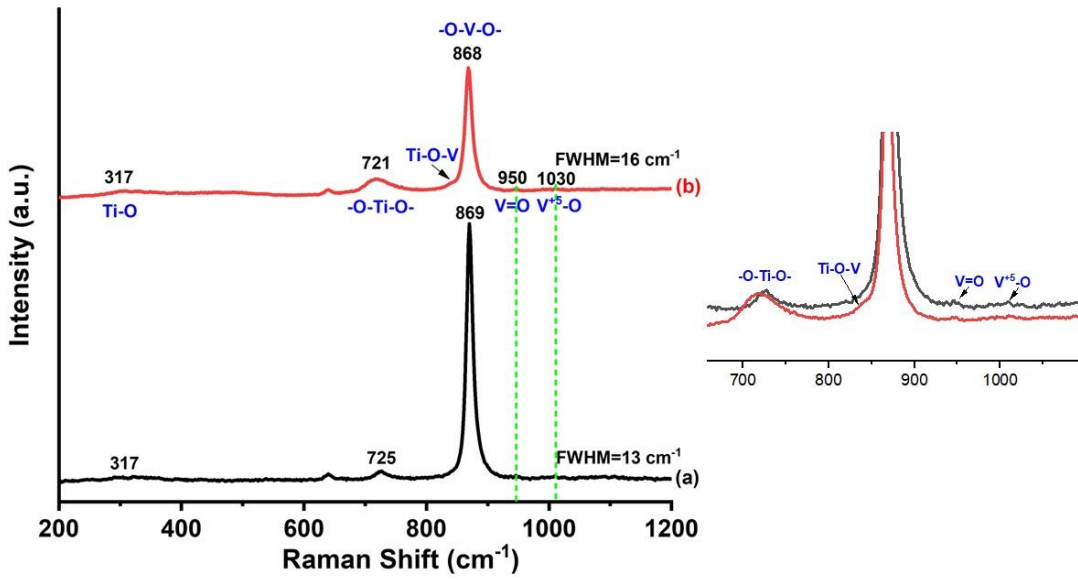


Figure 5.8. Raman spectra of 2S-VS<sub>1</sub> (a), 2S-VS<sub>2</sub> (b) films.

In the literature, the Raman frequency of the -V-O-V- vibrational band for AM-6 crystals was observed at 870  $\text{cm}^{-1}$  [95]. As shown in Figure 5.8, the -V-O-V- vibrational band frequency of 2S-VS<sub>1</sub> and 2S-VS<sub>2</sub> films were obtained at 869  $\text{cm}^{-1}$  and 868  $\text{cm}^{-1}$ , respectively, close to the value defined in the literature [49]. Furthermore, it can be said that the FWHM of the AM-6 were also comparable to the values defined in the literature, which were 13  $\text{cm}^{-1}$  for 2S-VS<sub>1</sub> and 16  $\text{cm}^{-1}$  for 2S-VS<sub>2</sub> [79]. These results show that zeotype AM-6 thin films were successfully fabricated on porcelain substrates. The Raman peak at approximately 870  $\text{cm}^{-1}$  is associated with the  $\text{VO}_6$  octahedral structure (quantum chain) in the AM-6 and is due to V-O stretching vibrations induced by octahedrally positioned  $\text{V}^{4+}$  cations [104]. The peak located at 950 and 1030  $\text{cm}^{-1}$  peak positions with a very low intensity indicates the characteristic Raman peak of the  $\text{V}^{5+}$  cations contained in the  $\text{VO}_3^{2-}$

quantum chains in the AM-6 structure [99]. These peaks appeared as a result of a distorted vanadium tetrahedron with a V=O bond [77].

According to Datta et al., the peak centered at  $640\text{ cm}^{-1}$  was ascribed to the bridging vibration of V-O-Si [105]. Since this peak is a very characteristic peak for AM-6 crystals in the current study (Figure 5.8), it seems more appropriate to assign this peak to V- related coordination as well, in agreement with Datta et al.

Peaks with very low intensities were observed at approximately  $317\text{ cm}^{-1}$  and  $721\text{-}725\text{ cm}^{-1}$ , indicating Ti-O stretching vibrations and the presence of ETS-10 structure in the AM-6 film structure. [47], [104]. Moreover, there is a tiny shoulder at  $840\text{ cm}^{-1}$  for the 2S-VS<sub>2</sub> sample, which can be related to V-O-Ti vibration [75]. Yoon et al. reported that using ETS-10 to synthesize AM-6 crystal could cause disruption of -Ti-O-Ti-O-V-O-V- quantum wires creating defects towards the formation of -Ti-OH- and -HO-V- sites at the core/shell interfaces [49]. The Raman peaks observed in this study were similar to the ones conducted by Guo and coworkers, where ETS-10 was used as the seed crystal for the formation mechanism of AM-6 crystals. This mechanism suggested that ETS-10 crystals used as seed crystals started to dissolve into small particles from the outer surfaces and these particles served as nucleation sites for AM-6 formation [106]. As known from the literature, vanadium sources (VOSO<sub>4</sub> and V<sub>2</sub>O<sub>5</sub>) used in AM-6 synthesis have different dissolution rates [49], [50]. These results suggest that the ETS-10 seed crystals acted as a core structure during the formation of AM-6 films.

The difference in the broadness of the Raman peak at  $721\text{-}725\text{ cm}^{-1}$  can be attributed to higher defect concentration in the 2S-VS<sub>2</sub> film. The higher defect concentration is in correlation with the observed lower intensity of -V-O-V- vibration at  $868\text{ cm}^{-1}$ , which is also slightly broader with respect to the one obtained for 2S-VS<sub>1</sub>. A shift to a lower wavenumber region for -Ti-O-Ti- peak, indicating that the average length of the titanate quantum wires in 2S-VS<sub>2</sub> was shorter than that in 2S-VS<sub>1</sub>. These results can be in correlation with the lower CPO values obtained for this sample.

The higher amount of defects obtained for 2S-VS<sub>2</sub> may be due to the different dissolution rates of the vanadium sources used in the synthesis [95]. The higher amount of defects proposed to be forming in 2S-VS<sub>2</sub> may be due to the difference in the dissolution rate of the VOSO<sub>4</sub> used as the vanadium source. Furthermore, the pH and the reaction temperatures for the VS<sub>2</sub> films with higher defect concentration could also induce the formation of these defects, especially in the presumed -Ti-O-V- wires.

In summary, all these results suggest that the applied synthesis conditions with varying parameters allowed one to obtain ETS-10/AM-6 core-shell films with controllably tailored defect concentration. Accordingly, the obtained films in this study with well-controlled structural differences were used to investigate their humidity-sensing behavior.

### **5.5 Humidity sensing performance of AM-6 films prepared by different Secondary growth gel formulations**

In this part, the humidity sensing performance of the films obtained by changing the chemical formulation of the secondary growth solution was investigated. Figure 5.9 shows the impedance measurement results of 2S-VS<sub>1</sub> and 2S-VS<sub>2</sub>, which were produced using two different molar formulations with varying CPO values.

According to Figure 5.9, 2S-VS<sub>1</sub> shows a low sensitivity behavior over the entire relative humidity range, while the 2S-VS<sub>2</sub> sensor shows high sensitivity (1000 times impedance change) over the entire relative humidity range. Both sensors show good linearity compared to ETS-10 sensors prepared by the secondary growth method in the previous section. This difference in humidity sensor performance can be attributed to defects arising from changes in crystal orientations (CPO values) and different vanadium precursors used for the growth of films.

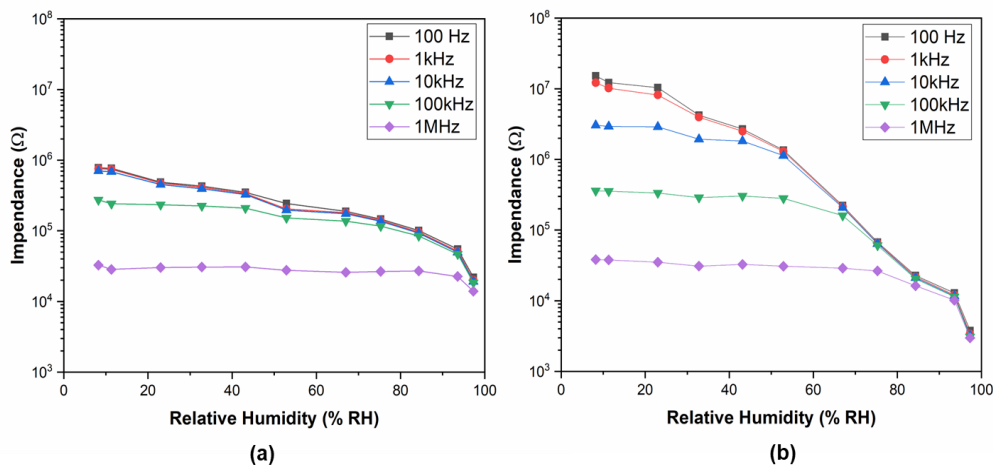


Figure 5.9. Relationship between impedance modulus and RH at different frequencies for 2S-VS<sub>1</sub> (a), 2S-VS<sub>2</sub> (b)

According to Figure 5.9, the 2S-VS<sub>2</sub> sensor showed a sensitivity of three orders of magnitude. In contrast, the sensitivity for 2S-VS<sub>1</sub> decreased to two orders of magnitude, suggesting a decrease of 10 times in comparison with 2S-VS<sub>2</sub> films. Despite ETS-10 films (2S/1D/2D-TS), these films show good sensitivity and linearity in the whole range.

The presence of -V-O-V- chains in the matrix results in electronic conduction at LRH levels. On the other hand, it seems that the proton conduction mechanism is mainly affected by the presence of V<sup>5+</sup>, distorted -Ti-O-Ti bond in the seed layer (ETS-10 as seed layer) and Ti-O-V bonds in the structure at LRH for 2S-VS<sub>2</sub>, which results in higher sensitivity in the whole range compared to 2S-VS<sub>1</sub>. The chemisorbed V-OH and Ti-OH groups act as water dissociation sites and increase the number of physisorbed water molecules on the surface and thus increase the sensitivity.

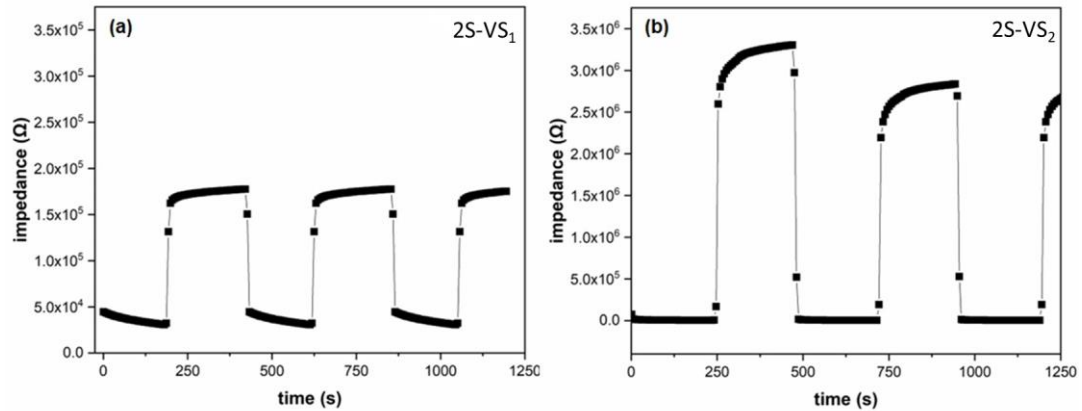


Figure 5.10. Response and recovery performance of 2S-VS<sub>1</sub> (a) and 2S-VS<sub>2</sub> (b) sensors by changing relative humidity levels from 30% (dry environment) to 90% (high humidity environment) and vice versa.

Figure 5.10 and Table 5.4 shows the response and recovery times of these sensors as a result of changing the chemical formulation of the secondary growth solution. As shown in Figure 5.10, the response and recovery time of the 2S-VS<sub>2</sub> sensor was significantly faster than that of the 2S-VS<sub>1</sub>. This shows the importance of the type of chemicals used for secondary growth and quantum chain structure on the performance obtained by humidity sensors.

Table 5.4. Response and recovery values of 2S-VS<sub>1</sub> and 2S-VS<sub>2</sub>.

<i>Sample code</i>	<i>Response time (s)</i>	<i>Recovery time (s)</i>
2S-VS <sub>1</sub>	50	110
2S-VS <sub>2</sub>	20	90

## 5.6 Complex impedance spectroscopy of films prepared by spin coating and Secondary growth methods

In order to understand the humidity sensing behavior of the sensors produced by the secondary growth method, the complex impedance spectrum of the humidity sensors was measured, as shown in Figure 5.11. In the graph, the x-axis corresponds to the

real part, and the y-axis to the imaginary part of the impedance. The graph points were measured at different frequency values over a certain frequency range. This graph is known as the "Nyquist plot of impedance." In this context, the complex impedance spectra of the sensors were measured in the range of 100Hz-10MHz in environments with 11.32%, 52.89%, and 93.58% relative humidity (low, moderate, and high humidity). As seen in Figure 5.11-a, the impedance values of the produced films increased very rapidly at high frequency and low relative humidity (11.32%), almost parallel to the y-axis. The reason is related to the low amount of physisorbed water in this humidity range. When the relative humidity reaches a moderate level (52.89%), the impedance spectrum of the sensor completes the semicircle shape. By increasing the humidity level, both the real and imaginary part of the impedance of the sensors decreases, and as a result, a semicircle appears. This is because the conductivity by proton hopping starts to increase with increasing humidity levels (Figure 5.11-b).

As shown in Figure 5.11-c, when the relative humidity increases to higher values, such as 93.58%, the impedance spectrum of the sensor shows an additional flat increase at low frequencies in addition to the semicircle. The Warburg impedance, which indicates the diffusion of water molecules, appears in high humidity environments. As a result, as the relative humidity of the sensors produced within the scope of this study increases, it has been observed that as the relative humidity increases, first, a semicircle appears by the Nyquist impedance representation. As the relative humidity increases, a straight line appears in accordance with the Warburg impedance. As a result of these measurements, equivalent circuits representing the humidity sensor behavior of the produced films were drawn.

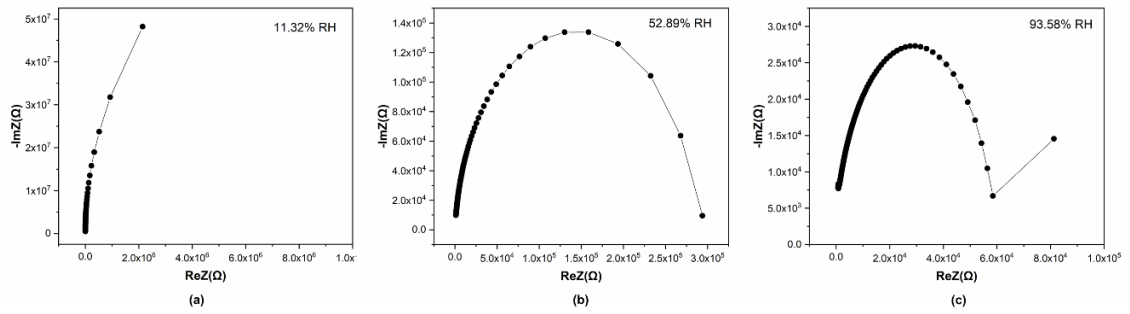


Figure 5.11. CIS measurements of sensors prepared by spin coating and secondary growth film production method at 11.32% (a) 52.89% (b) 93.58% (c) RH levels.

### 5.7 Effect of different film preparation methods on humidity sensing mechanism

In this section, the interaction of water molecules with films was discussed by considering the film preparation methods: spin coating and secondary growth. The spin coating method involves coating the substrates with ETS-10 or AM-6 crystals in powder form. The secondary growth method involves using films obtained from the spin (or dip) coating method (seed layer) on the substrates and growing a zeotype film layer on them. This method resulted in a more durable and stable film. The zeotype sensors prepared by these two different methods can be evaluated separately for low humidity (a), moderate humidity (b), and high humidity (c) levels. Both film-making techniques for these three different humidity levels are schematically shown in Figure 5.12. In general, the water adsorption mechanism should also be considered for three different crystal regions. These are intra-crystal water, inter-crystal water, and surface water.

Proton hopping in sensors produced by the spin-coating method can be explained as follows: As the relative humidity increases, the amount of inter crystalline water condensation increases, and eventually, the grain surfaces are covered with water. Under high humidity conditions, the surface of the grains is covered with a very thin layer of water (Figure 5.12-a). There is water in the nanopores and channels inside

the zeotype crystals. Water in the nanopores is present even at very low humidity levels. Proton hopping is the basic conduction mechanism of humidity sensors.

In sensors produced by spin coating at high humidity levels, proton hopping takes place from the grain surface and inside the crystals (Figure 5.12-a). At intermediate levels, conduction takes place in the grain boundary of crystals and by condensed water inside the crystal (Figure 5.12-b). At very low humidity levels (Figure 5.12-c), the conduction mechanism is mainly due to intra-crystal water.

In sensors produced by the secondary growth method, proton hopping takes place as follows. Despite the spin-coated films, nanopores in the secondary growth zeotype crystals are connected to each other at the grain boundaries. Therefore, it is possible for proton hopping to occur with the water in the inside crystals at low relative humidity levels (Figure 5.12-d and e). At high humidity, the conduction is similar to the previous type of sensors. At medium and low humidity levels, the rate of change of impedance relative to humidity is significantly affected by the parameters like thickness, secondary growth gel type (could be Ti or V)/formula, and CPO values. This may explain why morphological and chemical differences between the films and even differences in the internal structure of the zeotype films affect the humidity sensor performance.

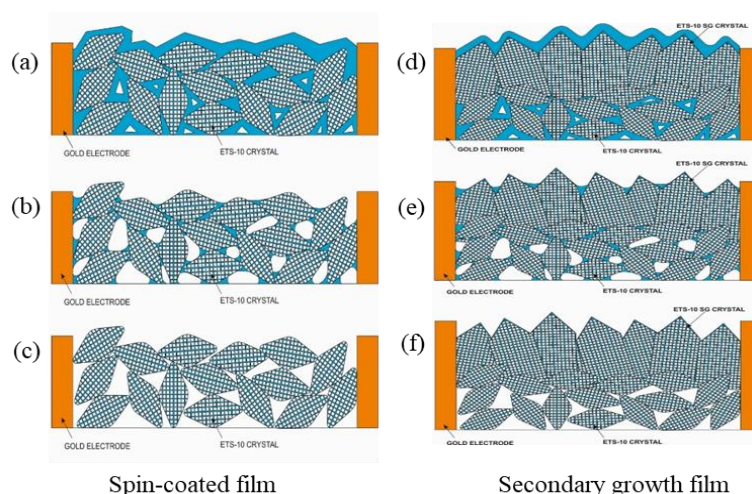


Figure 5.12. Schematic of water filling in the films prepared by spin-coated and secondary growth at high (a-d), moderate (b-e), and low (c-f) relative humidities.



## CHAPTER 6

### TAILORING HUMIDITY SENSING BEHAVIOR OF TITANOSILICATES WITH Ti-O-Ti WIRES BY VANADIUM SUBSTITUTION

#### 6.1 Characterization of as-synthesized ETS-10 and Vanadium substituted ETS-10 crystals

Figure 6.1 shows the XRD patterns of ETS-10 and vanadium-substituted  $V_x$ ETS-10 samples. The XRD patterns indicate the successful synthesis of ETS-10 by adding V-containing gel in differing amounts. All samples show good crystallinity with minor impurities in only  $V_{0.2}$ ETS-10 and  $V_{0.3}$ ETS-10 samples. When the amount of vanadium was increased in the synthesis gel, the amount of quartz and anatase impurities also increased, as indicated by XRD patterns. It can be concluded that the addition of vanadium source into the synthesis gel in differing amounts resulted in the successful formation of V-incorporated samples of ETS-10.

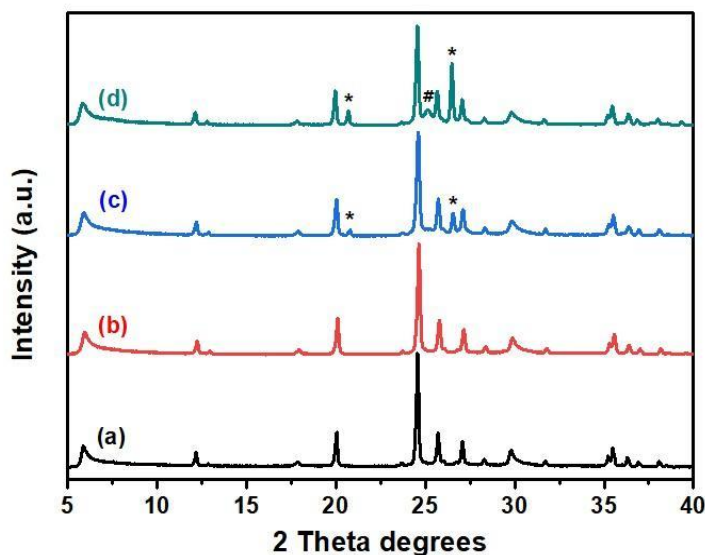


Figure 6.1. XRD patterns of ETS-10 (a),  $V_{0.1}$ ETS-10 (b),  $V_{0.2}$ ETS-10 (c),  $V_{0.3}$ ETS-10(d) (\*quartz, #anatase) impurities.

The chemical composition of ETS-10 and vanadium-substituted ETVS-10 samples are shown in Table 6.1.

Table 6.1 Bulk Atomic ratio of samples ETS-10, V<sub>0.1</sub>ETVS-10, V<sub>0.2</sub>ETVS-10, and V<sub>0.3</sub>ETVS-10.

<i>Sample</i>	<i>V/(V+Ti)</i>	<i>Si/(V+Ti)</i>	<i>(Na+K)/(V+Ti)</i>
ETS-10	0	4.56 ± 0.02	1.65 ± 0.03
V <sub>0.1</sub> ETS-10	0.10 ± 0.01	2.58 ± 0.06	0.99 ± 0.17
V <sub>0.2</sub> ETS-10	0.20 ± 0.01	2.15 ± 0.11	1.10 ± 0.07
V <sub>0.3</sub> ETS-10	0.31 ± 0.00	3.69 ± 0.12	1.21 ± 0.07

The elemental composition of the samples was found to correlate well with the expected results from the synthesis gel. Increasing vanadium content in the synthesis gel resulted in a gradual increase of vanadium content in the V<sub>x</sub>ETS-10 samples showing the successful replacement of vanadium with titanium atom (x indicates the atomic weight ratio of vanadium in the structure of ETS-10). Accordingly, the total amount of V + Ti increased for higher vanadium content, resulting in a gradual decrease in Si/(Vi+Ti). However, this ratio increased again for sample V<sub>0.3</sub>ETS-10, probably due to a significant increase in the silica-containing impurity.

The (Na + K)/ (V + Ti) ratio of unmodified ETS-10 was comparable with the literature data [75]. However, this ratio decreased with the substitution of vanadium in its structure concerning the original sample. This may be due to the presence of extra-framework sites in which the V<sup>4+</sup> and V<sup>5+</sup> ions would balance some of the framework charges and result in an overall decrease in the (Na + K) content. Different amounts of V<sup>4+</sup> and V<sup>5+</sup> cations in the structure would cause the need for different amounts of Na and K ions to balance the electroneutrality of the overall structure. In addition to these, the micropore volume of the original sample may

increase with the incorporation of vanadium since the sizes of  $V^{4+}$ , and  $V^{5+}$  cations are slightly smaller (i.e., 0.68 Å, 0.72 Å, and 0.75 Å for  $V^{5+}$ ,  $V^{4+}$ , and  $Ti^{4+}$ , respectively) [75].

Raman analysis was used to determine the characteristic vibration peaks of V-O-V and Ti-O-Ti in the structures of ETS-10 and V-substituted ETS-10 samples (Figure 6.2). A prominent band at ca.  $725\text{ cm}^{-1}$  is due to symmetric Ti-O stretching vibration in octahedral  $TiO_6$  units along the -Ti-O-Ti- chains. The FWHM of this band broadens as the vanadium content increases from 22.01 for ETS-10 to 25.7, 28.9, and 34.03 for  $V_{0.1}$ -ETS-10,  $V_{0.2}$ -ETS-10, and  $V_{0.3}$ -ETS-10, respectively. FWHM of this band is used to identify the length homogeneity and quality of the quantum wires in ETS-10 crystals [10]. The V-substitution seems to create defects in these wires, along with the appearance of new bands. The Raman spectra of V-substituted  $V_x$ -ETS-10 samples showed an additional longitudinal V-O-V ( $V^{4+}O_3^{2-}$  chains) vibration at  $870\text{ cm}^{-1}$ , besides small vanadium peaks at  $640\text{ cm}^{-1}$  which is assigned to various T-O-T, O-T-O (T = Ti or Si) bending by Lv et al. [98]. However, Datta et al. claimed that the peak centered at  $640\text{ cm}^{-1}$  is ascribed to the bridging vibration of V-O-Si [105]. The peak at  $840\text{ cm}^{-1}$  is related to the V-O-Ti vibration band [75]. The main band at  $870\text{ cm}^{-1}$ , which increases in intensity with vanadium, was ascribed to undistorted  $VO_6$  octahedra. The gradual broadening and decreasing intensity of  $725\text{ cm}^{-1}$ , in combination with the increasing intensity of  $870\text{ cm}^{-1}$  bands, indicates the replacement of vanadium for titanium in the framework with some considerable defect formation along the wires. Accordingly, it seems that while  $V_{0.2}$ -ETS-10 shows some significant deformation in the wires with new V-O band formations, the considerably different Raman spectrum of  $V_{0.3}$ -ETS-10 can be indicative of excessive vanadium doping in the structure of ETS-10. This behavior was also ascribed to a change in the local environment of the chains [75].

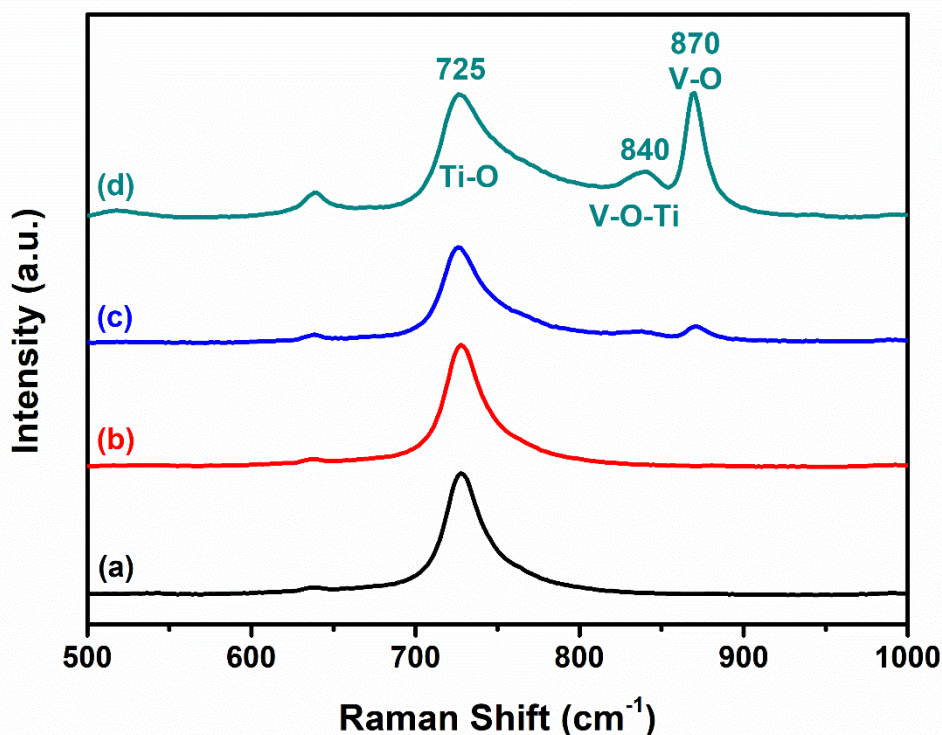


Figure 6.2. Raman spectra of ETS-10, V<sub>0.1</sub>ETS-10, V<sub>0.2</sub>ETS-10, and V<sub>0.3</sub>ETS-10.

The morphologies, i.e., the crystal size of AM-6, which is isostructural with ETS-10, were shown to have an impact on the optical, magnetic, and vibrational properties of these wires due to the unpaired electrons residing on the wire [9]. It is known that the defects created upon breakage of the Ti-O-Ti wire could affect the adsorption behavior of water and, thus, the sensor behavior [52]. The addition of vanadium and its state was shown to induce the formation of -OH groups and electron transfer, improving the adsorption ability [107]. Knowing that the factors affecting the defect formation with a possible change in humidity sensing performance could be based on different oxidation states of V<sup>4+</sup> and V<sup>5+</sup> formed [74], [75]. The change in the crystal size [9], SEM, and XPS investigations were carried out to get more insight into the nature of the Ti-O-Ti wires of ETS-10 upon vanadium substitution.

High-resolution FE-SEM images of ETS-10 and  $V_x$ ETS-10 are demonstrated in Figure 6.3.

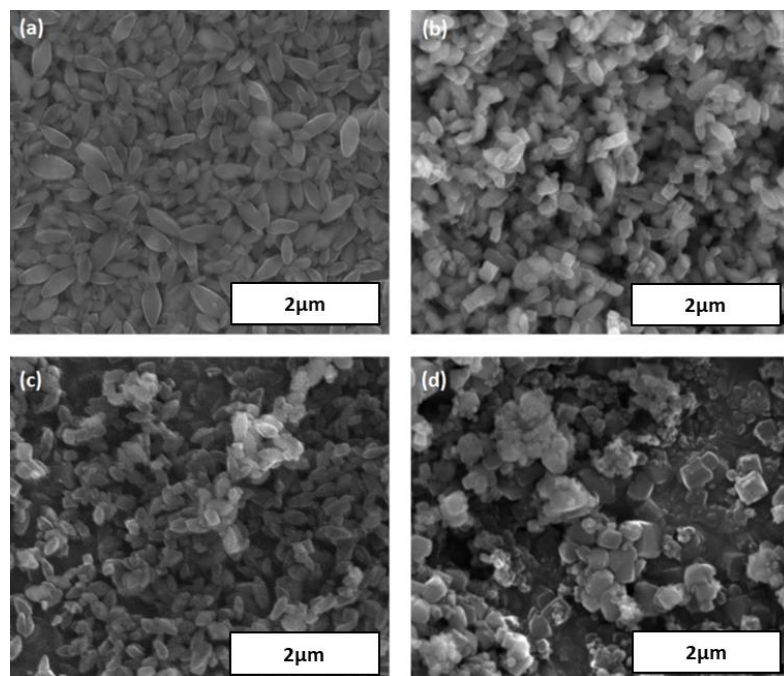


Figure 6.3. SEM images of ETS-10 (a),  $V_{0.1}$ -ETS-10 (b),  $V_{0.2}$ -ETS-10 (c), and  $V_{0.3}$ -ETS-10 (d).

Accordingly, as shown in Figure 6.3-a typical ETS-10 crystals of approximately 500  $\mu\text{m}$  with elongated square bipyramidal morphology were obtained [76]. It seems that the addition of vanadium in the synthesis gel led to a slight decrease in particle size with a mixture of truncated bipyramidal and cubic-like crystals in addition to square bipyramidal morphology, as shown in Figure 6.3-b and c ( $V_{0.1}$ -ETS-10 and  $V_{0.2}$ -ETS-10). Further increase in vanadium content resulted in bigger crystals with a more significant formation of cubic-like morphology and larger agglomerates of possible impurities.

XPS analyses were conducted to investigate the chemical states of Ti ( $\text{Ti}^{3+}$  and  $\text{Ti}^{4+}$ ) in the structure of ETS-10,  $V_{0.1}$ ETS-10,  $V_{0.2}$ ETS-10, and  $V_{0.3}$ ETS-10.

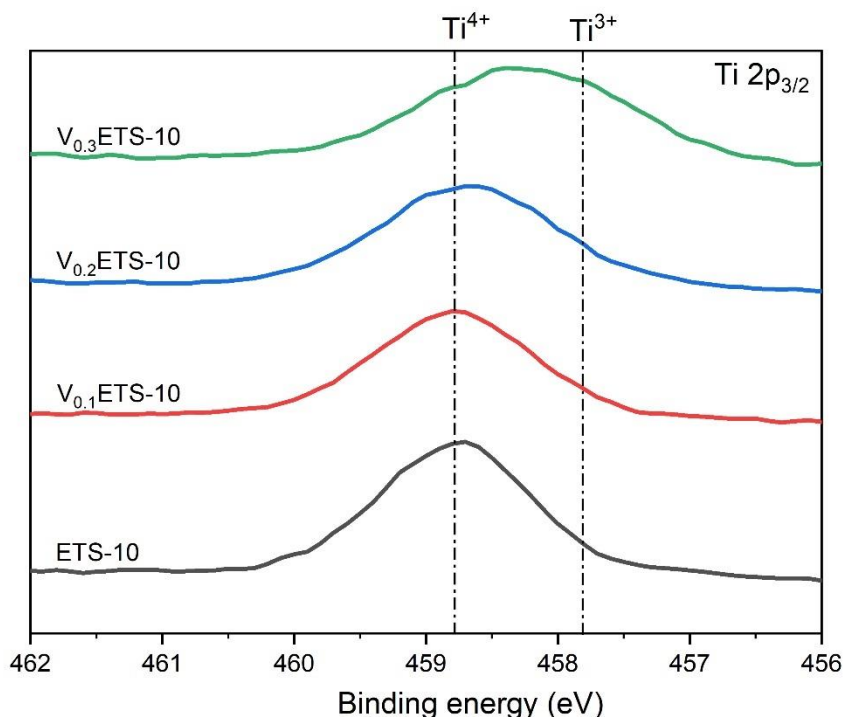


Figure 6.4. XPS spectra of Ti( $2p_{3/2}$ ) binding energies of ETS-10 and vanadium-substituted ETS-10 samples.

As shown in Figure 6.4, the XPS peaks at around 457.8 eV and 458.7 eV are assigned to Ti  $2p_{3/2}$  of  $Ti^{3+}$  and  $Ti^{4+}$  [10]. By increasing the amount of doped vanadium from  $V_{0.1}ETS-10$  to  $V_{0.2}ETS-10$  and  $V_{0.3}ETS-10$ , a significant shift in the main peak towards the lower binding energy was observed, which suggested the decreasing amount of  $Ti^{4+}$  with an increasing amount of  $Ti^{3+}$ . A similar shift was seen for V-doped  $TiO_2$ , which was attributed to the increased non-stoichiometry of  $TiO_2$  NPs toward  $Ti^{3+}$  [107]. It was also claimed that the  $Ti^{3+}$  states emerged along with  $Ti^{4+}$  states with increasing V-doping levels, reflecting the presence of oxygen vacancies in the  $TiO_2$  structure [108]. Liu et al. studied photocatalysis under vacuum conditions showing similar results for vanadium-doped  $TiO_2$ . A shift to lower binding energy in all cases indicated an increase in the electron density around Ti in doped  $TiO_2$ , which was attributed to the formation of  $Ti^{3+}$  [109]. By doping  $V^{4+}$  cation into the structure of  $TiO_2$ ,  $Ti^{3+}$  cations were created, reducing  $Ti^{4+}$  cations.  $Ti^{3+}$  cations can be

hypothesized to increase charge carrier mobility behavior, which could be effective for humidity sensing performances.

In the case of ETS-10, Yoon et al. claimed that the contribution of  $Ti^{3+}$  to the electronegativity of the cation was higher than that of  $Ti^{4+}$ . It could be explained by the richer electron density of  $Ti^{3+}$  species than  $Ti^{4+}$ , which could significantly enhance the electronic conductivity [10], [110]. It seems that the occurrence of  $Ti^{3+}$  is happening in conjunction with vanadium doping. Thus, vanadium XPS analysis was also conducted.

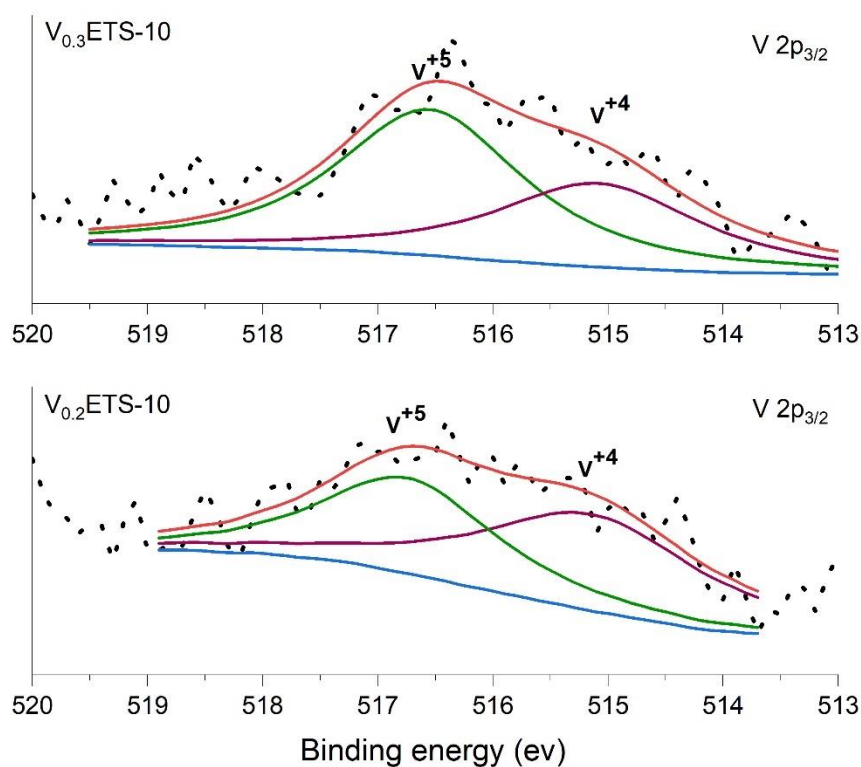


Figure 6.5. XPS spectra of  $V(2p_{3/2})$  binding energies of vanadium-substituted ETS-10 samples.

XPS analyses were conducted to investigate the chemical states of V ( $V^{4+}$  and  $V^{5+}$ ) in the structure of vanadium-doped samples. Since the amount of vanadium was very low for the  $V_{0.1}ETS-10$  sample, deconvolution was only applied to  $V2p_{3/2}$  peak of

$V_{0.2}$ ETS-10 and  $V_{0.3}$ ETS-10 by using XPSPEAK41 and mixed Gaussian-Lorentzian function. The obtained results are shown in Figure 6.5. While the dotted lines represent the original XPS data, the straight lines represent the deconvoluted data.

The percentages of the relative areas of  $V^{4+}$  and  $V^{5+}$  were calculated based on assuming their total amount was 100%. Accordingly, as the vanadium doping level increased, the area of  $V^{4+}$  decreased from 55.84% to 32.76%, while the area of  $V^{5+}$  increased from 44.6% to 67.23% (Figure 6.5). These results indicated that vanadium exists in two different oxidation states in the structure with a more significant amount of  $V^{5+}$  as the vanadium doping level increased. The  $V^{5+}$  cations are considered as a defect site in the structure. In the case of photocatalytic activity, an optimized amount of this site was shown to enhance the photocatalytic performance. Besides, the existence of a  $V^{5+}$  cation created an unoccupied mid-gap state, which acted as an electron trap. Also, beyond an optimal vanadium concentration, these sites started acting as recombination centers reducing the overall reactivity [75]. A similar optimized level of vanadium doping level was also observed in the literature for other photocatalytic applications of ETS-10, where vanadium incorporation should not exceed a certain level, and excessive doping can cause the total deformation of the structure due to the unstable nature of  $V^{5+}$ [74], [76].



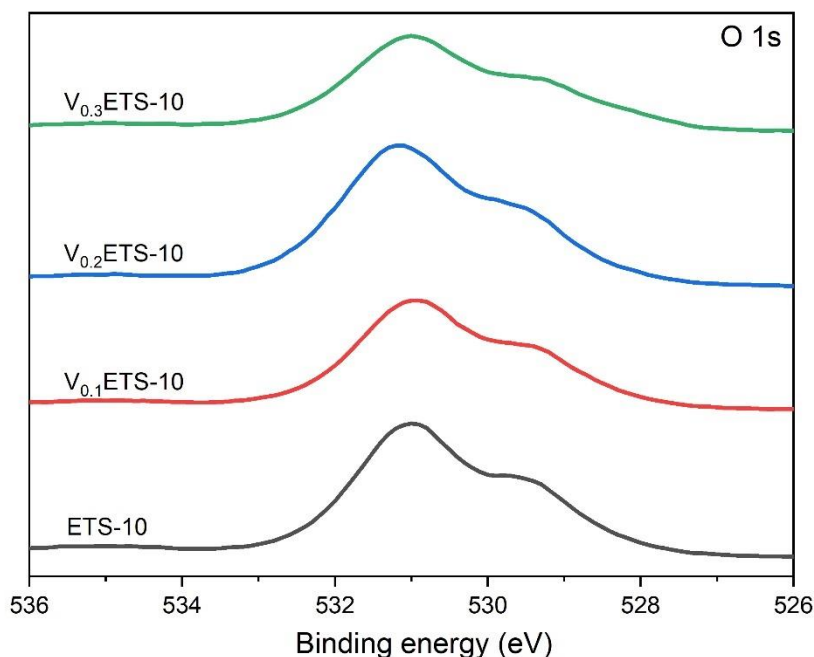


Figure 6.6. XPS spectra of O 1s binding energies of vanadium-substituted ETS-10 samples.

Figure 6.6 shows the XPS spectra of the O 1s region. The wide and asymmetric peak of XPS O 1s indicated that there could be more than one chemical state. Generally, the photoelectron peaks of O 1s could be resolved into three components. The peak at lower BE and lower intensity was assigned to O in Ti-O-Ti linkage (529.6 eV), and the high-intensity peak at a high BE around 531-533 eV was attributed to O in Si-O-Si and Si-O-Ti linkages [111], [112]. As seen in Figure 6.6, V doping led to the O 1s peak shift to the higher binding energy, and peaks were gradually broadened. The shift toward higher energy was reversed for the V<sub>0.3</sub>ETS-10. It may be related to the existing impurities in V<sub>0.3</sub>ETS-10 upon increased V-doping. Moreover, the O 1s peak was broadened upon V doping, indicating some disturbed linkage or the interruption of -Ti-O-Ti-chains by vanadium at some locations.

## 6.2 Humidity Sensing Performances of ETS-10 and its V-doped variations

100 Hz was chosen for the humidity studies as the optimum frequency for impedance vs. relative humidity measurements. Fig 6.7 shows the relationship between the impedance modulus of all sensors and RH at the frequency of 100Hz. Response and recovery time of sensors were measured by the simultaneous change of impedance from the relative humidity of 90 % to 32 % and vice versa.

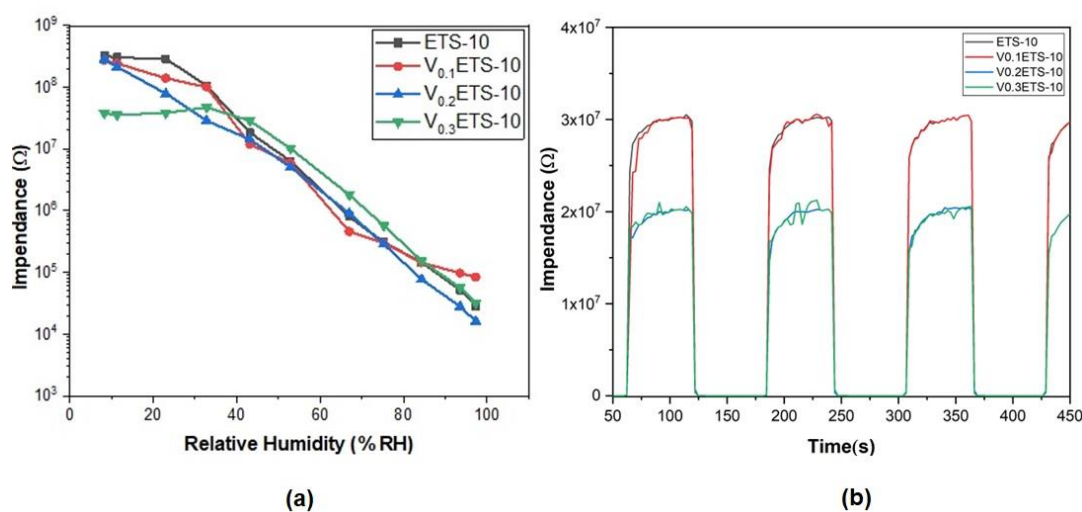


Figure 6.7. Relationship between impedance modulus and RH (a), and response recovery performance of ETS-10 and V-doped ETS-10 sensors at 100Hz frequency (b).

In general, the change in the impedance modulus for all coated films was more than four orders of magnitude within the whole range of RH (8% to 97%) at 100 Hz. The response was less than 8 seconds for all the samples where recovery times were increased from 35 to 41 seconds by increasing the vanadium content. These results suggested that ETS-10 film coated on the quartz glass substrate and its V-doped variations showed good potential for humidity sensing application.

The sensitivity can be obtained from the slope of the Impedance vs. %RH plot. Figure 6.8 represents the sensitivity and linearity of ETS-10 and V-doped ETS-10 sensors for coated films. The results showed that  $V_{0.2}$ ETS-10 showed the highest

potential with optimized linearity since a higher slope in the whole range was obtained for V<sub>0.2</sub>ETS-10. These results indicated that increasing the amount of vanadium increased the sensitivity of the developed sensor as its behavior improved at low RH levels. The other films did not show a particular improvement at low RH levels, leading to lower overall sensitivity. Thus, the vanadium-doped sensors with an optimized vanadium content using ETS-10 films were shown to exhibit great sensitivity for humidity sensing for the first time. The improvement obtained at a low RH level was of particular interest.

This enhancement could be related to the appearance of new states upon doping. It seems that existing Ti<sup>4+</sup> sites in the original ETS-10 structure due to the -Ti-O-Ti- chains were reduced to Ti<sup>3+</sup> due to vanadium incorporation and an optimized amount of doping (V<sub>0.2</sub>ETS-10) resulted in higher electron density which enhanced conductivity [110], [113]. This mechanism was occurring concurrently with the emergence of V<sup>4+</sup> and V<sup>5+</sup> states in the -Ti-O-Ti- chain. Due to the unstable nature of V<sup>5+</sup>, they act as water dissociation sites even at LRH levels (8%-32%). A similar doping mechanism was used to attribute V<sup>5+</sup> sites to make hydroxyl groups (V-OH sites) at the surface for enhanced photocatalytic activity [75]. However, by increasing the amount of vanadium up to the V<sub>0.3</sub>ETS-10 sample, it was observed that the humidity sensing performance decreased at LRH. This insensitivity could be related to the higher amount of V<sup>5+</sup> in the -Ti-O-Ti- chain. Higher V<sup>5+</sup> concentrations caused the appearance of a longer -V<sup>5+</sup>-O-V<sup>5+</sup> chain, which is energetically not favorable and makes the ETS-10 structure unstable [74]. Furthermore, XRD patterns showed impurities like quartz and anatase in the structure of the V<sub>0.3</sub>ETS-10 sample upon increased vanadium doping. These impurities were visible in the SEM images of the V<sub>0.3</sub>ETS-10 sample through the appearance of new cubic-shaped morphologies.

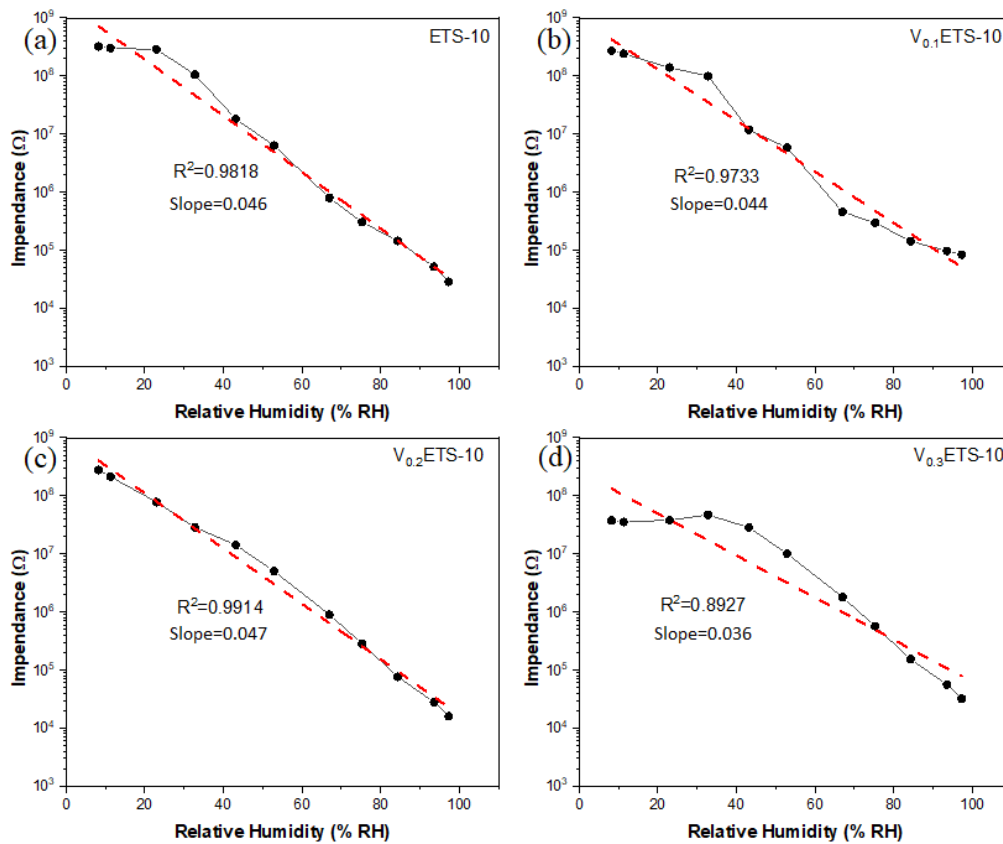


Figure 6.8. Relationship between impedance modulus and RH for all sensors due to their slopes at 100 Hz frequency.

In summary, it seems that vanadium doping in an optimized amount affected the LRH level humidity behavior by hypothetical enhancement of both electronic and ionic conductivity. This type of optimized performance was also observed in photocatalytic studies, where the proximity of the newly created  $\text{Ti}^{3+}$  and  $\text{V}^{5+}$  sites was also of importance. At HRH levels, all films showed similar performance, which was of high sensitivity. So, it can be said that the initial layer of water was significantly affected by the type and number of defects (Ti-OH, V-OH, etc.). Knowing that no single instrument can cover the entire humidity range until now, the developed methodology presented by vanadium-doped ETS-10 films can be a promising solution for LRH detection, which offers a strong alternative for the sensor to cover the whole range.

### 6.3 Complex Impedance Spectra of Spin-coated ETS-10 sensors

The complex impedance spectroscopy (CIS) technique was used on the developed  $V_{0.2}$ ETS-10 humidity sensor in order to elucidate the conduction mechanism at different relative humidity values. These measurements were done by applying a single voltage of 500 mV at a frequency range of 40 Hz-100 kHz. The Nyquist plots for the whole humidity range are presented in Figure 6.9.

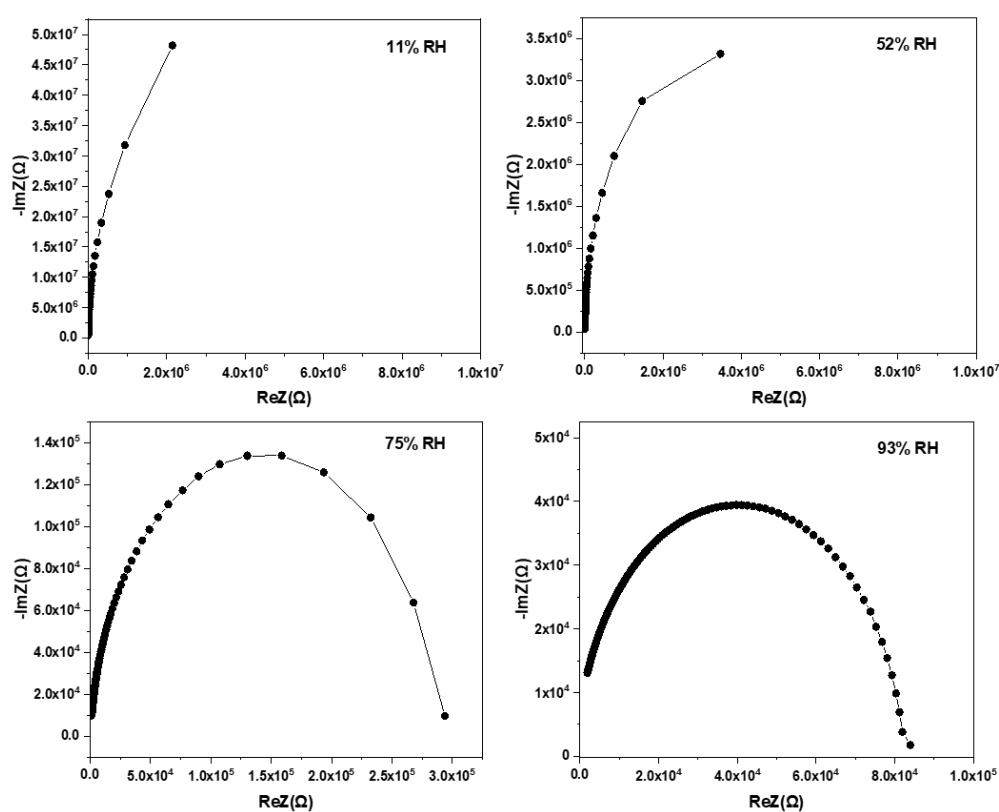


Figure 6.9. Complex impedance spectra of  $V_{0.2}$ ETS-10 at various relative humidity values.

As shown in Figure 6.9-a, when humidity was introduced at a very low RH level (11%), the absence of a continuous water layer resulted in a relatively high impedance with high values of real and imaginary parts, suggesting proton hopping was very low at this stage.

At increased RH values, the semicircle developed into a smaller one, showing a significant decline in impedance. It is possible that at increased RH, physically adsorbed water makes a continuous water layer, which makes proton hopping easier and thus could be observed upon increased conduction with complete semicircles. At increased RH levels, more water molecules could make hydrogen bonds with the hydroxyl groups. The formed chemisorbed water layer could result in  $\text{H}_3\text{O}^+$  hydronium ions, which are more stable than  $\text{H}^+$  ions. At increased RH levels (75%), a continuous water layer is created on the surface, and proton hopping by the hydronium group is enhanced (Figure 6.9-c).

Regarding high RH levels (93.58%), water molecules accumulate on each other, and the proton hopping mechanism increases considerably (Figure 6.9-d). The conductivity thus increases further, causing the resistance to drop further. Less ordered layers on the first physisorbed layer are created due to weak hydrogen bonding. This phenomenon makes the water molecules more mobile to form continuous dipoles through the surface. At high RH levels, the semicircle became smaller, and a short line appeared in the low-frequency range in the semicircular tail. At this stage, physisorbed water molecules move easily, and proton hopping becomes the primary conduction mechanism. This line represents the Warburg impedance in the equivalent circuit. Fig 6.10 shows the equivalent circuit for the sensor at different RH values.

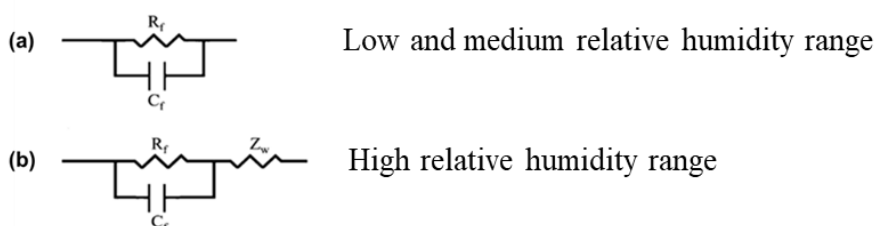


Figure 6.10. Impedance–frequency characteristics of the sensor at different RH levels.  $R_f$ : film resistance;  $C_f$ : film capacitance;  $Z_w$ : Warburg impedance.

#### 6.4 Humidity Sensing Mechanism and effect of vanadium-doping

The presence of dopants was shown to create possible new defect sites for water molecules to dissociate, which could be proposed to be a significant advantage of vanadium doping. When relative humidity was very low, unstable defect sites like  $Ti^{+3}$  and  $V^{+5}$  on the surface of V-doped samples could have an active role in dissociating water molecules to form a hydroxyl group. This layer was chemisorbed, resulting in Ti-OH and V-OH groups promoting the formation of a proton ( $H^+$ ). Thus, the hydroxyl groups could dissociate water molecules and provide mobile protons. These protons give rise to conduction by hopping from site to site on the surface, which results in a proton-hopping mechanism [26].

These results can be interpreted in terms of the electronic and proton conduction mechanism as follows:

The semiconductive nature of the films due to the -Ti-O-Ti- chains could result in mixed-type electronic and ionic conductivity. From the electronic conduction mechanism point of view, at LRH levels, when water molecules were chemisorbed to the film's surface, they donated electrons to the film. In the case of V-doped ETS-10, due to the high electronegativity of  $Ti^{+3}$  compared to  $Ti^{+4}$ , water molecules became more attributed to being adsorbed onto the surface. Moreover, the higher electron density of  $Ti^{+3}$  could enhance electronic conductivity [110], [113].

Electronic conduction mechanism at very low RH levels could also be occurring through the replacement of water molecules with the previously adsorbed oxygens ( $O^-$ ,  $O^{2-}$ , etc.), similar to creating a depletion region on the surface. As a result, the release of the electrons from the ionized oxygen occurred. [30]. Also, it was stated that defect sites result in an increased number of trapped electrons, which were liberated by the adsorption of water molecules [22].

From the ionic conduction mechanism point of view, when water molecules touch the surface of the sensor at low humidity rates, they are attributed to be chemisorbed

on defective sites like  $Ti^{3+}$  and  $V^{5+}$  groups. The dissociation of  $H_2O$  to  $H^+$  and  $OH^-$  ions occurs on the hydroxide groups ( $Ti-OH$ ,  $V-OH$ ) formed upon this chemisorption, and the protons formed during the dissociation hop from one active site to another on the defective surface. This phenomenon is named as Grotthuss mechanism, which determines ionic conductivity [26]. At medium humidity, the conductivity increases by the formation of  $H_3O^+$  instead of protons, causing an increase in surface polarization and proton hopping. This fact is also explained by the Grotthuss ion transfer mechanism, which is defined by the movement of protons in the condensed water layer [26]. In  $H_2O + H_3O^+ = H_3O^+ + H_2O$  ion conduction, a proton separated from  $H_3O^+$  is accepted by the neighboring water molecule, and another proton is released. This mechanism is shown schematically in Fig 6.11.

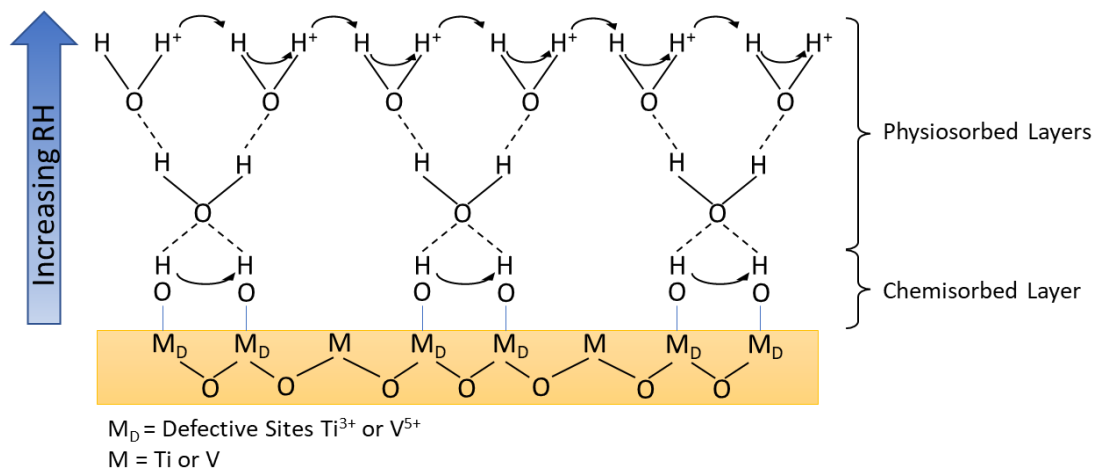


Figure 6.11. The theoretical model for water adsorption on the surface of the sensor.



## SUMMARY AND CONCLUSIONS

The performance of sensors with different film preparation methods and gel formulas obtained throughout this study was summarized in Table 6.1.

Table 6.1 Humidity sensing performance of the films prepared in this study

<b>Sample code</b>	<b>Working range (%)</b>	<b>Response / Recovery times(s)</b>	<b>Sensitivity</b>	<b>Film preparation method</b>
<b>ETS-10-2S</b>	32-97	8/35	> 1000	Spin-coating
<b>AM-6-2S</b>	32-97	54/5	> 1000	
<b>ETS-10-4S</b>	32-97	47/41	> 100	
<b>ETS-10-8S</b>	32-97	68/73	> 100	
<b>2S-TS</b>	43-97	30/80	> 100	Secondary growth (2S)
<b>1D-TS</b>	43-97	250/150	> 100	Secondary growth (1D)
<b>2D-TS</b>	67-97	310/210	> 10	Secondary growth (2D)
<b>2S-VS<sub>1</sub></b>	8-97	50/110	> 10	Secondary growth (2S)
<b>*2S-VS<sub>2</sub></b>	8-97	20/90	> 1000	Secondary growth (2S)
<b>V<sub>0.1</sub> ETS-10</b>	32-97	8/35	> 1000	Spin-coating
<b>*V<sub>0.2</sub> ETS-10</b>	8-97	8/41	> 1000	
<b>V<sub>0.3</sub> ETS-10</b>	32-97	8/40	> 1000	

2S= 2 times spin-coated seed layer, 1/2D=1/2 times dip-coated seed layer

\*Best performing sensors at the whole humidity range.

In this study, the sensing performance of films prepared by the spin-coating method was shown to acquire high sensitivity in the range of (32% - 97%). Doping an optimized level of vanadium to the ETS-10 films, i.e., V<sub>0.2</sub>ETS-10, was the optimized sensor showing enhanced performance at the whole humidity range. As discussed in Chapter 6, this enhancement within the whole range is believed to be related to creating Ti-O-V wires with higher charge transfer and defect groups like Ti<sup>+3</sup> and V<sup>+5</sup> in the film's structure.

The films prepared by spin coating methods had unique information for humidity sensors in the first stage. However, stability is one of the major issues to be resolved for evaluating the performance of humidity sensors. Accordingly, the secondary growth method had to be adapted to achieve more durable and strong film formation for humidity sensors.

It was seen that the humidity sensing performance of secondary growth films of ETS-10 showed good sensitivity in the high relative humidity range. Attempts towards increasing the sensing performance at the whole range were investigated by tailoring the CPO values towards *c*-orientation. Decreasing the CPO values was aspired by changing the ETS-10 seed layer coating method from spin-coating to dip-coating. However, no significant change in humidity sensing performance was observed by manipulating the seed layer coating method.

Within the scope of secondary growth film studies prepared with vanadium sources, both the effect of different vanadium sources on film formation and the sensing performance differences of AM-6 films compared to ETS-10 films were evaluated.

Among the sensors prepared by the secondary growth method, 2S-VS<sub>2</sub> showed the best humidity sensing performance, as shown in Table 6.1. The higher amount of defects proposed to be forming in 2S-VS<sub>2</sub> suggests that the applied synthesis conditions with varying parameters allowed one to obtain ETS-10/AM-6 core-shell films with controllably tailored defect concentration. It was discussed that the 2S-VS<sub>2</sub> films also induced the formation of Ti-O-V wires. Moreover, all obtained results correlated with the lower CPO values compared to 2S-VS<sub>1</sub> values obtained for this sample.

In summary, this study shows that microporous ETS-10/AM-6 with a core-shell-like structure tailored at optimized chemical and film preparation formulation are strong alternatives in humidity sensing applications due to their high sensitivity at the whole relative humidity range. Although there is still room for enhancing the overall performance, this thesis is believed to have brought some critical points toward pursuing nanoporous materials in novel sensing platforms.

## REFERENCES

- [1] H. Farahani, R. Wagiran, and M. N. Hamidon, *Humidity sensors principle, mechanism, and fabrication technologies: A comprehensive review*, vol. 14, no. 5. 2014. doi: 10.3390/s140507881.
- [2] Z. Chen and C. Lu, ‘Humidity sensors: A review of materials and mechanisms’, *Sens Lett*, vol. 3, no. 4, pp. 274–295, 2005, doi: 10.1166/sl.2005.045.
- [3] D. Nunes *et al.*, ‘Metal oxide nanostructures for sensor applications’, *Semiconductor Science and Technology*, vol. 34, no. 4. Institute of Physics Publishing, Mar. 11, 2019. doi: 10.1088/1361-6641/ab011e.
- [4] L. Sun, A. A. Haidry, Q. Fatima, Z. Li, and Z. Yao, ‘Improving the humidity sensing below 30% RH of TiO<sub>2</sub> with GO modification’, *Mater Res Bull*, vol. 99, pp. 124–131, Mar. 2018, doi: 10.1016/j.materresbull.2017.11.001.
- [5] R. Grau-Crespo and U. Schwingenschlögl, ‘The interplay between dopants and oxygen vacancies in the magnetism of V-doped TiO<sub>2</sub>’, *Journal of Physics Condensed Matter*, vol. 23, no. 33, Aug. 2011, doi: 10.1088/0953-8984/23/33/334216.
- [6] M. Gong, Y. Li, Y. Guo, X. Lv, and X. Dou, ‘2D TiO<sub>2</sub> nanosheets for ultrasensitive humidity sensing application benefited by abundant surface oxygen vacancy defects’, *Sens Actuators B Chem*, vol. 262, pp. 350–358, Jun. 2018, doi: 10.1016/j.snb.2018.01.187.
- [7] M. Z. Musa *et al.*, ‘Humidity Sensing Performance of V: TiO<sub>2</sub> 3D Nanostructure-based Humidity Sensor’, in *IOP Conference Series: Earth and Environmental Science*, Feb. 2021, vol. 682, no. 1. doi: 10.1088/1755-1315/682/1/012073.

- [8] ‘Enhanced Sensitivity of Humidity Sensor Prepared using Vertically Aligned V-doped TiO<sub>2</sub>Nanorods Array’.
- [9] N. C. Jeong, M. H. Lee, and K. B. Yoon, ‘Length-dependent band-gap shift of TiO<sub>3</sub>- molecular wires embedded in zeolite ETS-10’, *Angewandte Chemie - International Edition*, vol. 46, no. 31, pp. 5868–5872, 2007, doi: 10.1002/anie.200701676.
- [10] C. J. Nak *et al.*, ‘New insights into ETS-10 and titanate quantum wire: A comprehensive characterization’, *J Am Chem Soc*, vol. 131, no. 36, pp. 13080–13092, Sep. 2009, doi: 10.1021/ja903638v.
- [11] M. Guo *et al.*, ‘“Extracting” the key fragment in ETS-10 crystallization and its application in AM-6 assembly’, *Chemistry - A European Journal*, vol. 18, no. 38, pp. 12078–12084, Sep. 2012, doi: 10.1002/chem.201200875.
- [12] J. Rocha, P. Branddo, Z. Lin, M. W. Anderson, and V. Alfredsson, ‘The First Large-Pore Vanadosilicate Framework Containing Hexacoordinated Vanadium’, pp. 100–102, 1997.
- [13] E. Traversa, ‘Ceramic sensors for humidity detection: the state-of-the-art and future developments’, *Sens Actuators B Chem*, vol. 23, no. 2–3, pp. 135–156, 1995, doi: 10.1016/0925-4005(94)01268-M.
- [14] E. Traversa, Y. Sadaoka, M. C. Carotta, and G. Martinelli, ‘Environmental monitoring field tests using screen-printed thick-film sensors based on semiconducting oxides’, 2000. [Online]. Available: [www.elsevier.nl/locatersensorb](http://www.elsevier.nl/locatersensorb)
- [15] G. v Kunte, S. A. Shivashankar, and A. M. Umarji, ‘Humidity sensing characteristics of hydrotungstite thin films’, 2008.
- [16] A. v. Mamishev, K. Sundara-Rajan, F. Yang, Y. Du, and M. Zahn, ‘Interdigital sensors and transducers’, in *Proceedings of the IEEE*, 2004, vol. 92, no. 5, pp. 808–844. doi: 10.1109/JPROC.2004.826603.

- [17] W.-P. Tai, J.-G. Kim, J.-H. Oh, and C. Lee, 'Humidity sensing properties of nanostructured-bilayered potassium tantalate: Titania films'.
- [18] A. S. G. Reddy, B. B. Narakathu, M. Z. Atashbar, M. Rebros, E. Rebrosova, and M. K. Joyce, 'Fully printed flexible humidity sensor', in *Procedia Engineering*, 2011, vol. 25, pp. 120–123. doi: 10.1016/j.proeng.2011.12.030.
- [19] Z. Ahmad, Q. Zafar, K. Sulaiman, R. Akram, and K. S. Karimov, 'A humidity sensing organic-inorganic composite for environmental monitoring', *Sensors (Switzerland)*, vol. 13, no. 3, pp. 3615–3624, Mar. 2013, doi: 10.3390/s130303615.
- [20] R. Fenner and E. Zdankiewicz, 'Micromachined Water Vapor Sensors: A Review of Sensing Technologies', *IEEE Sens J*, vol. 1, no. 4, pp. 309–317, 2001, doi: 10.1109/7361.983470.
- [21] A. Tripathy, S. Pramanik, J. Cho, J. Santhosh, and N. A. A. Osman, 'Role of morphological structure, doping, and coating of different materials in the sensing characteristics of humidity sensors', *Sensors (Switzerland)*, vol. 14, no. 9. MDPI AG, pp. 16343–16422, Sep. 03, 2014. doi: 10.3390/s140916343.
- [22] T. A. Blank, L. P. Eksperiandova, and K. N. Belikov, 'Recent trends of ceramic humidity sensors development: A review', *Sens Actuators B Chem*, vol. 228, pp. 416–442, 2016, doi: 10.1016/j.snb.2016.01.015.
- [23] A. Lasia, 'Electrochemical Impedance Spectroscopy and its Applications', in *Modern Aspects of Electrochemistry*, Kluwer Academic Publishers, 2005, pp. 143–248. doi: 10.1007/0-306-46916-2\_2.
- [24] D. V. RIBEIRO, C. A. C. SOUZA, and J. C. C. ABRANTES, 'Use of Electrochemical Impedance Spectroscopy (EIS) to monitoring the corrosion of reinforced concrete', *Revista IBRACON de Estruturas e Materiais*, vol. 8, no. 4, pp. 529–546, Aug. 2015, doi: 10.1590/s1983-41952015000400007.

- [25] R. A. Huggins, 'Simple Method to Determine Electronic Conductivity in Mixed A Review and Ionic Components of the Conductors', 2002.
- [26] N. Agmon, 'The Grotthuss mechanism', *Chem Phys Lett*, vol. 244, no. 5–6, pp. 456–462, 1995, doi: 10.1016/0009-2614(95)00905-J.
- [27] P. A. Thiel and T. E. Madey, 'THE INTERACTION OF WATER WITH SOLID SURFACES: FUNDAMENTAL ASPECTS', 1987.
- [28] S. J. Ray, 'Humidity sensor using a single molecular transistor', *J Appl Phys*, vol. 118, no. 4, Jul. 2015, doi: 10.1063/1.4927296.
- [29] J. F. Boyle and K. A. Jones, 'THE EFFECTS OF CO, WATER VAPOR AND SURFACE TEMPERATURE ON THE CONDUCTIVITY OF A SnO<sub>2</sub> GAS SENSOR'.
- [30] N. Yamazoe, J. Fuchigami, M. Kishikawa, and T. Seiyama, 'INTERACTIONS OF TIN OXIDE SURFACE WITH O<sub>2</sub>, H<sub>2</sub>O AND H<sub>2</sub>', 1979.
- [31] V. Galstyan, 'Porous TiO<sub>2</sub>-based gas sensors for cyber chemical systems to provide security and medical diagnosis', *Sensors (Switzerland)*, vol. 17, no. 12. MDPI AG, Dec. 19, 2017. doi: 10.3390/s17122947.
- [32] M. Gong, Y. Li, Y. Guo, X. Lv, and X. Dou, '2D TiO<sub>2</sub> nanosheets for ultrasensitive humidity sensing application benefited by abundant surface oxygen vacancy defects', *Sens Actuators B Chem*, vol. 262, pp. 350–358, Jun. 2018, doi: 10.1016/j.snb.2018.01.187.
- [33] E. A. Sosnov, A. A. Malkov, and A. A. Malygin, 'Hydrolytic stability of the Si–O–Ti bonds in the chemical assembly of titania nanostructures on silica surfaces', *Russian Chemical Reviews*, vol. 79, no. 10, pp. 907–920, Dec. 2010, doi: 10.1070/rc2010v079n10abeh004112.

- [34] S. P. Mirajkar, A. Thangaraj, and V. P. Shiralkar, 'Sorption Properties of Titanium Silicate Molecular Sieves 3073', 1992. [Online]. Available: <https://pubs.acs.org/sharingguidelines>
- [35] H. van Bekkum, E. M. Flanigen, P. A. Jacobs, and J. C. Jansen, 'Introduction to zeolite science and practice: Preface 2nd edition', *Stud Surf Sci Catal*, vol. 137, 2001, doi: 10.1016/s0167-2991(01)80240-8.
- [36] S. E. Sen, S. M. Smith, and K. A. Sullivan, 'Tetrahedron report number 508 Organic Transformations using Zeolites and Zeotype Materials', *Tetrahedron*, vol. 55, pp. 12657–12698, 1999.
- [37] C. C. H. Lin, K. A. Dambrowitz, and S. M. Kuznicki, 'Evolving applications of zeolite molecular sieves', *Can J Chem Eng*, vol. 90, no. 2, pp. 207–216, Apr. 2012, doi: 10.1002/CJCE.20667.
- [38] Steven M. Kuznicki, 'Large-pored crystalline titanium molecular sieve zeolites', 4,853,202, Aug. 01, 1989
- [39] L. Lv, F. Su, and X. S. Zhao, 'A reinforced study on the synthesis of microporous titanosilicate ETS-10', *Microporous and Mesoporous Materials*, vol. 76, no. 1–3, pp. 113–122, 2004, doi: 10.1016/j.micromeso.2004.08.004.
- [40] N. B. K. Magnowski, A. M. Avila, C. C. H. Lin, M. Shi, and S. M. Kuznicki, 'Extraction of ethane from natural gas by adsorption on modified ETS-10', *Chem Eng Sci*, vol. 66, no. 8, pp. 1697–1701, Apr. 2011, doi: 10.1016/j.ces.2011.01.005.
- [41] Z. Ji, J. Warzywoda, and A. Sacco, 'Titanosilicate ETS-10 thin film preparation on fused silica optical fibers', *Microporous and Mesoporous Materials*, vol. 101, no. 1-2 SPEC. ISS., pp. 279–287, 2007, doi: 10.1016/j.micromeso.2006.10.003.
- [42] Z. Ji, B. Yilmaz, J. Warzywoda, and A. Sacco, 'Hydrothermal synthesis of titanosilicate ETS-10 using  $Ti(SO_4)_2$ ', *Microporous and Mesoporous*

- Materials*, vol. 81, no. 1–3, pp. 1–10, 2005, doi: 10.1016/j.micromeso.2005.01.006.
- [43] Z. Ji, J. Warzywoda, and A. Sacco, ‘Synthesis and morphological control of large titanosilicate ETS-10 crystals’, *Microporous and Mesoporous Materials*, vol. 109, no. 1–3, pp. 1–11, 2008, doi: 10.1016/j.micromeso.2007.04.019.
- [44] P. D. Southon and R. F. Howe, ‘Spectroscopic studies of disorder in the microporous titanosilicate ETS-10’, *Chemistry of Materials*, vol. 14, no. 10, pp. 4209–4218, Oct. 2002, doi: 10.1021/cm021199c.
- [45] H. Karge *et al.*, ‘Structure of the Microporous Titanosilicate ETS-10’.
- [46] M. N. Ismail, U. K. Ibe, T. Chernenko, M. Diem, J. Warzywoda, and A. Sacco, ‘Synthesis and characterization of vanadosilicate AM-6 with transition metal ions isomorphously substituted in the framework’, *Microporous and Mesoporous Materials*, vol. 145, no. 1–3, pp. 118–123, Nov. 2011, doi: 10.1016/j.micromeso.2011.04.030.
- [47] M. N. Ismail *et al.*, ‘First unseeded hydrothermal synthesis of microporous vanadosilicate AM-6’, *Microporous and Mesoporous Materials*, vol. 120, no. 3, pp. 454–459, 2009, doi: 10.1016/j.micromeso.2008.12.020.
- [48] R. M. Yeates *et al.*, ‘AM-6: A microporous one-dimensional ferromagnet’, *Dalton Transactions*, no. 38, pp. 8025–8032, 2009, doi: 10.1039/b908099f.
- [49] S. J. Datta and K. B. Yoon, ‘Synthesis of ideal AM-6 and elucidation of v4+-to-O charge transfer in vanadate quantum wires’, *Angewandte Chemie - International Edition*, vol. 49, no. 29, pp. 4971–4975, Jul. 2010, doi: 10.1002/anie.200907088.
- [50] F. Mani, L. Wu, and S. M. Kuznicki, ‘A simplified method to synthesize pure vanadium silicate analogue of ETS-10’, *Microporous and Mesoporous Materials*, vol. 177, pp. 91–96, 2013, doi: 10.1016/j.micromeso.2013.02.008.



- [51] A. Kumar, G. Gupta, K. Bapna, and D. D. Shivagan, ‘Semiconductor-metal-oxide-based nano-composites for humidity sensing applications’, *Materials Research Bulletin*, vol. 158. Elsevier Ltd, Feb. 01, 2023. doi: 10.1016/j.materresbull.2022.112053.
- [52] M. O. S. V. M. and R. M.Z.Musa, ‘Enhanced Sensitivity of Humidity Sensor Prepared using Vertically Aligned V-doped TiO<sub>2</sub>Nanorods Array’, *JOURNAL OF ELECTRICAL AND ELECTRONIC SYSTEMS RESEARCH*, pp. 68–73, 2020.
- [53] A. H. Zare and S. Mohammadi, ‘Silver doped titanium dioxide humidity sensor’, in *IOP Conference Series: Materials Science and Engineering*, 2011, vol. 17, no. 1. doi: 10.1088/1757-899X/17/1/012015.
- [54] A. I. Buvailo, Y. Xing, J. Hines, N. Dollahon, and E. Borguet, ‘TiO<sub>2</sub>/LiCl-based nanostructured thin film for humidity sensor applications’, *ACS Appl Mater Interfaces*, vol. 3, no. 2, pp. 528–533, Feb. 2011, doi: 10.1021/am1011035.
- [55] H. Jyothilal, G. Shukla, S. Walia, S. Kundu, and S. Angappane, ‘Humidity sensing and breath analyzing applications of TiO<sub>2</sub> slanted nanorod arrays’, *Sens Actuators A Phys*, vol. 301, Jan. 2020, doi: 10.1016/j.sna.2019.111758.
- [56] Y. Hase *et al.*, ‘Humidity sensor properties of hydrothermally grown rutile-TiO<sub>2</sub> microspheres on interdigital electrodes (IDEs)’, *Journal of Materials Science: Materials in Electronics*, vol. 33, no. 15, pp. 11825–11840, May 2022, doi: 10.1007/s10854-022-08146-4.
- [57] E. P. Ng and S. Mintova, ‘Nanoporous materials with enhanced hydrophilicity and high water sorption capacity’, *Microporous and Mesoporous Materials*, vol. 114, no. 1–3. Elsevier, pp. 1–26, Sep. 01, 2008. doi: 10.1016/j.micromeso.2007.12.022.

- [58] A. Jentys, G. Warecka, M. Derewinski, and J. A. Lercher, ‘Adsorption of Water on ZSM5 Zeolites’, 1989. [Online]. Available: <https://pubs.acs.org/sharingguidelines>
- [59] D. H. Olson, W. O. Haag, and W. S. Borghard, ‘Use of water as a probe of zeolitic properties: interaction of water with HZSM-5’, 2000. [Online]. Available: [www.elsevier.nl/locate/micromeso](http://www.elsevier.nl/locate/micromeso)
- [60] J. Kornatowski, ‘Adsorption isotherms of water as a tool for characterization of metal substituted aluminophosphate molecular sieves’, *Comptes Rendus Chimie*, vol. 8, no. 3–4, pp. 561–568, 2005, doi: 10.1016/j.crci.2004.12.007.
- [61] N. Li *et al.*, ‘Host-guest composite materials of LiCl/NaY with wide range of humidity sensitivity’, *Mater Lett*, vol. 58, no. 10, pp. 1535–1539, Apr. 2004, doi: 10.1016/j.matlet.2003.10.022.
- [62] S. Mintova and T. Bein, ‘Nanosized zeolite films for vapor-sensing applications’, *Microporous and Mesoporous Materials*, vol. 50, no. 2–3, pp. 159–166, 2001, doi: 10.1016/S1387-1811(01)00443-7.
- [63] S. Mintova, S. Mo, and T. Bein, ‘Humidity sensing with ultrathin LTA-type molecular sieve films grown on piezoelectric devices’, *Chemistry of Materials*, vol. 13, no. 3, pp. 901–905, 2001, doi: 10.1021/cm000671w.
- [64] W. Zhang, R. Wang, Q. Zhang, and J. Li, ‘Humidity sensitive properties of K-doped mesoporous silica SBA-15’, *Journal of Physics and Chemistry of Solids*, vol. 73, no. 4, pp. 517–522, Apr. 2012, doi: 10.1016/j.jpics.2011.10.030.
- [65] S. Kunchakara, A. Ratan, M. Dutt, J. Shah, R. K. Kotnala, and V. Singh, ‘Impedimetric humidity sensing studies of Ag doped MCM-41 mesoporous silica coated on silver sputtered interdigitated electrodes’, *Journal of Physics and Chemistry of Solids*, vol. 145, Oct. 2020, doi: 10.1016/j.jpics.2020.109531.

- [66] Y. Chen *et al.*, ‘Humidity sensor based on AlPO<sub>4</sub>-5 zeolite with high responsivity and its sensing mechanism’, *Sens Actuators B Chem*, vol. 212, pp. 242–247, 2015, doi: 10.1016/j.snb.2015.02.017.
- [67] G. P. Alcantara, L. E. B. Ribeiro, A. F. Alves, C. M. G. Andrade, and F. Fruett, ‘Humidity sensor based on zeolite for application under environmental conditions’, *Microporous and Mesoporous Materials*, vol. 247, pp. 38–45, 2017, doi: 10.1016/j.micromeso.2017.03.042.
- [68] X. Yang and R. E. Truitt, ‘Xe NMR Investigation of ETS-10 Titanosilicate Molecular Sieves’, 1995. [Online]. Available: <https://pubs.acs.org/sharingguidelines>
- [69] J. M. Pinheiro, A. A. Valente, S. Salústio, N. Ferreira, J. Rocha, and C. M. Silva, ‘Application of the novel ETS-10/water pair in cyclic adsorption heating processes: Measurement of equilibrium and kinetics properties and simulation studies’, *Appl Therm Eng*, vol. 87, pp. 412–423, Jun. 2015, doi: 10.1016/j.applthermaleng.2015.05.011.
- [70] Z. Ji, ‘SYNTHESIS AND ENGINEERING OF TITANOSILICATE ETS-10 FOR ENHANCED PHOTOCATALYTIC ACTIVITY IN AN OPTICAL FIBER REACTOR’, PhD Thesis, Northeastern University, 2009.
- [71] L. Lv, F. Y. Lee, J. Zhou, F. Su, and X. S. Zhao, ‘XPS study on microporous titanosilicate ETS-10 upon acid treatment’, *Microporous and Mesoporous Materials*, vol. 96, no. 1–3, pp. 270–275, Nov. 2006, doi: 10.1016/j.micromeso.2006.07.006.
- [72] Z. Ji, M. N. Ismail, D. M. Callahan, J. Warzywoda, and A. Sacco, ‘Transition metal ion substitution in titanosilicate ETS-10 for enhanced UV light photodegradation of methylene blue’, *J Photochem Photobiol A Chem*, vol. 221, no. 1, pp. 77–83, Jun. 2011, doi: 10.1016/j.jphotochem.2011.04.027.
- [73] P. Brandão, A. Philippou, A. Valente, J. Rocha, and M. Anderson, ‘Synthesis and characterisation of chromium-substituted ETS-10’, *Physical Chemistry*

- Chemical Physics*, vol. 3, no. 9, pp. 1773–1777, 2001, doi: 10.1039/b006828o.
- [74] A. M. Shough, D. J. Doren, M. Nash, and R. F. Lobo, ‘Effects of vanadium substitution on the structure and photocatalytic behavior of ETS-10’, *Journal of Physical Chemistry C*, vol. 111, no. 4, pp. 1776–1782, Feb. 2007, doi: 10.1021/jp0662247.
- [75] M. J. Nash, S. Rykov, R. F. Lobo, D. J. Doren, and I. Wachs, ‘Photocatalytic Activity of Vanadium-Substituted ETS-10’, 2007, doi: 10.1021/jp067259.
- [76] A. Marie Shough, R. F. Lobo, and D. J. Doren, ‘A visible light photocatalyst: Effects of vanadium substitution on ETS-10’, *Physical Chemistry Chemical Physics*, vol. 9, no. 37, pp. 5096–5104, 2007, doi: 10.1039/b703187d.
- [77] M. Guo, G. Li, F. Fan, Z. Feng, and C. Li, ‘Enhancement of the visible light absorption intensity of microporous vanadosilicate AM-6’, *Chemical Communications*, vol. 48, no. 97, pp. 11892–11894, Nov. 2012, doi: 10.1039/c2cc36083g.
- [78] S. Galioglu, M. N. Ismail, J. Warzywoda, A. Sacco, and B. Akata, ‘Preparation and microstructural characterization of oriented titanosilicate ETS-10 thin films on indium tin oxide surfaces’, *Microporous and Mesoporous Materials*, vol. 131, pp. 401–406, 2010, doi: 10.1016/j.micromeso.2010.02.001.
- [79] D. Kuzyaka, S. Galioglu, and B. Akata, ‘Secondary growth of microporous vanadosilicate AM-6 films’, *Journal of Porous Materials*, vol. 23, no. 5, pp. 1–9, 2016, doi: 10.1007/s10934-016-0191-2.
- [80] Y. Liu, Y. Li, and W. Yang, ‘Effective manipulation of the microstructure of zeolite film by hydrothermal pretreatment’, *J Mater Sci*, vol. 46, no. 11, pp. 3942–3951, Jun. 2011, doi: 10.1007/s10853-011-5319-9.

- [81] F. Ying, R. W. Smith, and D. J. Srolovitz, 'The mechanism of texture formation during film growth: The roles of preferential sputtering and shadowing', *Appl Phys Lett*, vol. 69, no. 20, pp. 3007–3009, Nov. 1996, doi: 10.1063/1.116821.
- [82] Z. Wang and Y. Yan, 'Oriented zeolite MFI monolayer films on metal substrates by in situ crystallization'. [Online]. Available: [www.elsevier.com/locate/micromeso](http://www.elsevier.com/locate/micromeso)
- [83] B. Yilmaz, K. G. Shattuck, J. Warzywoda, and A. Sacco, 'Controlling crystal orientation in microporous titanosilicate ETS-4 films by secondary growth method', *J Mater Sci*, vol. 41, no. 10, pp. 3135–3138, May 2006, doi: 10.1007/s10853-006-6453-7.
- [84] J. S. Lee, H. K. Jae, J. L. Young, C. J. Nak, and B. Y. Kyung, 'Manual assembly of microcrystal monolayers on substrates', *Angewandte Chemie - International Edition*, vol. 46, no. 17, pp. 3087–3090, 2007, doi: 10.1002/anie.200604367.
- [85] Z. Lin, J. Rocha, A. Navajas, C. Téllez, J. Coronas, and J. Santamaría, 'Synthesis and characterisation of titanosilicate ETS-10 membranes', *Microporous and Mesoporous Materials*, vol. 67, no. 1, pp. 79–86, Jan. 2004, doi: 10.1016/j.micromeso.2003.10.004.
- [86] F. Qiu, X. Wang, X. Zhang, H. Liu, S. Liu, and K. L. Yeung, 'Preparation and properties of TS-1 zeolite and film using Sil-1 nanoparticles as seeds', *Chemical Engineering Journal*, vol. 147, no. 2–3, pp. 316–322, Apr. 2009, doi: 10.1016/j.cej.2008.11.034.
- [87] X. Zhang, H. Liu, and K. L. Yeung, 'Influence of seed size on the formation and microstructure of zeolite silicalite-1 membranes by seeded growth', *Mater Chem Phys*, vol. 96, no. 1, pp. 42–50, Mar. 2006, doi: 10.1016/j.matchemphys.2005.06.031.

- [88] J. Li *et al.*, ‘Silicalite-1 zeolite membrane: Synthesis by seed method and application in organics removal’, *Chemosphere*, vol. 218, pp. 984–991, Mar. 2019, doi: 10.1016/j.chemosphere.2018.11.215.
- [89] J. Hedlund, S. Mintova, and J. Sterte, ‘Controlling the preferred orientation in silicalite-1 films synthesized by seeding’, 1999.
- [90] W. C. Wong, L. Tak, Y. Au, C. T. Ariso, and K. L. Yeung, ‘Effects of synthesis parameters on the zeolite membrane growth’, 2001.
- [91] G. Xomeritakis *et al.*, ‘Growth, microstructure, and permeation properties of supported zeolite (MFI) films and membranes prepared by secondary growth’, 1999.
- [92] D. Kuzyaka, ‘MICROPOROUS VANADOSILICATE AM-6 FILMS FOR PHOTOCATALYTIC APPLICATIONS’, PhD Thesis, Middle East Technical University, 2019.
- [93] S. Galioglu, ‘SYNTHESIS AND CHARACTERIZATION OF TITANOSILICATE ETS-10 FOR POTENTIAL PHOTOVOLTAIC APPLICATIONS’, PhD Thesis, Middle East Technical University, 2010.
- [94] D. Kuzyaka, S. Galioglu, and B. Akata, ‘Secondary growth of microporous vanadosilicate AM-6 films’, *Journal of Porous Materials*, vol. 23, no. 5, pp. 1319–1327, Oct. 2016, doi: 10.1007/s10934-016-0191-2.
- [95] S. J. Datta and K. B. Yoon, ‘Synthesis of ideal AM-6 and elucidation of v4+-to-O charge transfer in vanadate quantum wires’, *Angewandte Chemie - International Edition*, vol. 49, no. 29, pp. 4971–4975, 2010, doi: 10.1002/anie.200907088.
- [96] C. C. Pavel, B. Zibrowius, E. Löffler, and W. Schmidt, ‘On the influence of ion exchange on the local structure of the titanosilicate ETS-10’, *Physical Chemistry Chemical Physics*, vol. 9, no. 26, pp. 3440–3446, Jun. 2007, doi: 10.1039/b701773a.

- [97] Y. Su, M. lou Balmer, and B. C. Bunker, 'Raman spectroscopic studies of silicotitanates', *Journal of Physical Chemistry B*, vol. 104, no. 34, pp. 8160–8169, Aug. 2000, doi: 10.1021/jp0018807.
- [98] L. Lv, J. K. Zhou, F. Su, and X. S. Zhao, 'Local structure changes of microporous titanosilicate ETS-10 upon acid treatment', *Journal of Physical Chemistry C*, vol. 111, no. 2, pp. 773–778, Jan. 2007, doi: 10.1021/jp056107w.
- [99] M. N. Ismail, U. K. Ibe, T. Chernenko, M. Diem, J. Warzywoda, and A. Sacco, 'Synthesis and characterization of vanadosilicate AM-6 with transition metal ions isomorphously substituted in the framework', *Microporous and Mesoporous Materials*, vol. 145, no. 1–3, pp. 118–123, 2011, doi: 10.1016/j.micromeso.2011.04.030.
- [100] L. Sun, A. A. Haidry, Q. Fatima, Z. Li, and Z. Yao, 'Improving the humidity sensing below 30% RH of TiO<sub>2</sub> with GO modification', *Mater Res Bull*, vol. 99, pp. 124–131, Mar. 2018, doi: 10.1016/j.materresbull.2017.11.001.
- [101] S. Galioğlu, M. N. Ismail, J. Warzywoda, A. Sacco, and B. Akata, 'Preparation and microstructural characterization of oriented titanosilicate ETS-10 thin films on indium tin oxide surfaces', *Microporous and Mesoporous Materials*, vol. 131, no. 1–3, pp. 401–406, 2010, doi: 10.1016/j.micromeso.2010.02.001.
- [102] W. C. Wong, L. T. Y. Au, C. T. Ariso, and K. L. Yeung, 'Effects of synthesis parameters on the zeolite membrane growth', *J Memb Sci*, vol. 191, no. 1–2, pp. 143–163, 2001, doi: 10.1016/S0376-7388(01)00453-7.
- [103] H. K. Jeong, J. Krohn, K. Sujaoti, and M. Tsapatsis, 'Oriented molecular sieve membranes by heteroepitaxial growth', *J Am Chem Soc*, vol. 124, no. 44, pp. 12966–12968, Nov. 2002, doi: 10.1021/ja020947w.
- [104] J. Rocha, P. Brandão, Z. Lin, M. W. Anderson, V. Alfredsson, and O. Terasaki, 'The First Large-Pore Vanadosilicate Framework Containing

- Hexacoordinated Vanadium’, *Angewandte Chemie International Edition in English*, vol. 36, no. 1–2, pp. 100–102, 1997, doi: 10.1002/anie.199701001.
- [105] S. J. Datta and K. B. Yoon, ‘Synthesis of pure VSH-2 in large quantities and its characterization’, in *Topics in Catalysis*, Dec. 2010, vol. 53, no. 19–20, pp. 1311–1318. doi: 10.1007/s11244-010-9589-2.
- [106] M. Guo *et al.*, ‘“Extracting” the key fragment in ETS-10 crystallization and its application in AM-6 assembly’, *Chemistry - A European Journal*, vol. 18, no. 38, pp. 12078–12084, 2012, doi: 10.1002/chem.201200875.
- [107] J. H. Yu, S. H. Nam, J. W. Lee, D. I. Kim, and J. H. Boo, ‘Oxidation state and structural studies of vanadium-doped titania particles for the visible light-driven photocatalytic activity’, *Appl Surf Sci*, vol. 472, pp. 46–53, Apr. 2019, doi: 10.1016/j.apsusc.2018.04.125.
- [108] Y. Wang and D. J. Doren, ‘Electronic structures of V-doped anatase TiO<sub>2</sub>’, *Solid State Commun*, vol. 136, no. 3, pp. 142–146, 2005, doi: 10.1016/j.ssc.2005.07.014.
- [109] H. Liu, F. Shen, M. Xing, J. Zhang, and M. Anpo, ‘Synthesis, characterization and photo-activity of vacuum activated V 4+ and Ti3+ doped TiO<sub>2</sub>’, *Catal Letters*, vol. 144, no. 9, pp. 1494–1498, 2014, doi: 10.1007/s10562-014-1308-3.
- [110] T. Song, S. Ye, H. Liu, and Y. G. Wang, ‘Self-doping of Ti<sup>3+</sup> into Na<sub>2</sub>Ti<sub>3</sub>O<sub>7</sub> increases both ion and electron conductivity as a high-performance anode material for sodium-ion batteries’, *J Alloys Compd*, vol. 767, pp. 820–828, Oct. 2018, doi: 10.1016/j.jallcom.2018.07.186.
- [111] I. Tiscornia, S. Irusta, P. Prádanos, C. Téllez, J. Coronas, and J. Santamaría, ‘Preparation and characterization of titanosilicate Ag-ETS-10 for propylene and propane adsorption’, *Journal of Physical Chemistry C*, vol. 111, no. 12, pp. 4702–4709, Mar. 2007, doi: 10.1021/jp070044v.



- [112] S. B. Waghmode, R. Vetrivel, S. G. Hegde, C. S. Gopinath, and S. Sivasanker, 'Physicochemical investigations of the basicity of the cation exchanged ETS-10 molecular sieves', *Journal of Physical Chemistry B*, vol. 107, no. 33, pp. 8517–8523, Aug. 2003, doi: 10.1021/jp0278622.
- [113] G. Yang and S. J. Park, 'The formation mechanism of  $\text{Li}_4\text{Ti}_5\text{O}_{12-y}$  solid solutions prepared by carbothermal reduction and the effect of  $\text{Ti}^{3+}$  on electrochemical performance', *Sci Rep*, vol. 9, no. 1, Dec. 2019, doi: 10.1038/s41598-019-41206-0.



## CURRICULUM VITAE

Surname, Name: Davoudnezhad, Ramona

Nationality: Iranian, Turkish

Date and Place of Birth: 2 January 1990, Tabriz

### EDUCATION

Degree	Institution	Year of Graduation
MS	METU Metallurgy Engineering and Material Science	2016
BS	Sahand University of technology	2012

### WORK EXPERIENCE

Year	Place	Enrollment
2022 - present	Kalyon Güneş Teknolojileri Üretim A.Ş, Ankara	R & D Engineer
2018-2022	METU-MNT Department	TÜBİTAK Project Scholar

### FOREIGN LANGUAGES

Advanced English, Turkish, and Persian

### PUBLICATIONS

#### A. Thesis

1. Effect of heat treatment on microstructural and mechanical properties of molybdenum-based pm ferrous alloys, M. Sc. Thesis, METU, 2016.

#### B. Journal Articles

1. Tailoring humidity sensing behavior of titanosilicates with Ti-O-Ti wires by vanadium substitution, in press.

### **C. Conference and Meeting Presentations**

1. 20th International Zeolite Conference “Studying Humidity Sensing Behavior of microporous ETS-10 and Vanadium substituted ETS-10 Thin Films” (Poster Presentation), 3-8 July 2022 Valencia, Spain.

2. Materials Research Society (MRS) Fall Meeting and Exhibit, “Humidity Sensing Behavior of Microporous Titano / Vanadosilicate Thin Films: Effect of film preparation and stability” (Oral Presentation), November 29-December 2, 2021, Boston, USA.

3. Materials Research Society (MRS) Fall Meeting and Exhibit, “Humidity Sensing Behavior of Microporous Titanosilicate and Vanadosilicate Thin Films” (Oral Presentation), 1-6 December 2019, Boston, USA.

4. 42nd Annual Meeting of the British Zeolite Association, “Humidity Sensors Based on Microporous Titanosilicate & Vanadosilicate Thin films” (Poster Presentation), 11-12 April 2019, Birmingham, United Kingdom.

5. 7th FEZA Conference “The ZEOLITES: Materials with Engineered Properties,” “Humidity Sensors Based on Zeo-type Titanosilicate ETS-10 and Zeolite Y” (Oral Presentation), 3-7 July 2017, Sofia, Bulgaria.

### **AWARDS**

2016-2017 Academic Year METU Graduate Courses Performance Award.